EXPERIMENTAL ANALYSIS AND FINITE ELEMENT MODELLING OF MECHANICAL STOPPERS UNDER IMPACT LOADING

MEKANIK DURDURUCULARIN ÇARPIŞMA YÜKÜ ALTINDA DAVRANIŞININ DENEYSEL ANALİZİ VE SONLU ELEMANLAR MODELLEMESİ

CAN KÖKSAL

PROF. DR. BORA YILDIRIM
Supervisor

Submitted to
Graduate School of Science and Engineering of Hacettepe University
as a Partial Fulfillment to the Requirements
for the Award of the Degree of Master of Science
in Mechanical Engineering

2021

ABSTRACT

EXPERIMENTAL ANALYSIS AND FINITE ELEMENT MODELLING OF MECHANICAL STOPPERS UNDER IMPACT LOADING

Can KÖKSAL

Master of Science, Department of Mechanical Engineering
Supervisor: Prof. Dr. Bora YILDIRIM
June 2021, 100 Pages

The aim of this thesis is to determine and understand the characteristic of impact loading and reaction of different materials colliding to each other. In engineering area, especially for moving mechanisms, such designs needs to be constrained by electrical and/or mechanical stoppers which is a complex phenomenon and, this phenomena can not to be understood easily. To design a valuable stopper, designer needs to know the impact parameters and the resistance of the stoppers to the energy acquired during the impact occurrence. To do so, a known geometry used for antenna motion and simple rotational motion mechanism is examined and modelled in ANSYS/Mechanical. In parallel, this motion is modelled by analytical solution previously studied and can be found on the literature. Many studies are examined and many different solutions found in the literature to compare the results obtained from the finite element model. At the end of this study, for the known geometry, real time impact tests are carried on to see what happens exactly. During the tests, SIEMENS data acquisition software and LMS data acquisition hardware are used. For different materials such as Aluminum 6061-T6, Stainless Steel AISI 304 and Titanium Alloy Ti4-6Al-V are used as stopper and Aluminum 6061-T6 moving mechanism end. In addition, for the motion,

impact is carried out at different rotational velocities of 5, 10, 15, 20, 25 and 30 rpm. Each result is recorded individually. To take the impact data, a tee rosette strain gauge is used to obtain the strain data of the stopper in time domain. Data results are examined and it is seen that the results for different impact velocities are consistent. As the velocity increases, elastic deformation at the surface of the stopper increases, while, impact duration does not change abruptly. The impact occurrence fits to the finite element model developed in ANSYS with a certain acceptable amount of error. Thus, this gives us to use the analytical models to obtain the impact force between the two materials.

Keywords: Impact, Impact Mechanics, Collision, Collision Modelling, FEM, FEA, Collision Duration, Collision Indentation, Collision Mechanics

ÖZET

MEKANIK DURDURUCULARIN ÇARPIŞMA YÜKÜ ALTINDA DAVRANIŞININ DENEYSEL ANALİZİ VE SONLU ELEMANLAR MODELLEMESİ

Can KÖKSAL

Yüksek Lisans, Makina Mühendisliği Bölümü
Tez Danışmanı: Prof. Dr. Bora YILDIRIM
Haziran 2021, 100 Sayfa

Sunulan tez kapsamında, çarpışma yüklerinin karakteristiği ve farklı malzemelerin çarpışma yüklerinin ve tepkilerinin anlaşılması de belirlenmesi amaçlanmıştır. Mühendislik alanında, özellikle de hareketli mekanizmalarda, bir takım mekanizmaların hareketleri elektriksel ya da mekanik durdurucularla kısıtlanmıştır. Mekanik durdurucular ve çarpışma ile hareket kısıtlama karmaşık bir fenomendir ve genellikle altındaki fiziksel mekanizmayı anlamak zordur. Tasarımcıların iş gören bir mekanik durdurucu tasarlayabilmeleri için çarpışma parametrelerini ve çarpışan malzemelerin çarpışma sırasında çıkan enerjiyi nasıl absorb ettiklerini anlamaları gerekir. Bu çalışmayı yürütebilmek adına, daha önceden tasarlanmış ve geometrisi bilinen bir anten yönlendirme birimi ve döner hareket mekanizması incelenmiş ve ANSYS/Mechanical yazılımı içerisinde modellenmiştir. Bu modellemeye paralel olarak, bu hareket ve çarpışma literatürde bulunan daha önceden çalışılmış analitik modeller ile modellenmiştir. Literatürde çarpışma yükü modellenmesine dair birçok analitik çalışma ve çözüm bulunmaktadır. Bu çözümler ile sonlu elemanlar analizi sonuçları karşılaştırılmıştır. Tez çalışmasının son basamağı olarak, bahsedilen mekanizma ürettirilmiş ve gerçek zamanlı çarpışma testleri yürütülmüştür. Bu çarpışma testlerinde gerçekte tam olarak ne olduğu gözlenmiştir. Testler yürütülürken SIEMENS veri işleme yazılımı ve LMS veri işleme

sisteminden faydalanılmıştır. Test için Alüminyum 6061-T6, Paslanmaz Çelik AISI304 ve Titanyum alaşımı TI4-6Al-V malzemelerden mekanik durdurucular üretilmiş ve Alüminyum 6061-T6 malzemeden üretilen hareketli mekanizma sonuna çarptırılmıştır. Bütün bunlara ek olarak 5, 10, 15, 20, 25 ve 30 RPM gibi farklı hızlarda çarpışmalar tekrarlanmıştır. Her hız ve malzeme için farklı veri toplanmış ve kaydedilmiştir. Çarpışma verilerini zaman bölgesinde toplayabilmek ve mekanik durdurucu üzerindeki gerinim ölçebilmek için dirsek rozet gerinim ölçerler kullanılmıştır. Toplanan veriler incelenmiş ve her malzeme ve hız verilerinin kendi içerisinde tutarlı olduğu görülmüştür. Çarpışma hızı arttırıldıkça mekanik durdurucu üzerindeki gerinim arttığı ama çarpışma süresinin ciddi değişim yaşamadığı görülmüştür. Yapılan testler ile sonlu elemanlar analizi sonuçlarının Kabul edilebilir bir hara aralığı içerisinde örtüştüğü saptanmıştır. Bu da model üzerinden çarpışma parametrelerini ve çarpışma yükünü çıkarmamıza yardımcı olmuştur.

Anahtar Kelimeler: Darbe, Darbe Mekaniği, Çarpışma, Çarpışma Modellemesi, SEM, SEA, Çarpışma Süresi, Çarpışma İzi, Çarpışma Mekaniği

ACKNOWLEDGEMENT

I would like to thank to my supervisor Prof. Dr. Bora YILDIRIM for his support and guidance with this study. With his motivation and great patience, especially in the rough days of NCov-Covid19 pandemic, I could manage the difficulty of master's study. Without his valuable help, technical support and engineering insight, this study will never have come into life.

I would also like to thank to İsmail GÜLER, manager of Servo Technologies Design Engineering Department of ASELSAN A.Ş. with his executive support, tolerance and trust. In addition, I would like to express my thanks and gratitude to my colleagues and friends Ufuk YİĞİT, Hazim Sefa KIZILAY and Dr. Barış ULUTAŞ for their technical and moral support, comments and discussions.

I would like to give my greatest thanks to my beloved family, who supported me whole my life and held my hand, my mother Emel KÖKSAL, my father Hasan KÖKSAL and my sister Ece KÖKSAL for their effort through my childhood and education period, and also to my dear fiancée Gözde TEKELİ, for their limitless support, tolerance, patience, encouragement and especially for their unconditional love.

Finally, I thank to my company ASELSAN A.Ş. for providing me chance to complete my study.

TABLE OF CONTENTS

ABSTRACT v

ÖZET vii

ACKNOWLEDGEMENT ix

TABLE OF CONTENTS x

LIST OF TABLES xii

LIST OF FIGURES xiv

SYMBOLS AND ABBREVIATIONS xviii

1 INTRODUCTION 1

1.1 Motivation of the Study 1

1.2 Literature Survey 1

1.3 Aim of The Study 17

1.4 Thesis Layout 21

2 MATHEMATICAL MODELLING 22

2.1 Hertzian Impact Theory 22

2.2 Developed Models from Hertizan Impact Theory 23

3 IMPACT TEST 26

3.1 Test Layout and Set-Up 26

3.2 Test Verification 34

3.3 Collision Test Results 39

4 COMPUTER AIDED ANALYSIS 48

4.1 Geometry Analysis and Preparation 48

4.2 ANSYS Mechanical Model 52

4.3 FEM Results 58

5 COMPARISON OF TESTS, ANALYSES AND MATHEMATICAL MODELS 69

5.1 Test and FEM Analysis Comparison 69

5.2 Implementation to Mathematical Models 77

5.3 Characterization of Stoppers and Recommendations 82

6 CONCLUSION AND FUTURE WORK 86

7 REFERENCES 88

8 APPENDIX.....91

A. Strain Gauge Datasheet 91

B. M-Bond 200 Strain Gauge Adhesive Datasheet.....93

C. Strain Data Read-Write and Transformation MATLAB Code for AL6061-T651 Specimen.....95

D. Control MATLAB Code for Strain Gauge Validation 99

LIST OF TABLES

Table 2.2.1 Contact-Force Models 25
Table 3.1.1 Mechanical Properties of Selected Materials 26
Table 3.1.2 Tilt Angles of Strain Gauges on Stopper Parts 33
Table 3.2.1 Comparison of Test Results and Hand Calculations 39
Table 4.2.1 Materials and Mechanical Properties 52
Table 4.2.2 Material Assignment Table 53
Table 4.2.3 Mesh Options and Statistics 56
Table 4.2.4 Rotational Velocity Profile 57
Table 4.2.5 Sub Step Control of Explicit Dynamics 58
Table 4.3.1 Strain Value, Peak Time and Impact Duration 68
Table 5.1.1 Test and FEM Results Comparison for Aluminum Stopper 73
Table 5.1.2 Test and FEM Results Comparison for Steel Stopper 73
Table 5.1.3 Test and FEM Results Comparison for Titanium Stopper 73
Table 5.1.4 Impact duration of Test Result for Different Materials 74
Table 5.1.5 Impact Duration - Impact Velocity Relation for Aluminum Stopper 75
Table 5.1.6 Impact Duration - Impact Velocity Relation for Steel Stopper 75
Table 5.1.7 Impact Duration - Impact Velocity Relation for Titanium Stopper 75
Table 5.2.1 Impact Parameters for Aluminum Stopper 78
Table 5.2.2 Impact Parameters for Steel Stopper 79
Table 5.2.3 Impact Parameters for Titanium Stopper 79
Table 5.2.4 Calculated Hysteresis Damping Factors and Contact Forces for Aluminum Stopper 80
Table 5.2.5 Calculated Hysteresis Damping Factors and Contact Forces for Steel Stopper 80
Table 5.2.6 Calculated Hysteresis Damping Factors and Contact Forces for Titanium Stopper 81
Table 5.2.7 FEM Contact Reaction Forces 81
Table 5.2.8 Error Percentage of Reaction Force for Aluminum Stopper 81
Table 5.2.9 Error Percentage of Reaction Force for Steel Stopper 82

Table 5.2.10 Error Percentage of Reaction Force for Titanium Stopper 82

LIST OF FIGURES

Figure 1.2.1 Hertz Contact Law Model 3
Figure 1.2.2 Surface Contact Models for Mating Cylinders, Vertical Cylinder on Flat Surface and Cone Nose on Flat Surface 11
Figure 1.2.3 Pressure vs. Time History at Oil Chamber During Impact for Different Impact Velocities 13
Figure 1.2.4 ANSYS Model for the Low-velocity Impact Analysis 14
Figure 1.2.5 Low-velocity Impact Test Configuration for Energy Absorption Analysis of 3D Printed Architected Sandwich Panels 14
Figure 1.2.6 Collision Damage to the Barge at Speeds of 3 Knots and 5 Knots 16
Figure 1.3.1 Antenna Guidance System Model 18
Figure 1.3.2 Antenna Guidance System Model (Colored) 19
Figure 1.3.3 Antenna Guidance System Model Elevation Positive Limit 19
Figure 1.3.4 Antenna Guidance System Model Elevation Negative Limit 20
Figure 3.1.1 Test Assembly Model 27
Figure 3.1.2 Assembled Test System 28
Figure 3.1.3 Strain Gauge Position on the Stopper 29
Figure 3.1.4 Strain Gauge and Datasheet 30
Figure 3.1.5 Strain Gauge Position on Impact Stopper 31
Figure 3.1.6 Stainless Steel and Titanium Alloy Stoppers with Strain Gauges 32
Figure 3.1.7 Tilt Angles of Strain Gauges on Stopper Parts of Aluminum 6061 T6, Titanium Ti-6Al-4V and Stainless Steel AISI 304 32
Figure 3.1.8 Stainless Steel Stopper Before, During and After the Impact 33
Figure 3.2.1 Strain Gauge Verification Test Set-Up Drawing 34
Figure 3.2.2 Strain Gauge Verification Test Set-Up for Distance 200 mm 35
Figure 3.2.3 Strain Gauge Verification Test Set-Up for Distance 100 mm 35
Figure 3.2.4 Mass of Dummy Piece 37
Figure 3.2.5 Static Strain Level in Channel 1 for Both Control Points 37
Figure 3.2.6 Static Strain Level in Channel 2 for Both Control Points 38
Figure 3.2.7 Static Strain Level in Channel 3 for Both Control Points 38

Figure 3.3.1 Coordinate System and Channel Directions of Strain Gauge 41
Figure 3.3.2 Aluminum Stopper Channel 1 Test Results 41
Figure 3.3.3 Aluminum Stopper Channel 2 Test Results 42
Figure 3.3.4 Aluminum Stopper Channel 3 Test Results 42
Figure 3.3.5 Steel Stopper Channel 1 Test Results 43
Figure 3.3.6 Steel Stopper Channel 2 Test Results 43
Figure 3.3.7 Steel Stopper Channel 3 Test Results 44
Figure 3.3.8 Titanium Stopper Channel 1 Test Results.....44
Figure 3.3.9 Titanium Stopper Channel 2 Test Results.....45
Figure 3.3.10 Titanium Stopper Channel 3 Test Results.....45
Figure 3.3.11 Maximum Strain of Stoppers With Respect to Velocities for Channel 1 ...46
Figure 3.3.12 Maximum Strain of Stoppers With Respect to Velocities for Channel 2 ...47
Figure 3.3.13 Maximum Strain of Stoppers With Respect to Velocities for Channel 3 ...47
Figure 4.1.1 Primitive Simplified Geometry Assembly 50
Figure 4.1.2 Final Analysis Geometry Assembly.....51
Figure 4.1.3 Analysis Geometry and Test Part Comparison 51
Figure 4.2.1 Schematic Representation of Test Assembly.....54
Figure 4.2.2 Generated Mesh on Bodies 55
Figure 4.2.3 Generated Mesh on Stopper and Collision Arm 55
Figure 4.2.4 Rotational Velocity Profile 57
Figure 4.3.1 Small Peaks Before and After the Main Peak of Impact Strain.....59
Figure 4.3.2 Stationary Stopper Impact Surface.....60
Figure 4.3.3 Deflected Stationary Stopper Surface 60
Figure 4.3.4 Von-Misses Stress Generated on Steel Stopper Specimen Strain Gauge Surface 61
Figure 4.3.5 Von-Misses Stress Generated on Aluminum Stopper Specimen Strain Gauge Surface 61
Figure 4.3.6 Von-Misses Stress Generated on Titanium Stopper Specimen Strain Gauge Surface 62
Figure 4.3.7 Normal Strain in (X) Direction for Aluminum Stopper.....62
Figure 4.3.8 Normal Strain in (Y) Direction for Aluminum Stopper.....63

Figure 4.3.9 Normal Strain in (X) Direction for Steel Stopper..... 63
Figure 4.3.10 Normal Strain in (Y) Direction for Steel Stopper..... 64
Figure 4.3.11 Normal Strain in (X) Direction for Titanium Stopper..... 64
Figure 4.3.12 Normal Strain in (Y) Direction for Titanium Stopper..... 65
Figure 4.3.13 Normal Strain Contour in (X) Direction for Aluminum Stopper..... 65
Figure 4.3.14 Normal Strain Contour in (Y) Direction for Aluminum Stopper..... 66
Figure 4.3.15 Normal Strain Contour in (X) Direction for Steel Stopper 66
Figure 4.3.16 Normal Strain Contour in (Y) Direction for Steel Stopper 67
Figure 4.3.17 Normal Strain Contour in (X) Direction for Titanium Stopper..... 67
Figure 4.3.18 Normal Strain Contour in (Y) Direction for Titanium Stopper..... 68
Figure 5.1.1 Aluminum Stopper Comparison of Test and FEM Normal Strain Results in (X) Direction 69
Figure 5.1.2 Aluminum Stopper Comparison of Test and FEM Normal Strain Results in (Y) Direction 70
Figure 5.1.3 Steel Stopper Comparison of Test and FEM Normal Strain Results in (X) Direction 70
Figure 5.1.4 Steel Stopper Comparison of Test and FEM Normal Strain Results in (Y) Direction 71
Figure 5.1.5 Titanium Stopper Comparison of Test and FEM Normal Strain Results in (X) Direction 71
Figure 5.1.6 Titanium Stopper Comparison of Test and FEM Normal Strain Results in (Y) Direction 72
Figure 5.1.7 Impact Duration - Impact Velocity Relation in Elastic Region from LU's Study 76
Figure 5.1.8 Impact Duration - Impact Velocity Relation in Plastic Region from LU's Study 76
Figure 5.1.9 Impact Duration - Impact Velocity Relation from Impact Tests for Different Materials 77
Figure 5.2.1 Velocity Profiles of FEM Results..... 78
Figure 5.3.1 Stress Level for Aluminum Stopper 84
Figure 5.3.2 Stress Level for Steel Stopper 85

Figure 5.3.3 Stress Level for Titanium Stopper 85

SYMBOLS AND ABBREVIATIONS

F_n	: Contact Force
K	: Contact Stiffness Parameter
δ	: Value of Indentation
h_k	: Contact Stiffness for the k-th Body
ν	: Poission's Ratio for the k-th Body
E	: Elastic Modulus for the k-th Body
R_k	: Radii of the k-th Body
a	: Contact Area
P_{max}	: Stress Level at the Center of the Contact Area
d_k	: Depth of Indentation
$\dot{\delta}$	: Indentation Velocity
D	: Energy Dissipation
χ	: Hysteresis Damping Factor
$\dot{\delta}_0$	: Initial Relative Impact Velocity
c_r	: Restitution Coefficient
m_{eff}	: Efficienf Mass
m_k	: Mass of the k-th Body
ρ	: Specific Density
d	: Non-dimensional Gonthier Factor
δ_{max}	: Maximum depth of Indentation
ε	: Elastic Strain
σ	: Stress
COR	: Coefficient of Restitution
COI	: Coefficient of Indentation

1 INTRODUCTION

1.1 Motivation of the Study

In recent years, researches in multibody dynamics have been increased. With the improvements in the kinematics area and the advanced growing in the material characterization, impacts and the collisions take place in the multibody dynamics and kinematics area significantly. For the most of the engineering fields, collision is taken into account for the new design developments. Thus, research in the collision or impact phenomena gets higher attention.

Impact or collision is a complex phenomenon that occurs in very little time increment that cannot be captured easily. Thus, deeply detailed investigation is needed. For many years, scientists and engineers tried to explain the events occurring during collision. First, it may be said to be started with Hertzian Contact Theory, which is introduced by Heinrich Hertz in 1882. In this approach, Heinrich Hertz modelled two solids, where the two of them has spherical shapes, and investigated the deformation of these solid bodies colliding. Since there are two spherical solids colliding or touching to each other, contact area is formed by a contact point. Moreover, he created a mathematical model that captures the deformation and stress at each spherical solid bodies. In addition, a term, tribology has been generated from the Hertz's Theory that Hertzian Contact Stress, which refers to the stress area where occurs near the contact point. Hertz Contact Theory investigates the contact and friction phenomena under colliding and contacting bodies with an analytical solution. Moreover, this theory became a pioneer study for other engineers and scientists to develop new concepts and theories. Now on, with the Hertzian Contact Theory, we have many other approaches for contact and collision dynamics to investigate the behavior of colliding or contacting bodies.

1.2 Literature Survey

As we discussed above, first known attempt to understand the mechanics of contact and collision is developed by Heinrich Hertz. In 1882, Heinrich Hertz published a paper, "*Über die Berührung fester elastischer Körper*" [1], which is "*On the contact of elastic solids*", while he was working on optic materials, and understanding the behavior of multi stacked

optic lenses and how their optical behavior changes with the change of the fore, which holds them together. Since he was working on the optical lenses, his approach is built on the surfaces with curvatures. As the deformation of the curvatures of the two spherical lenses changes, their focus point and optical properties changes, thus the deformation behavior of the lenses must be investigated under these circumstances. His work investigates the contact force as a power function of the displacement of each spherical body through each other of shortly, indentation and can be expressed as,

$$F_n = K\delta^n$$

Where, F_n is contact force, K is contact stiffness parameter, which is a unique parameter for the case where collision occurs and δ is the value of indentation. Contact stiffness is an analytical parameter and it is a case wise parameter, which is dependent on the radii or the two contacting spheres, and material properties of the contacting media. It can be shown simply as [2],

$$K = \frac{4}{3 * (h_i + h_j)} * \sqrt{\frac{R_i * R_j}{R_i + R_j}}$$

This equation is an analytical equation and it will may differ for different contacting geometries, which are explained later on. In the equation of contact stiffness, there is a term h_k, for the k-th body, which is material property term, and is simply as,

$$h_k = \frac{1 - v_k^2}{E_k} \qquad k = i, j,$$

The parameters E_k and v_k are, as a general elasticity notation, the Young's modulus and the Poison's ratio, respectively. Contact stiffness constant may vary due to the geometry of colliding solids and will be discussed later. However, as discussed above, Hertzian Contact Stress is calculated for two contacting spheres. At the very first initial time of the collision, the contact occurs at a point but, as the two materials deforms each other, is becomes a circular area, where the contact stress is maximum at the circle origin as seen in Figure *1.2.1*.

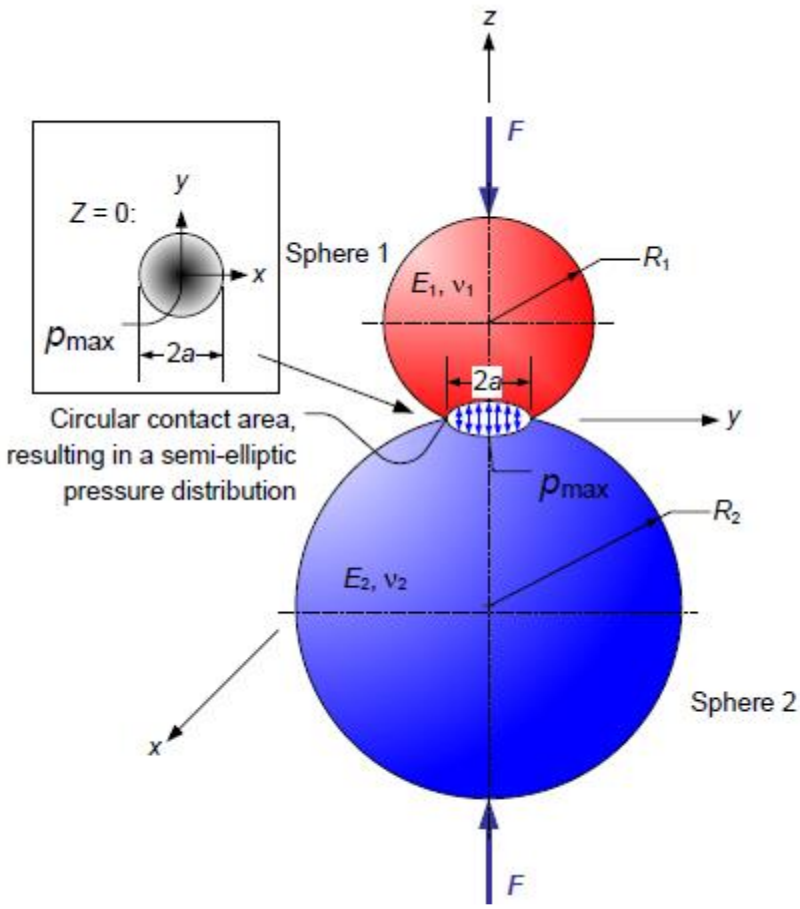

Figure 1.2.1 Hertz Contact Law Model

The radius of the contact area can be found by the following equation [3],

$$a = \sqrt[3]{\frac{3 * F * (\frac{1 - v_1^2}{E_1} + \frac{1 - v_2^2}{E_2})}{4 * (\frac{1}{R_1} + \frac{1}{R_2})}}$$

Where E is for Young's Modulus, v is for Poison's Ratio and R is for radius of the spheres seen in the figure above. Another important parameter of the collision is the collision force, that we may discuss it later.

As it is said above, the maximum stress occurs at the center of the circular contact area. This is a fact for collision dynamics of two spheres because; the maximum deformation for the

both colliding solids is the center of the area. Therefore, it is important to evaluate the stress level at the center of contact area, which is,

$$P_{max} = \frac{3 * F}{2 * \pi * a^2}$$

In addition, the resulting depth of indentation, or, the deformation can be calculated from the below equation,

$$d_k = \frac{a_k^2}{R_k} = \sqrt[3]{\frac{9 * F^2}{16 * R_k * E_k^2}} \ , \qquad k = 1, 2,$$

For each k value, indentation of each solid sphere can be calculated by using its own values.

As we discussed above, the recent collision dynamic researches are based on the Heinrich Hertz's work. Then analytical solutions are developed from this spherical contact approach. Sphere to flat surface and cylinder-to-cylinder surface solutions are developed and verified. As seen in the first equation, Hertz modelled collision as perfectly elastic contact-force model. However, this model does not account for the energy dissipation in the contact and the solid media that is naturally present in the mechanical media. Therefore, it is not convenient to model the collision or contact as the compression and restitution phases as Hertz developed. To overcome the energy dissipation phenomena, a new model developed by Kelvin and Voigt, which is modelled as a linear spring and linear damper element. Hertzian model and Kelvin-Voigt model are combined in parallel and a new contact force approach is obtained [2],

$$F_n = K * \delta + D * \dot{\delta}$$

In this approach, again, F_n represents the contact force, K represents the contact stiffness and δ represents the indentation. The new terms are arisen for considering the energy dissipation. D term represents the energy dissipation coefficient and $\dot{\delta}$ represents the relative contact velocity or indentation velocity. Kelvin-Voigt approach is used in researches and studies for a long time due to its simplicity and linearity. In addition, Khulief and Shabana [4] used this

model to introduce flexible bodies, and this model is used to evaluate the vertical forces on a tire in vehicle dynamics.

As seen above, Kelvin-Voigt model is a linear contact model, which is suitable for higher impact velocities [5]. However, this is not the case for slower collisions. To overcome this problem, Dubowsky et al. suggested that the dissipation factor is a nonlinear function of the deformation [6]. Nevertheless, this approach has disadvantages. At the start of the collision process, the initial deformation value must have zero value and the energy dissipation component of the contact force is a non-zero value. Which yields a physically inconsistency. In addition, at the end of the collision process, where the restitution phase finishes, the contact deformation, indentation value is zero but the relative velocity is a negative value. To overcome this inconsistency problems, Hunt and Crossley suggested a new model, which evaluates the contact physics more accurately [7]. Hunt and Crossley suggested that the exponent of the damping coefficient has to be identical with the exponent of the linear spring and has the form of,

$$F_n = K * \delta^n + \chi * \delta^n * \dot{\delta}$$

In which the χ symbol stands for the hysteresis-damping factor, which is,

$$\chi = \frac{3}{2} * \frac{K}{\dot{\delta_0}} * (1 - c_r)$$

Where, $\dot{\delta_0}$ stands for the initial relative impact velocity in the normal direction of contact surface and c_r is the restitution coefficient. Substituting the hysteresis-damping coefficient into the Hunt and Crossley model, we will get,

$$F_n = K * \delta^n (1 + \frac{3 * (1 - c_r)}{2} * \frac{\dot{\delta}}{\dot{\delta_0}})$$

It is not an easy process to obtain contact properties, thus, Guess et al. conducted a finite element analysis to evaluate these properties [8]. The Hunt and Crossley model works with a high value of the restitution coefficient, which means the impact has a lower energy dissipation. Herbert and McWhannel proposed a new model by using Hunt-Crossley model,

which uses the restitution coefficient as the main element of the impact process [9]. They redefined the hysteresis-damping factor as,

$$\chi = \frac{6}{(2 * c_r - 1)^2 + 3} * \frac{K}{\dot{\delta}_0} * (1 - c_r)$$

Thus, contact force equation yield to,

$$F_n = K * \delta^n (1 + \frac{6 * (1 - c_r)}{(2 * c_r - 1)^2 + 3} * \frac{\dot{\delta}}{\dot{\delta}_0})$$

Herbert and McWhannell model is a developed form of the Hunt and Crossley model. There is a slight difference between the coefficients of the hysteresis-damping factor, which is equal to 1.5 %. Herbert and McWhannell's model is widely used for gear dynamics. To fulfill the boundary conditions of hysteresis-damping factor, Lee and Wang proposed a new model and they overcome the physically inconsistency problem mentioned above [10]. According to their study, the hysteresis-damping factor is defined as,

$$\chi = \frac{3}{4} * \frac{K}{\dot{\delta}_0} * (1 - c_r)$$

Which yields a normal contact force equation as,

$$F_n = K * \delta^n (1 + \frac{3 * (1 - c_r)}{4} * \frac{\dot{\delta}}{\dot{\delta}_0})$$

Lee and Wang's model is simple to use however, it is not always chosen to introduce multibody dynamics with impact contact mechanics [10]. On another model, Lankarani and Nikravesh developed an approach that possesses the kinetic energy loss due to the internal damping of the contacting solids [11]. This model is based on the kinetic energy before and after impact-contact event. The kinetic energy gradient is calculated as a function of coefficient of restitution and the normal component of the relative velocity at the impact-contact event, which is,

$$\delta E = \frac{1}{2} * m_{eff} * \dot{\delta}_0^2 * (1 - c_r)$$

Where the equivalent mass, m_{eff} is the mathematical combination of impacting- contacting solids, which can be shown as,

$$m_{eff} = \frac{m_i * m_j}{m_i + m_j}, \qquad i = 1, j = 2,$$

To find the loss of the energy, one must integrate the contact force over time. If the contact force is assumed to have the same characteristic with the restitution force, the loss of kinetic energy will become,

$$\delta E = \frac{2}{3} * m_{eff} * \dot{\delta}_0^2 * \frac{\chi}{K}$$

In addition, hysteresis-damping factor is,

$$\chi = \frac{3}{4} * \frac{K}{\dot{\delta}_0} * (1 - c_r)$$

Thus, combining these equations and integrating will yield,

$$F_n = K * \delta^n (1 + \frac{3 * (1 - c_r)}{4} * \frac{\dot{\delta}}{\dot{\delta}_0})$$

This approach is only be applicable when the initial relative contact velocity is far less than the velocity of wave propagation in the material,

$$\dot{\delta}_0 \leq 10^{-5} * \sqrt{\frac{E}{\rho}}$$

Where, E is the Young's Modulus of the material and ρ is the specific density.

Lankarani and Nikravesh developed this model and it was useful for the impact-contact events in which the loss of kinetic energy is small, which means the model is successful for the case in which the coefficient of restitution is close to one. In another research, Shivaswamy has shown that, as the contact velocity reduces, it has larger effect on the energy dissipation [12]. The Lankarani and Nikravesh model was used in several studies and it

influenced many other researchers and models to be developed [13], [14], [15]. This model is for use in planar contact surfaces [16].

Gonthier et al. suggested another impact-contact event model, which is accepted to be best for larger contact surfaces and defines hysteresis-damping factor for larger surface contacts [17],

$$\chi = \frac{d}{c_r} * \frac{K}{\dot{\delta}_0}$$

Where d is a non-dimensional factor in the form of,

$$1 + \frac{d}{c_r * (1 - d)} = e^{d*(1+\frac{1}{c_r})}$$

Can be simplified and approximated to,

$$d \approx 1 - c_r^2$$

As a result, contact model and contact force for Gonthier's model is,

$$F_n = K * \delta^n (1 + \frac{(1 - c_r^2)}{c_r} * \frac{\dot{\delta}}{\dot{\delta}_0})$$

The contact-force model of Gonthier et al. can be mainly related to force, which is expressed as an explicit non-linear function of the contact volume and volume contact stiffness. The contact force has a unit of Newton per volume; however, it is not always possible to evaluate the parameter of volume stiffness. To overcome the volume stiffness problem, Zhiying and Qishao developed a new model for impact-contact event [18], which is,

$$\chi = \frac{3 * (1 - c_r^2) * e^{2*(1-c_r)}}{4} * \frac{K}{\dot{\delta}_0}$$

Yields contact force equation to,

$$F_n = K * \delta^n (1 + \frac{3 * \left(1 - c_r^2\right) * \left(e^{2*(1-c_r)}\right)}{4} * \frac{\dot{\delta}}{\dot{\delta}_0})$$

Zhiying and Qishao proposed this model to analyze the correlation between the coefficient of restitution, the contact parameters and the energy dissipation during the impact-contact event. Another force-contact model was developed by Flores, which combines Hertz's contact theory with the hysteresis-damping coefficient, which includes the energy loss during the event [19]. Flores evaluated the loss of kinetic energy during contact by using simple pendulum in contact with a wall. This dynamic model gave him the relation between the initial contact velocity and the restitution velocity and developed his model as follows,

$$\delta E = \frac{1}{4} * \chi * (1 - c_r) * \dot{\delta}_0 * \dot{\delta}_{max}^{\frac{5}{2}}$$
$$\chi = \frac{8 * (1 - c_r)}{5 * c_r} * \frac{K}{\dot{\delta}_0}$$

In which the term δ_{max} is the maximum depth of indentation or deformation at the contact. So, after evaluating the contact parameters, the contact force equation becomes,

$$F_n = K * \delta^n (1 + \frac{8 * (1 - c_r)}{5 * c_r} * \frac{\dot{\delta}}{\dot{\delta}_0})$$

These models are developed for impact-contact events occurring between elastic and inelastiv solids. Thus, suggested equations are very close to the model, which Gonthier et al. generated. Moreover, another contact model was developed by Hu and Guo, which focuses on the contact occurrences between softer materials [20]. Softer materials have smaller coefficient of restitution which, yields contacts that are more elastic and higher loss of energy. According to their approach, hysteresis-damping coefficient can be shown as,

$$\chi = \frac{3 * (1 - c_r)}{2 * c_r} * \frac{K}{\dot{\delta}_0}$$

Which yields a contact force equation as,

$$F_n = K * \delta^n (1 + \frac{3 * (1 - c_r)}{2 * c_r} * \frac{\dot{\delta}}{\dot{\delta}_0})$$

As considered above, there are many approaches and many models generated to investigate the natural behavior of impact-contact event. From Hertz's model to Hu and Guo, many scientists and engineers have tried to understand the occurrence of impact-contact event and tried to fit an analytical model to the action. From high impact velocities to low impact velocities, softer materials to harder materials and high impact energy dissipation to low impact dissipation, there are many analytical models found in the literature to fit an implementation of an impact case. It should not be forgotten that, these models are created analytically, which are depend on and proven by real time impact tests. For a new research, someone should list these mathematical models, and for the specific case, should fit one of these models then test and correlate it. Otherwise, the result may vary the results of the real case and there will be misleading.

As a literature review, Luka Skrinjar, Janko Slavic and Miha Boltezar published a paper that introduces recently and well-established analytical contact-force models used in the dynamical analysis of multibody systems [21]. In the study, they introduced the contact groups in two main groups and investigated as the general (point contact) and cylindrical (line contact) models. For the point contact group, they have investigated 20 different contact models and analyzed them and for the second cylindrical contact group, they have introduced 10 models. At the paper, they have shown that they have numerically simulated the contact models. After numerical simulations, they have conducted basic numerical experiments to compare the evolution of the contact force for the impact-contact event with general contact models mentioned above with energy dissipation and with and without energy dissipation for cylindrical contact models. They have aimed to generate general basic guidelines for selection of a proper impact-contact model and formulation for a specific case or application in the analysis of multibody contact dynamics. Furthermore, they have tried to research and present the hysteresis effect of impact damping coefficient for contact-force models. As a result of their work, they have described a comparison and review of the recently used continuous contact-force models with general or cylindrical contact between bodies. They have introduced 20 different contact-force model with general (point) contact and 10

different cylindrical (line) contact. They claimed that, when comparing the result of a dynamical response of colliding bodies, the initial and restituting velocities of the bodies and selected coefficient of restitution plays an important role with the selection of proper model. Furthermore, the energy loss of the dynamic system during impact-contact event changes significantly and increases as the selected value of the coefficient of restitution approaches to zero. In addition, the study pointed that for some of the force-contact models it is convenient to choose the coefficient of restitution value between the values of 1 and 0. However, for the six of the models listed in the work, it is better to choose the same parameter between 0.5 and 1.

In another study, Xiaoyin Zhu investigated Hertz contact stress with mating parts [3]. As he claims, this kind of stress occurs in the contact area of spherical mating parts, which is not always be significant but under some circumstances, may cause serious problems and must be taken into account. To analyze the Hertz contact stress, in his work, considered five types of classic solutions for non-adhesive elastic contact and application of Hertz contact stress theory on opto-mechanical engineering field. As a result of his paper, he exampled the areas and applications of need of Hertz contact stress and importance of evaluation of point or line contact of bodies.

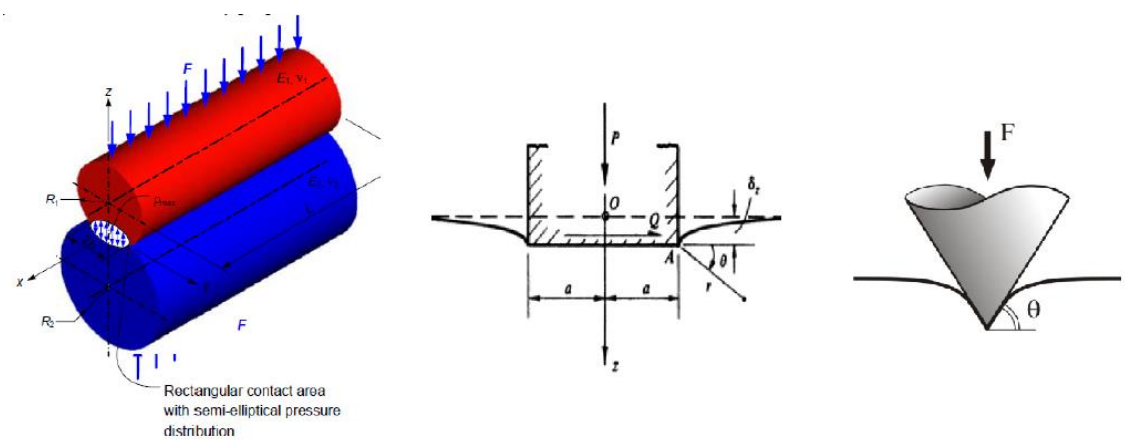

Figure 1.2.2 Surface Contact Models for Mating Cylinders, Vertical Cylinder on Flat Surface and Cone Nose on Flat Surface

Joshi Avinash and Gupta Laxmikant conducted another study about damage in bridge piers subjected to vehicle collisions [22]. In their study, they have studied the responses of several piers with varying geometries by finite element analysis. They tried to investigate the areas of damage on the pier geometries and estimate the damage sustained the pier under consideration. The work is supported with materials non-linear effects in the static and dynamic collision zones by using MATLAB. Then the numerical results were correlated with finite element analysis method via ANSYS. The collision loads were considered to be based on the standards and specifications of different countries while force-time histories were obtained for transient elastoplastic response from the simulated car crash tests. Pier geometries were chosen to be solid rectangular wall, solid circular and solid hollow circular piers. In the first part of the study, static analyses whose parameters are dependent on the specifications of several countries like the USA, India and the UK, conducted. In the second part, the colliding vehicles were chosen into two specifications, as a lightweight truck, 14kN Chevy and a medium weight truck, 66kN Ford, which were impacted through the pier geometries to obtain force-time history of the collision event. As a result of this study, it is seen that in the static loading part, dual plasticity estimation plays an important role on the expected damage. The judgement of the selection of suitable pier geometry can be done by applying the static load specified in the standards of the countries. The dynamic part of the study suggests that, the pier geometry and the pier material must be considered while design step if there is such traffic because, the damage recorded on all the piers are considerably high.

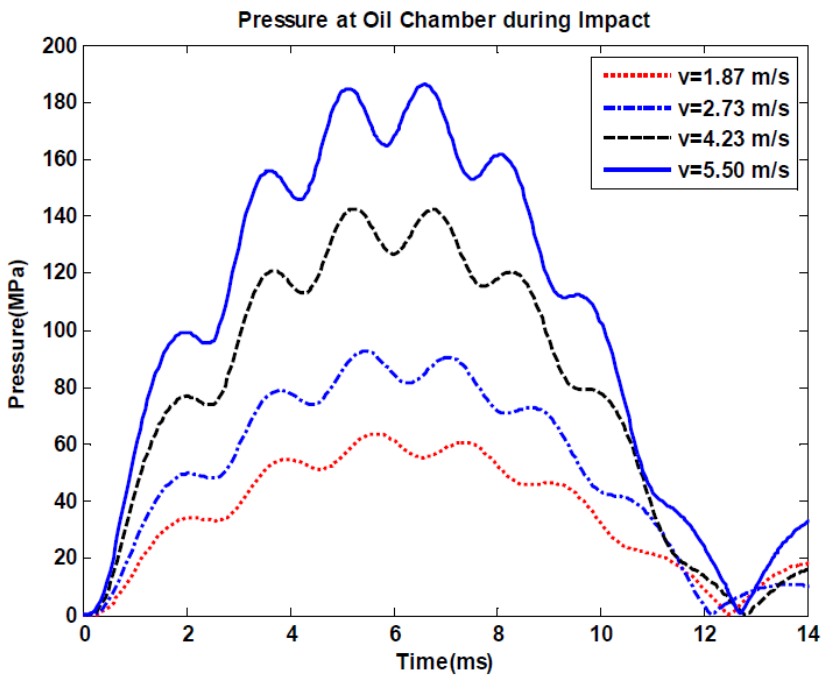

Figure 1.2.3 Pressure vs. Time History at Oil Chamber During Impact for Different Impact Velocities

In another study, Changki Cho investigated a dynamic impact model for a pile-driver breech fatigue system [23]. His aim was to obtain the fundamental characteristics of a currently used system and to improve the hardware. In order to achieve a desirable impact behavior of the pile driver system, he conducted a non-linear analysis of the hardware with good and efficient contact force model. He divided the pile driver system into lumped mass model and analyzed the system by using equations of motions via solving by MATLAB. He carried on his study by using force contact models and done a numerical analysis. Then he conducted a simulation of the system to correlate the results obtained from numerical analysis. Then he done a real time test to prove the study and determine the real impact response of the pile driver. His experimental and theoretical analyses meet well at the result step. For the given parameter sets, the results of the model with non-linear stiffness and non-linear damping combination and the model with only non-linear stiffness differs a little from each other. In addition, it can be easily seen that, as the impact velocity or indentation velocity increases, contact force increases for the both models. The duration time of the indentation reduces as the oil stiffness increases however; the indentation velocity does not affect the duration time. Oil pressure

increases as the impact velocity increases as expected. He proved that the lumped mass parameter method is valid for analyzing the pile driver system. It gives well contact force histories. Moreover, the experimental and simulation results well agreed with each other, which supported the lumped mass parameter method. He has shown that the accuracy of the current impact simulation model with non-linear contact force model is affected by the stiffness of contact area the frictional damping and the stiffness of oil chamber.

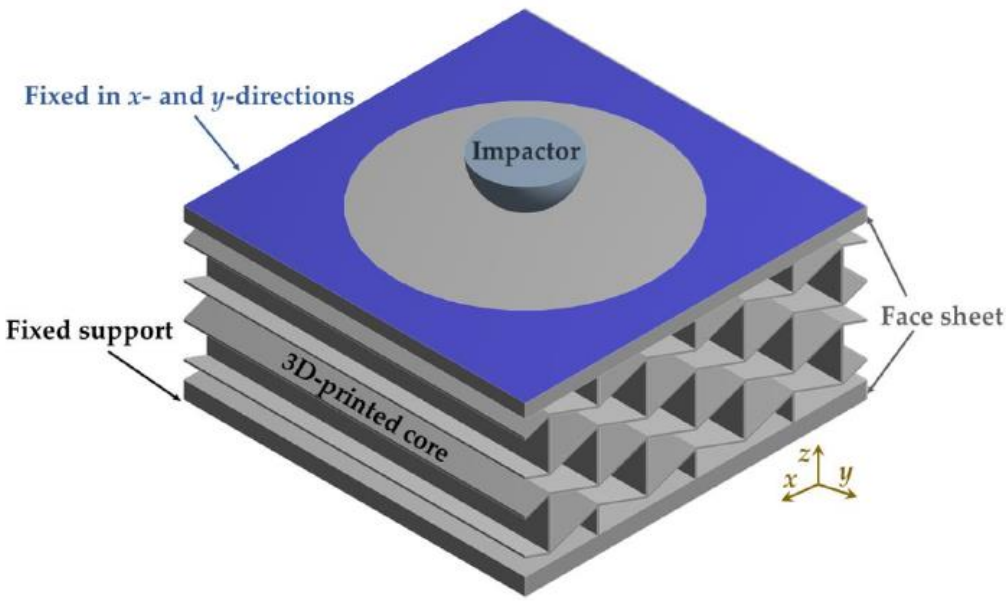

Figure 1.2.4 ANSYS Model for the Low-velocity Impact Analysis

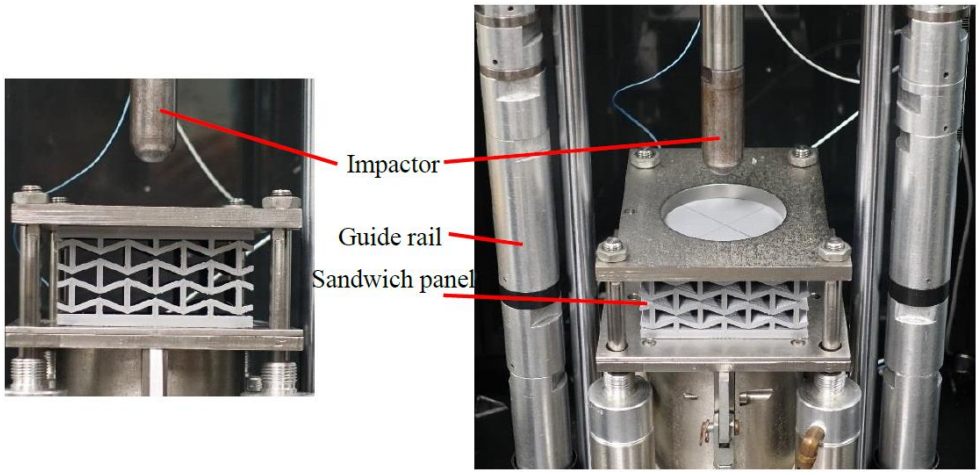

Figure 1.2.5 Low-velocity Impact Test Configuration for Energy Absorption Analysis of 3D Printed Architected Sandwich Panels

Hamidreza Yazdani Sarvestani and Hamed Niknam conducted another study on impact dynamics [24]. They have investigated the energy absorption and structural performance of 3D printed architecture polymeric sandwich panels. They have used semi-analytical and finite element approaches to simulate the behavior of 3D printed sandwich panel and conducted a real time test to evaluate the performance and correlate the results with analytical and numerical results. They built a test specimen with a periodic cellular core and tested under low velocity impact with simply supported boundary condition. From the test and the computational analysis, they have obtained load-displacement curves. The integration of these curves gave them the energy absorption of the sandwich panel. From the results, it is seen that if the core density of the sandwich panel with an eutectic core shape is chosen to be in proper manner with the impact energy, sandwich panels with periodic cellular core can absorb higher levels of impact energy than ones with a rectangular core shape and hexagonal core shapes.

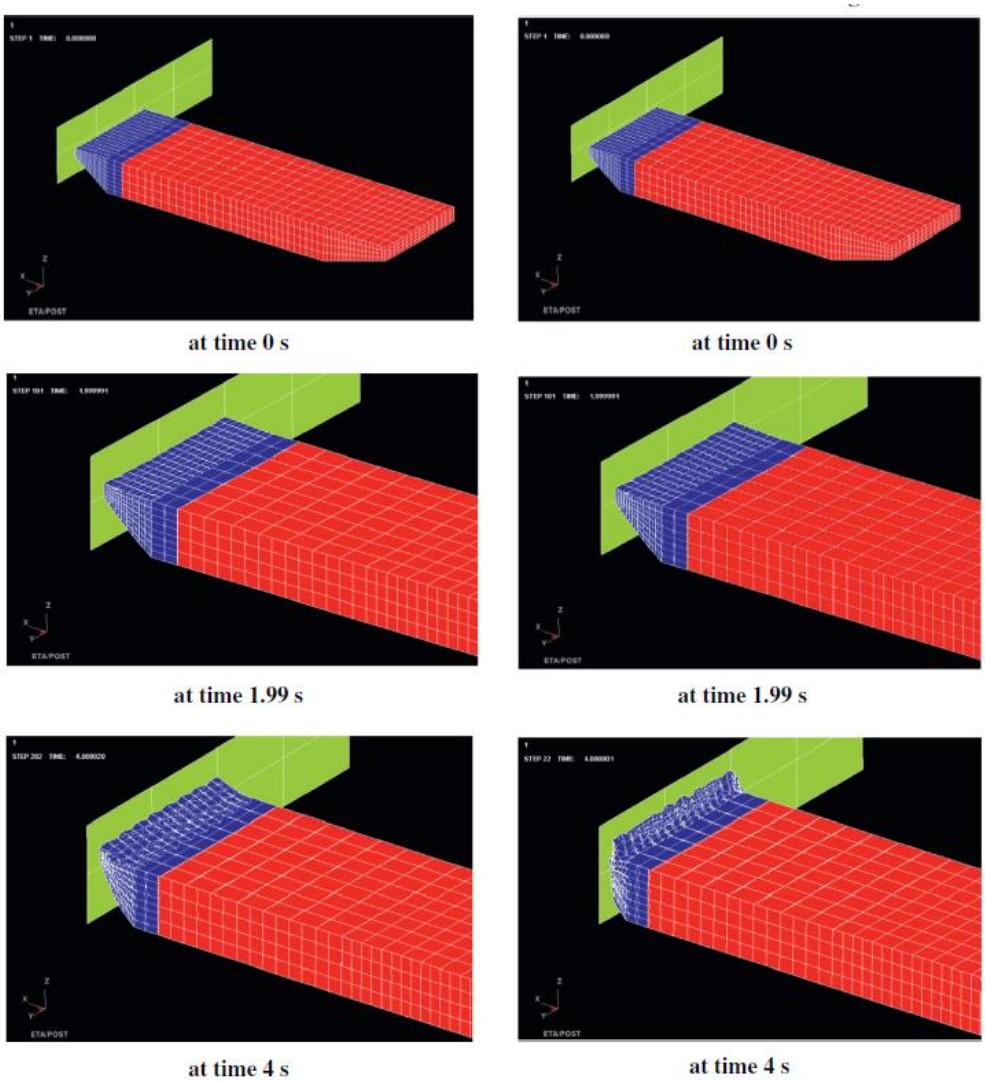

Figure 1.2.6 Collision Damage to the Barge at Speeds of 3 Knots and 5 Knots

Leheta, Elhewy and Sayed Mohamed investigated ship collision against bridges or walls in their study [25]. Especially, they have conducted the impact analysis on barges. According to them, forces and locations of barge impacts plan a significant role on the design considerations of the lock wall. They investigated the occurrence of the impact in two classes, external and internal mechanics. In internal mechanics, the absorbed energy is used for the evaluation of the colliding ship into the wall to ensure whether the ship withstands to the energy or not and in external mechanics, the absorbed energy is used to calculate the effects of the collision into the wall. For both classes, analytical approaches are used. Due to the difficulty of conducting of the real time test of ship to lock wall collision, they have simulated

the occurrence in finite element method, in structural analysis software, LS-DYNA. They have conducted the simulation for two different velocity parameters and recorded the results. From the simulation results, they have obtained the energy absorption of the collision occurrence and time duration of the impact. Due to the requirement of high performance computers to solve the finite element analysis model of collision, they have simplified the model to get an adequate solution. Thus, they have stated that the results may seem reasonable; hence, the model should be verified with real cases.

1.3 Aim of The Study

For moving mechanism, especially, where the motion is and/or has to be limited by design considerations, designers need to stop the kinematic motion by some elements. These elements can be chosen as electrical or mechanical means. Limit switches and motion stop codes can be named as good examples of electrical motion stoppers. When the limit switch is triggered during the motion, it delivers a voltage signal to the motion controller to decide to stop and/or reverse the motion. Thus, the controller sends feedback to the actuator to prevent the collision. However, for mechanical means, it will be a little bit more complex. There should be an obstacle has to be designed to increase the friction to slow down and stop the motion. However, friction control is not beneficial for some other aspects. For example, with the increasing friction, heat will increase and that may wear and damage the materials. In addition, with the increasing heat, stopper parts may stick to each other due to the thermal expansion. Moreover, for high relative velocities, there will be more brake length needed to stop the moving pair before hitting another obstacle or damage itself. A better design consideration will be impact or collision stoppers. In impact stoppers, adjacent mechanic walls are designed for both moving and stationary parts, and the stopper wall attached to the moving part is collided into the stopper wall attached to the stationary part, that stops the motion of the moving one.

Impact motion stoppers are more likely to be an option to choose, however, impact is a complex phenomenon. It is not always easy to understand what happens to the structures then two bodies collide to each other. To understand and control this phenomenon, many analytical models are carried on through the history for different cases. However, there are

unique cases that need attention to investigate and find the optimal design solution to overcome the impact problem.

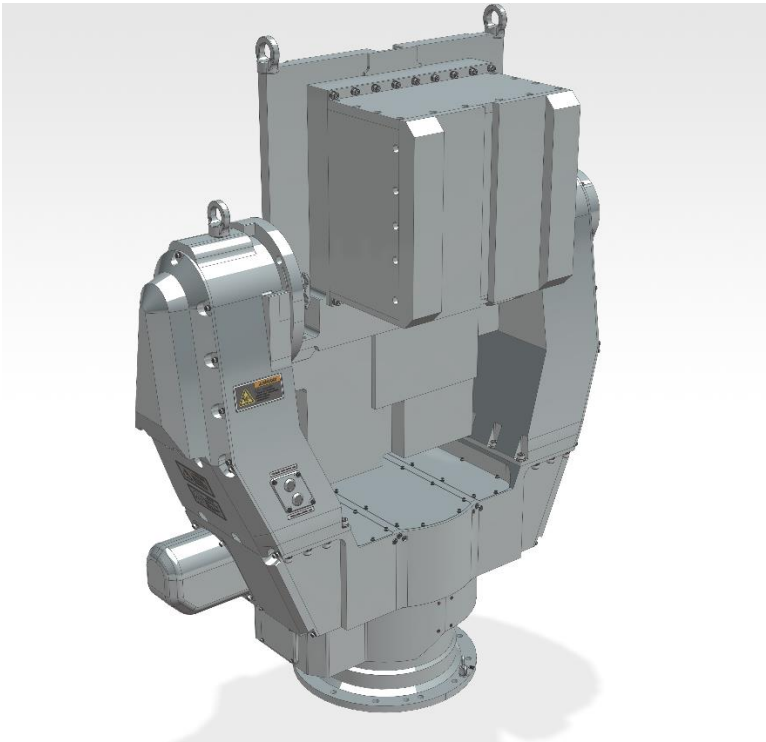

Figure 1.3.1 Antenna Guidance System Model

In this study, an antenna guidance system, designed for a specific purpose for defense industry as seen in, will be introduced. For the work conditions of the system, antenna should roll +74°/-34° around its elevation axis. If it does more that, the limits mentioned above, antenna components may hit to the basement and the basement will reflect the RF signal generated from the antenna backwards, that may affect the measurements. Thus, antenna guidance system is designed to have two mechanical impact stoppers as seen in the Figure 1.3.2 to ensure that the antenna will not exceed to limit.

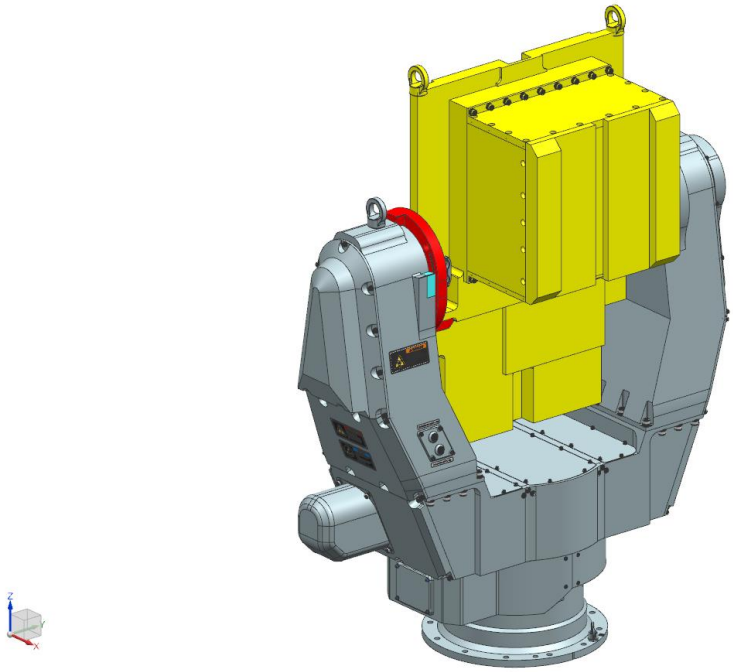

Figure 1.3.2 Antenna Guidance System Model (Colored)

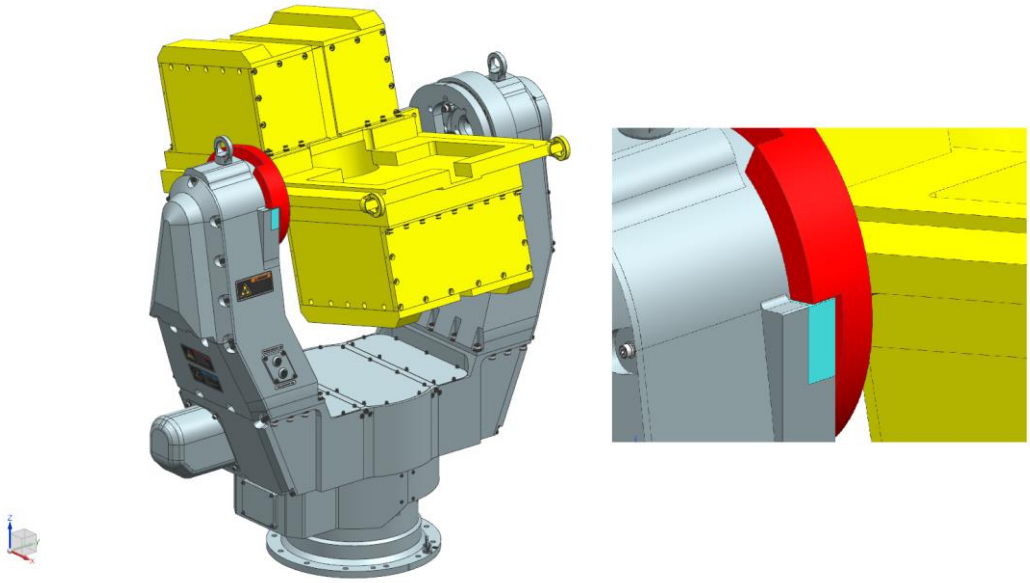

Figure 1.3.3 Antenna Guidance System Model Elevation Positive Limit

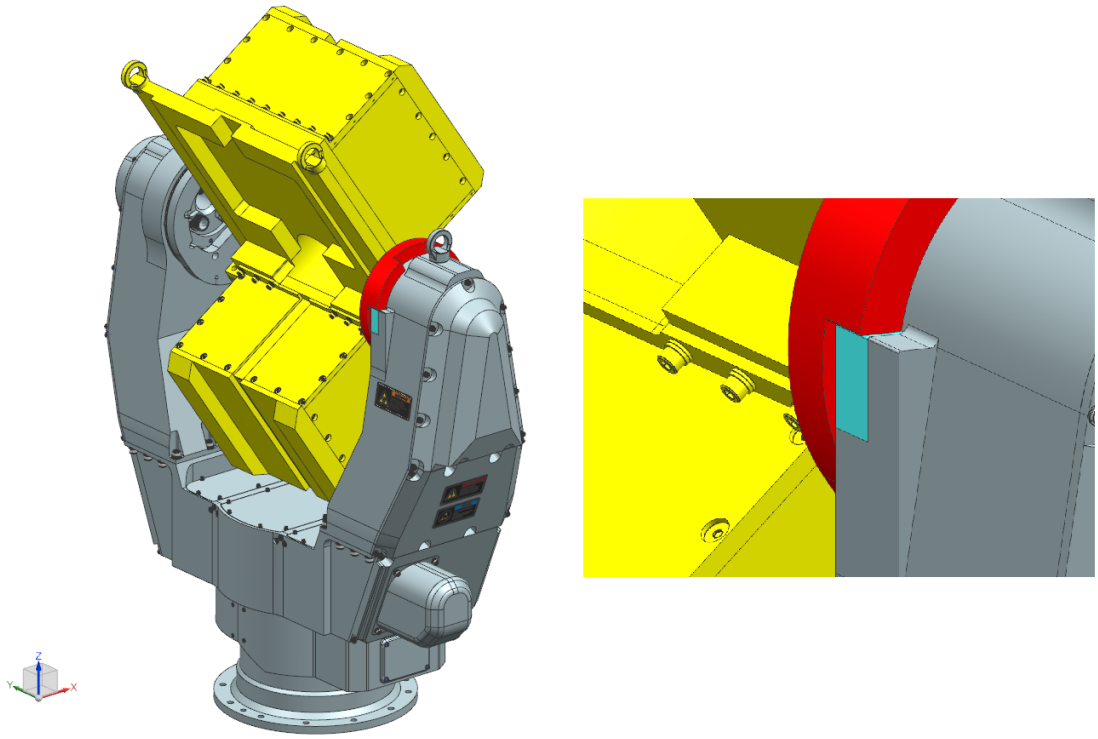

Figure 1.3.4 Antenna Guidance System Model Elevation Negative Limit

It is important to know the parameters of the collision to design an appropriate stopper design. If not, one may design a poor stopper that may broke after the collision that may cause other expensive components to fail. On the contrary, over designed stopper may take much time to design and manufacture, may cost more than expected also increases the mass and complexity of the product.

Before knowing the parameters of impact, one should know the parameters of the colliding parts, such as the mass of the moving section, the energy of the moving section and the materials of colliding stoppers. On this study, as seen in the figure, payload is replaced with the dummy load of the antenna. Dummy load of the antenna has approximately same mass and inertia values. In addition, the payload will be moving with an angular velocity of 30 revolutions per minute just before the collision takes place. The blue (turquoise) parts seen in the Figure *1.3.3* and Figure *1.3.4* are modular stopper parts. The red part is the stopper of the payload. Modular stopper design is preferred for this guidance system to provide ease to assembly and dis-assembly.

Aim of this study is to understand the complex phenomena called impact and have an engineering knowledge to create optimal design for mechanical motion stoppers.

1.4 Thesis Layout

This study includes six main topics, which are introduction part, analytical model part, finite element analysis part, real time test part, comparison part and conclusion parts.

In introduction part, the problem and the influence point is explained briefly. Numerical and experimental studies about impact phenomenon are introduced. Short information about analytical models are examined, and the motivation to study impact phenomenon is summarized.

In the second chapter, point of origin of the impact model, Hertzian Impact Model is explained in detail. Moreover, the other studies based on Hertzian Impact Model are introduced and showed in detail. The comparison of these studies are exampled from previous studies found in the literature.

In third chapter, real time tests are described. Test method and the tools used to conduct an appropriate test are introduced in detail. The data collected from the test are explained and the numerical results from the impact test are shown.

In the fourth chapter, the finite element model to solve impact problem numerically is explained. The correct way to build a finite element model, initial conditions, boundary conditions and mesh setting on ANSYS/Mechanical software is judged, and the numerical results from simulation results are shown.

In the fifth chapter, the results of the previous three chapters are compared with each other.

In the last chapter, the work done up to the end of the study is summarized and the points which will be improved are mentioned. The effort to improve the study and the future work can be carried on about the topic is discussed.

2 MATHEMATICAL MODELLING

2.1 Hertzian Impact Theory

As we discussed above, impact or collision is a complex phenomenon that occurs in milliseconds and it is not an easy task to capture all the behavior of the colliding materials. Therefore, impact texture need to be investigated deeply to discover the nature of itself. To achieve this, up to now, many studies are carried on to illuminate the impact theory. Most of the studies are narrowed down to clarify the special cases of colliding materials. However, some of these studies can be said to have a general meaning for scientist and/or engineers to enlighten their designs or studies. These studies may be said to be started with Hertzian Contact Theory. In 1881, Heinrich Hertz explained his new approach about colliding solids, which of two has spherical shapes. Moreover, Hertz investigated the deformation of the solids colliding each other, and analytically, showed the contact force between two colliding solid spheres. Therefore a term, tribology has been generated from the Hertz's Theory that Hertzian Contact Stress, which refers to the stress area where occurs near the contact point. Hertz Contact Theory investigates the contact and friction phenomena under colliding and contacting bodies with an analytical solution. In addition, this theory became a pioneer study for other engineers and scientists to develop new concepts and theories. Now on, with the Hertzian Contact Theory, we have many other approaches for contact and collision dynamics to investigate the behavior of colliding or contacting bodies.

He published his work in 1882, with the name of "Über die Berührung fester elastischer Körper", which means "On the contact of elastic solids". In his article, he explained the behavior of colliding spherical solids, while he was working on the optic lenses contacting to each other. Thus, he related the contact force to a non-linear power function of the deformation or indentation of colliding spheres as,

$$F = K * \delta^n$$

2.2 Developed Models from Hertizan Impact Theory

Hertz contact theory is improved for solid, perfectly elastic colliding spheres with no energy dissipation. Bu this is not an applicable concept for engineering, because, due to the nature of friction and heat, some of the energy during the collision is wasted or dissipated, thus, this theory needed an energy dissipation or hysteresis touch. Thus, Kelvin and Voigt introduced new approach with hysteresis damping component in the formula. The Kelvin-Voigt model introduces the material into two sections, one of them is represented with spring, the other one which includes the energy dissipation as damper,

$$\varepsilon_{total} = \varepsilon_S + \varepsilon_D$$
$$\sigma_{total} = \sigma_S + \sigma_D$$

From the above equations, rate of change of the stress and the strain with respect to the time are governed by the equation in the form of,

$$\sigma(t) = E * \varepsilon(t) + \eta * \frac{d\varepsilon(t)}{dt}$$
$$\sigma(t) = E * \varepsilon(t) + \eta * \dot{\varepsilon}$$

If we rewrite the stress-strain rate equation for contact force,

$$F_n = K * \delta + D * \dot{\delta}$$

Where, K is for the contact stiffness and D is for the force dissipation (energy-dissipation) coefficient for the colliding materials. This approach is very simple to apply for different cases and used for many studies in the literature. Kelvin-Voigt model is used to evaluate the vertical forces in a tire in vehicle dynamics and contact between flexible bodies. However, Kelvin-Voigt model does not represent the non-linear behavior of the contact process, it can be said to be applicable for the collisions with high impact velocity.

s

Especially, Hertz Contact Theory prompted other scientists to investigate the contact force during collision phenomena. Thus, it can be said that the pioneer study done by Heinrich Hertz is the keystone of contact force during impact. However, because Hertz Law does not count for the energy dissipation, with the addition of the hysteresis-damping coefficient to the formula, Kelvin-Voigt model is said to be the skeleton of the mathematical model for contact force for impact loading. The following studies about impact loading and contact force are modifications due to the cases, material shapes, material stiffness, material hardness etc.

Hunt and Crossley reworked on the Kelvin-Voigt model to examine the hysteresis damping to express the non-linearity of the whole contact process. In their work, they simulated a forced vibro-impact system to define the hysteresis damping, and they concluded that, the contact force could be evaluated as,

$$F_n = K * \delta^n + \chi * \delta^n * \dot{\delta}$$

They stated that the exponent coefficient of damping deformation must be equal to the exponent coefficient of the spring deformation, and they explained the hysteresis-damping coefficient as,

$$\chi = \frac{3}{2} * \frac{K}{\dot{\delta}_0} * (1 - c_r)$$

With the Hunt and Crossley improvement to the impact force equation, many studies revealed and many approaches are created. In the Table *2.2.1*, the scientist worked on the impact force topic and the result of their studies are examined. The results of the mathematical models will be given in the conclusion chapter of this study with the given parameters of the collision test done.

Table 2.2.1 Contact-Force Models

Contact-Force Model	**Constitutive Law**	**n**	**m**	**χ**
Hertz	$F = K * \delta^{3/2}$	$3/2$	-	-
Kelvin-Voigt	$F_n = K * \delta + \chi * \delta * \dot{\delta}$	1	1	-
Hunt-Crossley Marefka-Orin	$F_n = K * \delta^{3/2} + \chi * \delta^{3/2} * \dot{\delta}$	$3/2$	$3/2$	$\frac{3}{2}\frac{K}{\dot{\delta}_0}(1 - c_r)$
Herbert-McWhannel	$F_n = K * \delta^{3/2} + \chi * \delta^{3/2} * \dot{\delta}$	$3/2$	$3/2$	$\frac{6\,K\,(1 - c_r)}{\dot{\delta}_0\,((2\,c_r - 1)^2 + 3)}$
Lee-Wang	$F_n = K * \delta^{3/2} + \chi * \delta^{3/2} * \dot{\delta}$	$3/2$	$3/2$	$\frac{3}{4}\frac{K}{\dot{\delta}_0}(1 - c_r)$
Anagnostopoulos	$F_n = K * \delta + \chi * \delta * \dot{\delta}$	1	1	$2\frac{-lnc_r}{\pi^2 + (lnc_r)^2}\sqrt{K\,m_{eff}}$
Lankarani-Nikravesh	$F_n = K * \delta^{3/2} + \chi * \delta^{3/2} * \dot{\delta}$	$3/2$	$3/2$	$\frac{3}{4}\frac{K}{\dot{\delta}_0}(1 - c_r^2)$
Ristow	$F_n = K * \delta^{3/2} + \chi * \delta * \dot{\delta}$	$3/2$	1	Empirical Value
Tsuji et al.	$F_n = K * \delta^{3/2} + \chi * \delta^{1/4} * \dot{\delta}$	$3/2$	$1/4$	$\alpha\sqrt{K\,m_{eff}}$
Lee-Herrmann	$F_n = K * \delta^{3/2} + m_{eff}\chi * \delta * \dot{\delta}$	$3/2$	1	Empirical Value
Shafer et al.	$F_n = K * \delta^{3/2} + \chi * \delta * \dot{\delta}$	$3/2$	1	Empirical Value
Jankowski	$F_n = K * \delta^{3/2} + \chi * \delta^{1/2} * \dot{\delta}$	$3/2$	$1/2$	$\frac{-2\,K\,lne_r}{\dot{\delta}_0\sqrt{\pi^2 + (lne_r)^2}}$
Zhiying-Qishao	$F_n = K * \delta^{3/2} + \chi * \delta^{3/2} * \dot{\delta}$	$3/2$	$3/2$	$\frac{3\,K\,(1 - c_r^2)e^{2(1-c_r)}}{4\,\dot{\delta}_0}$
Bordbar-Hyppanen Schwager-Porchel	$F_n = K * \delta^{3/2} + \chi * \delta^{0.65} * \dot{\delta}$	$3/2$	0.65	Empirical Value
Gonthier et al. Zhang-Sharf	$F_n = K * \delta^{3/2} + \chi * \delta^{3/2} * \dot{\delta}$	$3/2$	$3/2$	$\frac{1 - c_r^2}{c_r}\frac{K}{\dot{\delta}_0}$
Flores et al.	$F_n = K * \delta^{3/2} + \chi * \delta^{3/2} * \dot{\delta}$	$3/2$	$3/2$	$\frac{8}{5}\frac{K}{\dot{\delta}_0}\frac{(1 - c_r)}{c_r}$
Gharib-Hurmuzlu	$F_n = K * \delta^{3/2} + \chi * \delta^{3/2} * \dot{\delta}$	$3/2$	$3/2$	$\frac{1}{c_r}\frac{K}{\dot{\delta}_0}$
Brilliantov et al.	$F_n = K * \delta^{3/2} + \chi * \delta^{1/2} * \dot{\delta}$	$3/2$	$1/2$	$\frac{(3\eta_2 - \eta_1)^2}{(3\eta_2 - \eta_1)}\frac{(1 - \vartheta)(1 - 2\vartheta)}{KE\vartheta^2}$
Hu-Guo	$F_n = K * \delta^{3/2} + \chi * \delta^{3/2} * \dot{\delta}$	$3/2$	$3/2$	$\frac{3}{2}\frac{1 - c_r}{c_r}\frac{K}{\dot{\delta}_0}$

3 IMPACT TEST

In this chapter, test case, test preparation and real time impact test of the described geometry and conditions of the system mentioned above in the first chapter is explained in detail. The test set-up is introduced and the tools and gauges used to measure the results are mentioned briefly. Then the test cases are discussed and finally the test results are showed in detail for different parameters of the impact test.

3.1 Test Layout and Set-Up

The real time impact test is carried on to see what happens to the stopper parts under impact loading. First, appropriate and well-qualified mechanic parts are manufactured to build the main antenna guidance system. After the assembly of the antenna guidance system, stopper parts and their manufacturing tolerances are considered to fit the space left in the arm of the antenna guidance system. Then, to see the materials properties effect to the impact load, 3 stopper parts are manufactured with 3 different materials, one is aluminum alloy AL-6061-T6, one is stainless steel AISI 304 and the last one is titanium alloy Ti-6Al-4V. Comparison of the mechanical properties of these materials are given in the Table *3.1.1*.

Table 3.1.1 Mechanical Properties of Selected Materials

Property / Material	**AL 6061 – T6**	**Ti-6Al-4V**	**AISI 304**
Density (g/cc)	2.70	4.43	8.00
Hardness, Vickers	107	349	129
Tensile Strength, Yield (MPa)	276	880	215
Tensile Strength, Ultimate (MPa)	310	950	505
Modulus of Elasticity (GPa)	68.9	113.8	193
Poisson’s Ratio	0.330	0.342	0.290

The antenna guidance system is a complex gimbal, which allows the antenna to rotate around the three main axes. However, in our model, due to the license and secrecy issues with the company, third rotational motion is suppressed and replaced in a dummy load, which is not an important parameter for the test case. As seen in the Figure *3.1.1*, the whole antenna and

the roll motion motor is substituted with a dummy load with same center of gravity and same inertial properties.

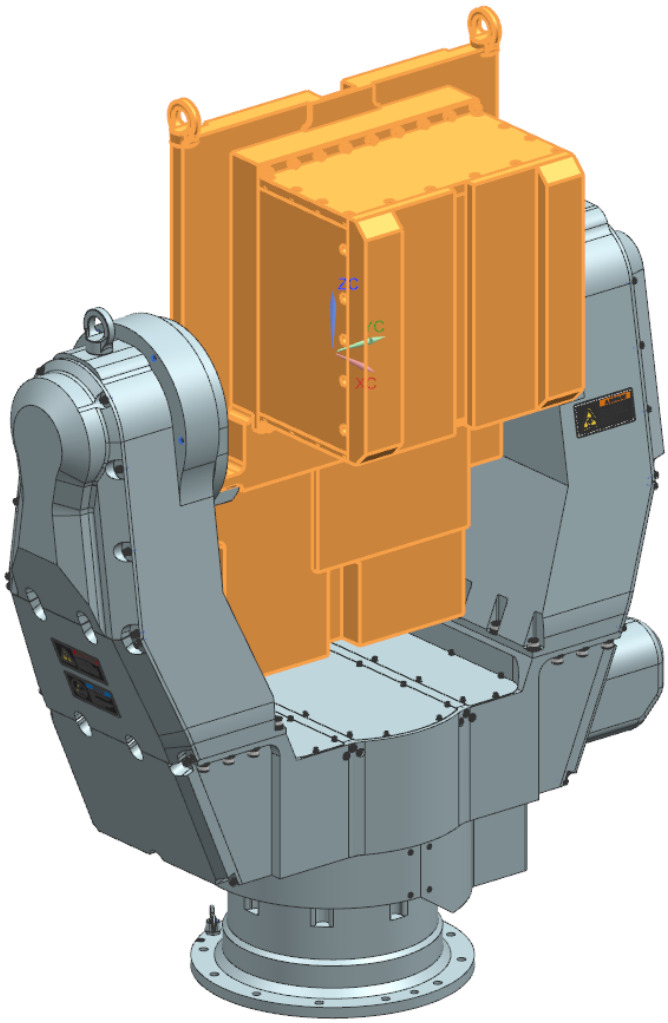

Figure 3.1.1 Test Assembly Model

In the Figure *3.1.1*, the highlighted model seen in orange color is the dummy load prepared to substitute the roll motor and the antenna geometry. The antenna guidance system has three degrees of rotational motion and the roll motor, which is suppressed, has the rotational motion in the x-axis. The yaw motion is performed in the z-axis via a gearbox from the bottom side of the system. In addition, the elevation or pitch motion is supplied by a reducer in the right arm at y-axis. The impact stoppers are located at the elevation motion to introduce the impact force during the collision occurrence.

The above figure is the design picture of the test arrangement. In the Figure *3.1.2*, the manufactured test system can be seen. The dummy antenna and the roll motor is assembled and strain gauge mounted stopper is placed to the right position. For the ease of access to the motor drivers and cables, the unnecessary mechanical parts and covers are disassembled.

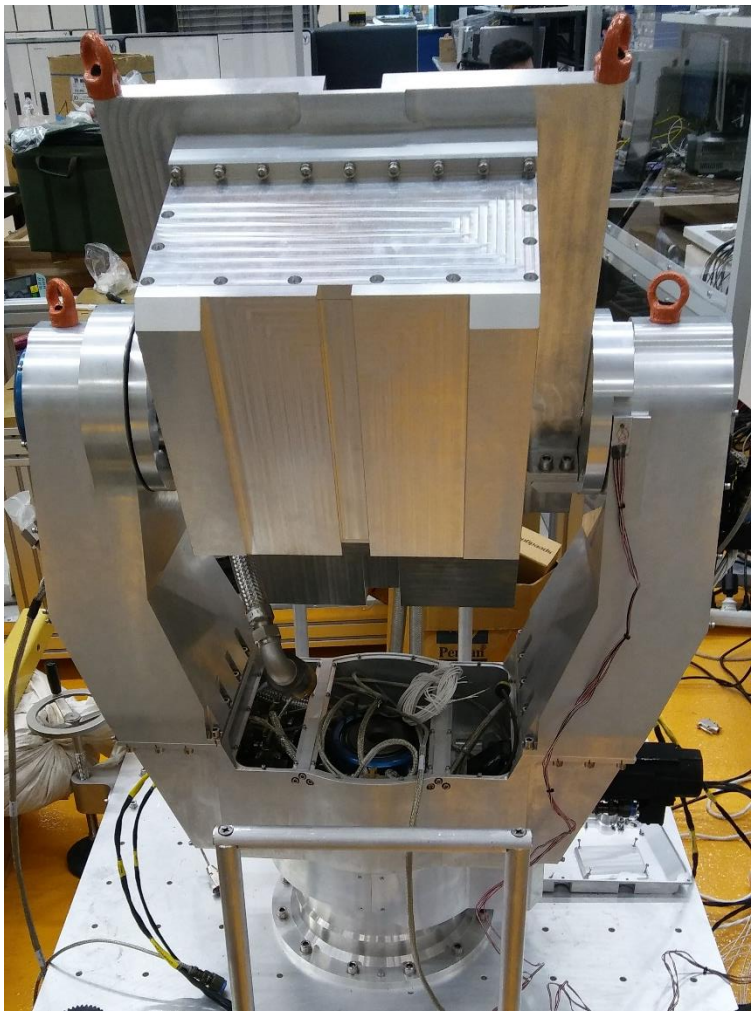

Figure 3.1.2 Assembled Test System

To measure the strain level of the mechanical parts during elastic and/or plastic deformation, some gauges or tools are needed. In general, to measure the elastic deformations in the materials surfaces, wire strain gauges and laser strain gauges are used widely. Since the laser strain gauges are so expensive and sensitive devices, strain gauges are the most common tools to measure deformations in the materials. However, strain gauges can be used only for

elastic deformation. Thus, the placement of strain gauge is an important manner for the results of the tests. With an engineering foresight, at the upper edge of the stopper, the thin wires of the strain gauge may be exposed to plastic deformation, thus, the gauge should be placed at a secure distance below the upper edge, where the impact occurs. The position of the gauge can be seen in the Figure *3.1.3*.

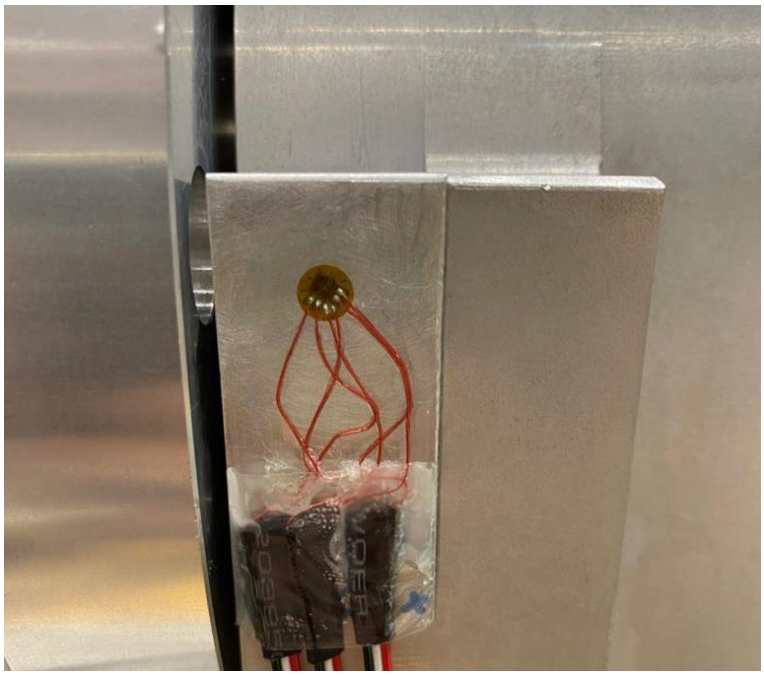

Figure 3.1.3 Strain Gauge Position on the Stopper

Selection of the strain gauge is an important parameter to ensure the reliability of the test results. Thus, a detailed research in the literature and the products in the company catalogs have been conducted. After the research, it has been decided to select a tee rosette strain gauge to measure the strain on the stopper surface in three different directions. This gives an advantage to measure three different strains in three different directions and calculate the von-Misses stress at the surface at the point where the gauge is located on. With all these information, from Vishay's Product Group, Micro Measurements, G1350 series tee rosette strain gauge is chosen. The datasheet of the product can be seen in APPENDIX.

Figure 3.1.4 Strain Gauge and Datasheet

The strain gauge is placed on the stoppers free surface as mentioned above seen in Figure *3.1.3*. The gauge is placed below the contact surface edge due to the probability of plastic deformation at the or near the impact edge. The gauge is mounted 1 cm below the edge and just at the middle portion of the stoppers free surface. The gauge and the wire directions are chosen to be such that, the second channel of the strain gauge shows the upper face (impact face) edge of the stopper. The gauge is mounted with a special adhesive, M-Bond 200 Adhesive Kit, which used for sticking strain gauges to metal surfaces. The datasheet of the adhesive can be found in APPENDIX. Strain gauges are mounted to the stopper surfaces with this adhesive as described in the datasheet.

The strain gauge is mounted by hand thus; the accuracy of the directions of the wires and parallelism of the second channel to the z-axis is low. That situation brings an error source to the results, which is tried to be eliminated via using computer-aided drawings. The gauge direction on the stopper can be seen in Figure *3.1.5*.

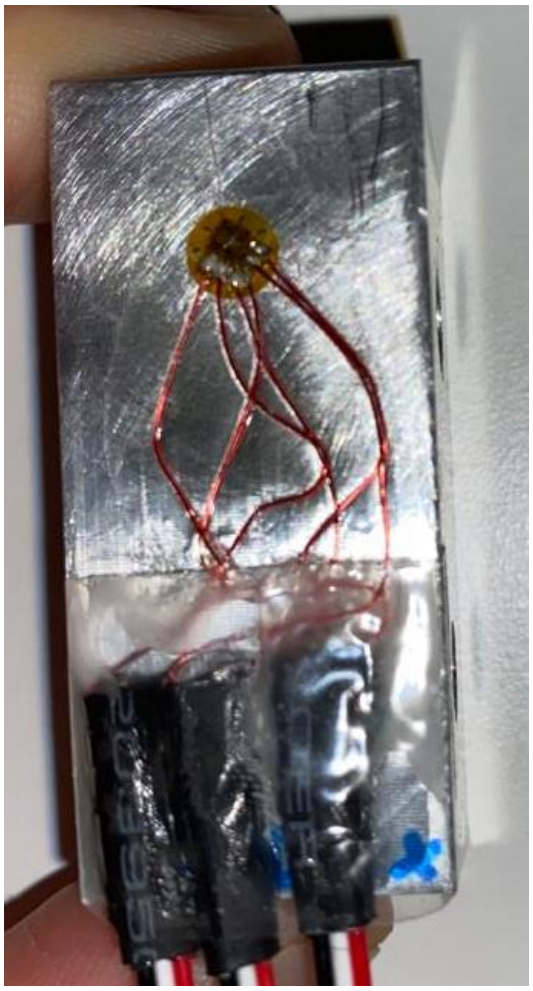

Figure 3.1.5 Strain Gauge Position on Impact Stopper

As seen in the figure above, the gauge's second channel direction is tilted from the z-axis of the system. This misdirection is observed and calculated by using CAD software Siemens NX-12 as seen in Figure *3.1.7* for aluminum, steel and titanium stoppers and the value of deflection is reflected to the results and calculation part of the study. The same procedure is carried for all the aluminum, steel and titanium stopper specimens. Tilt angles are given in Table *3.1.2*.

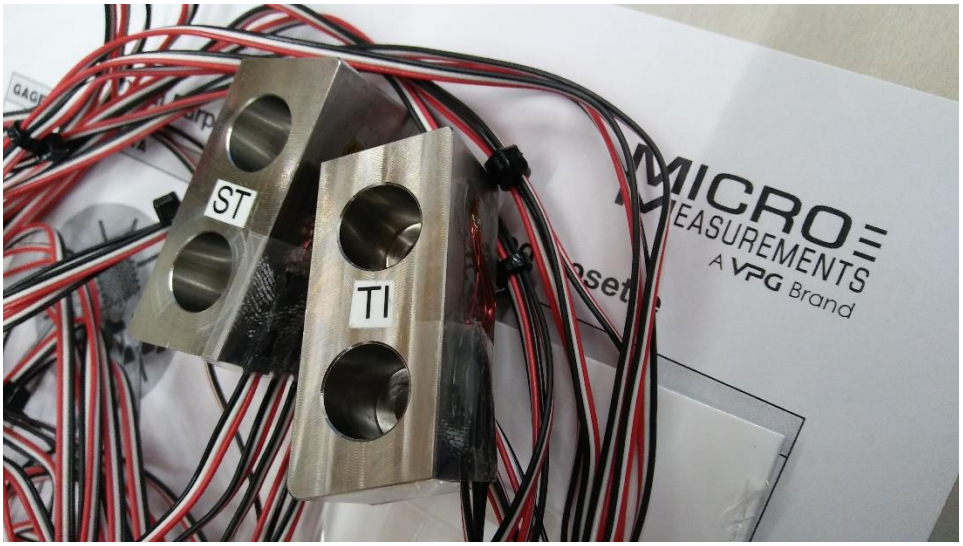

Figure 3.1.6 Stainless Steel and Titanium Alloy Stoppers with Strain Gauges

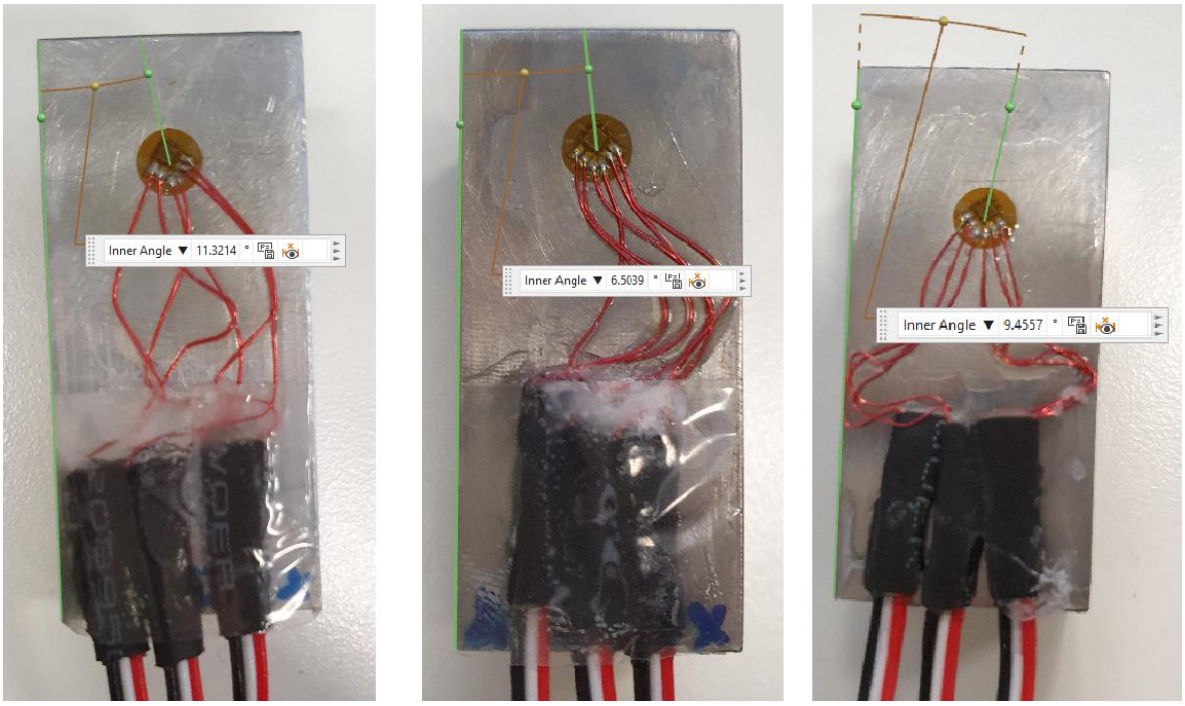

Figure 3.1.7 Tilt Angles of Strain Gauges on Stopper Parts of Aluminum 6061 T6, Titanium Ti-6Al-4V and Stainless Steel AISI 304

Table 3.1.2 Tilt Angles of Strain Gauges on Stopper Parts

Material	AL 6061 – T6	Titanium Ti-6Al-4V	AISI 304
Tilt Angle	11.32°	6.50°	-9.46°

Another important point for conducting a real time impact test is to determine the scenario and the count of the repetition of tests of each scenario and sampling rate of the data. For the function of the antenna guidance system, the antenna may reach to 30-RPM angular velocity to track the obstacles. Thus, for the operation conditions of the antenna guidance system, with a failure of the controller algorithm or motor driver, the antenna may collide to the stoppers with an angular velocity of 30-RPM. Thus, the test should be carried on with 30-RPM velocity to observe the function ability of stoppers. Moreover, to detect the relative angular velocity effect of the collision, the tests at different speeds are considered. Thus, the tests will start at collision with 5-RPM and the angular velocity will be increased by 5-RPM value after each test conducted. At the end of the test sequences, testes should be conducted at six different angular velocity values. In addition, to be sure that the test results are reliable, for each angular velocity value, tests are done for three times to see the variation between them. Thus, total eighteen tests are conducted to see the reaction of the stoppers to the impact load. Photos of the position of stainless steel stopper before, during and just after the collision can be seen in the Figure *3.1.8*.

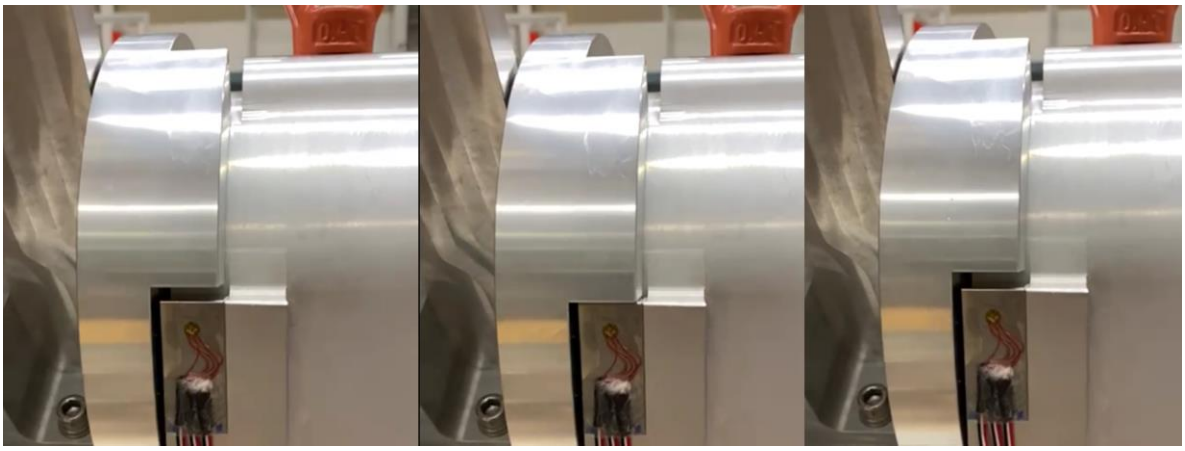

Figure 3.1.8 Stainless Steel Stopper Before, During and After the Impact

3.2 Test Verification

Test method is the most useful method to see the results of an occurrence and take data, but the important point is to be sure that the set-up and the conditions are met quite well. To achieve the consistency of the tests carried on, and to be sure that the strain gauges and the software set-up is configured in the right way, a basic cantilever beam test is conducted. A known aluminum beam sample made from AL-6061-T6 is tested with the stain gauge used for the collision tests and configured with the same procedure and settings. The 463 mm long, 57.5 mm wide and 3 mm thick beam is fixed to a test table and G1350 series 120-ohm strain gauge is stocked to its upper surface as seen in Figure *3.2.1*, Figure *3.2.2* and Figure *3.2.3*.

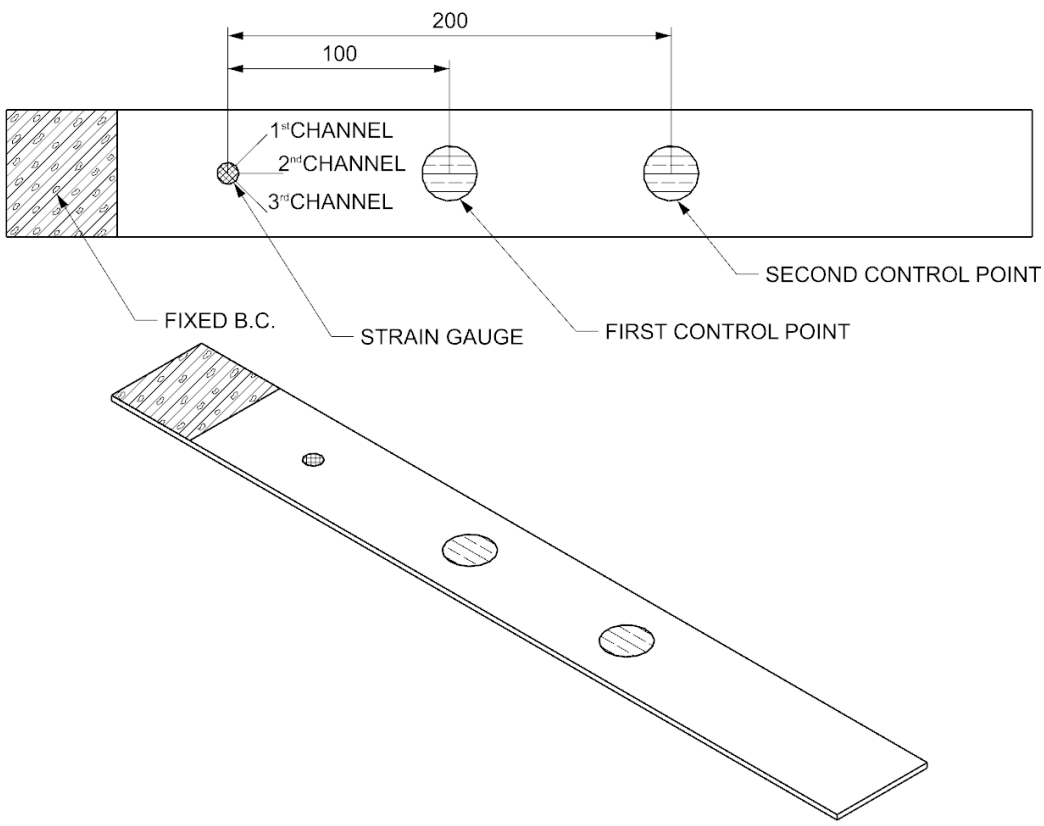

Figure 3.2.1 Strain Gauge Verification Test Set-Up Drawing

Figure 3.2.2 Strain Gauge Verification Test Set-Up for Distance 200 mm

To create a bending moment on the beam seen above, a known mass is positioned on the beam. To see the bending moment and to judge in the proper way, two control points are created, and the mass piece is positioned on these two distinct points. The control points are 100 mm apart from each other and the first control point, which is closer to the strain gauge, is 100 mm away from the strain gauge as seen in Figure *3.2.1*. The gear shaped dummy piece in Figure *3.2.2*, which is used to represent the known mass, is measured on a precise weighting instrument and it is seen that the dummy piece has 472 grams of weight, which can be seen in Figure *3.2.4*.

Figure 3.2.3 Strain Gauge Verification Test Set-Up for Distance 100 mm

Then, basic bending moment calculation is carried on to evaluate the theoretical strain value for the beam subjected to the dummy piece load described above:

$$M = F_m * r = m * g * r$$

$$\sigma = \frac{M * c}{I}$$

$$I = \frac{1}{12} * b * h^3$$

$$\sigma = E * \varepsilon$$

From these above equations, strain can be evaluated as:

$$\varepsilon = \frac{12 * m * g * r * c}{b * h^3 * E}$$

Where, m is mass, g is earth gravity, r is distance of mass from strain gauge perpendicular to moment direction, c is distance of strain gauge from neutral axis of beam tested, b is beam width, h is beam thickness and E is elastic modulus of the beam. After evaluating of the equation above:

$$\varepsilon_{10mm} = 76.66 \ \frac{\mu u}{u}$$

$$\varepsilon_{20mm} = 153.33 \ \frac{\mu u}{u}$$

This strain value is valid for channel 2 of strain gauge. To evaluate the other channels, one should perform coordinate transformation, however, this result can be said to be enough to see the performance of strain gauge and test set-up.

Figure 3.2.4 Mass of Dummy Piece

After hand calculations, the strain value for each case is evaluated from the cantilever beam test and data acquisition system. The results can be seen in Figure *3.2.5*, Figure *3.2.6* and Figure *3.2.7*.

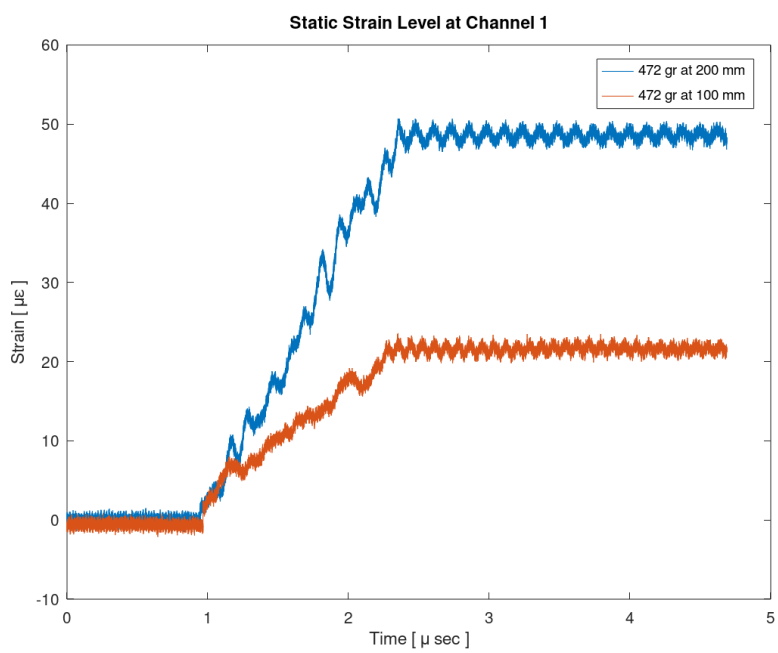

Figure 3.2.5 Static Strain Level in Channel 1 for Both Control Points

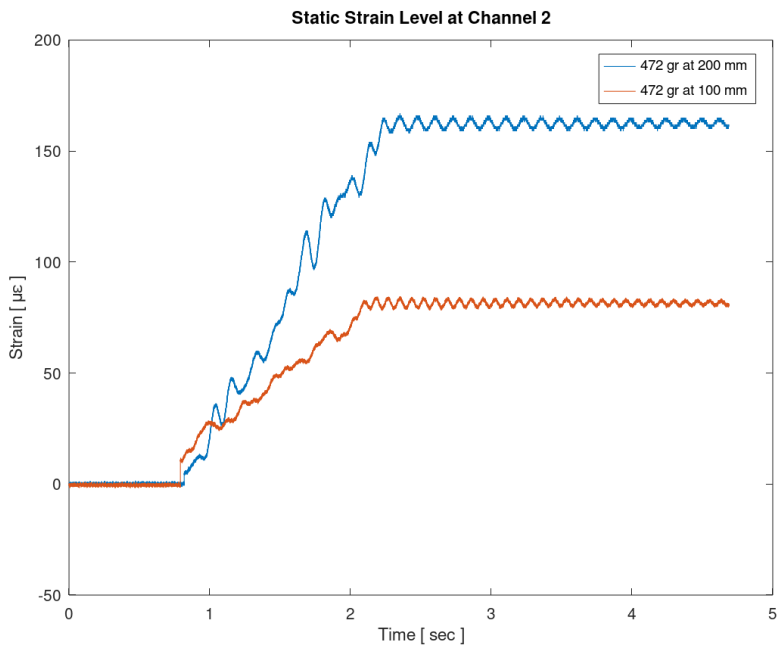

Figure 3.2.6 Static Strain Level in Channel 2 for Both Control Points

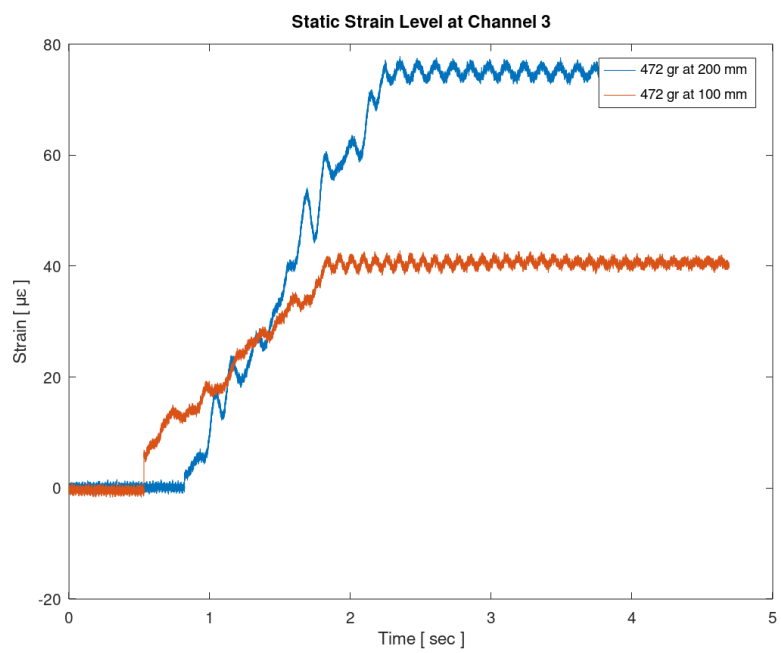

Figure 3.2.7 Static Strain Level in Channel 3 for Both Control Points

The results oscillates for a while because the dummy mass is dropped by hand as gently as possible nevertheless this procedure creates a wavy behavior and output for the data read

from data acquisition system. After the system converged and the oscillations settled up, the results and the hand calculation results are expressed in Table *3.2.1*.

Table 3.2.1 Comparison of Test Results and Hand Calculations

Channel and Position	**Test Result ($x10^{-6}$)**	**Hand Calculation ($x10^{-6}$)**	**Error %**
Channel 1 at 100 mm	21.9	-	-
Channel 1 at 200 mm	49.2	-	-
Channel 2 at 100 mm	81.7	76.66	6.17
Channel 2 at 200 mm	163	153.33	5.93
Channel 3 at 100 mm	40.5	-	-
Channel 3 at 200 mm	75.2	-	-

For channel 1 and channel 2, there is other phenomena like torsion strain and shear strain are taken into account and these kind of stresses and strains are dominant and needs concentrated study on these calculations thus, they are not conducted. However, for channel 2, the results of the test and readings from the strain gauge meets well. As a conclusion for strain gauge test, the procedure conducted to stick the strain gauges to the stoppers and readings from the collision tests can be said to be convenient to compare and conclude. The error may be developed due to the misdirection of strain gauge. The gauge is wanted to stick to the beam surface in which the direction of channel 2 should be parallel to the beam length, however, unfortunately, due to the manual labor error; the direction of channel 2 on beam surface may be mismatched.

3.3 Collision Test Results

After consecutive eighteen collision tests of stopper, slightly precise results are obtained. Before the results are printed, a useful MATLAB code is generated to obtain record and print the graphs of impact occurrence in time domain. The code generated is given in APPENDIX. The test data is recorded by a data acquisition hardware produced by LMS, and processed in data acquisition software generated by Siemens. In the acquisition software, the data is recorded in 12800 Hz to see the reaction of the strain gauge detailed.

The results of the tests are introduced separately for each material. Firstly, aluminum specimen is tested at 5-RPM and test speed is increased to 30-RPM by 5-RPM increments. For each angular velocity, test is repeated three times to check the precision of recordings and the strain gauge ability. Then the same procedure is carried on for steel and titanium specimens. All the data obtained from tests are recorded and published separately.

Since the strain gauges have three distinct wires due to its tee rosette configuration, three different data set obtained from each test. For each case, the data collected from acquisition system have been analyzed and grouped with respect to which channel it belongs. After all the tests are conducted, all three-test results for each channel published in the same figure. Then, result are averaged for each channel and displayed. All data from the data acquisition system is recorded as strain read on stopper versus time.

Here, analyzing the meaning of terms Channel 1, Channel 2 and Channel 3 has importance on understanding the response of the stopper to collision load given. As mentioned above, strain gauge has three channels, measuring strain in three directions, first one is at 45 degree, second one is at 90 degree and the third one is at 135 degree in coordinate system seen in the Figure *3.3.1*.

Thus, the results are shown below, from Figure *3.3.2* to Figure *3.3.10*, separate channel results can be seen for each stopper.

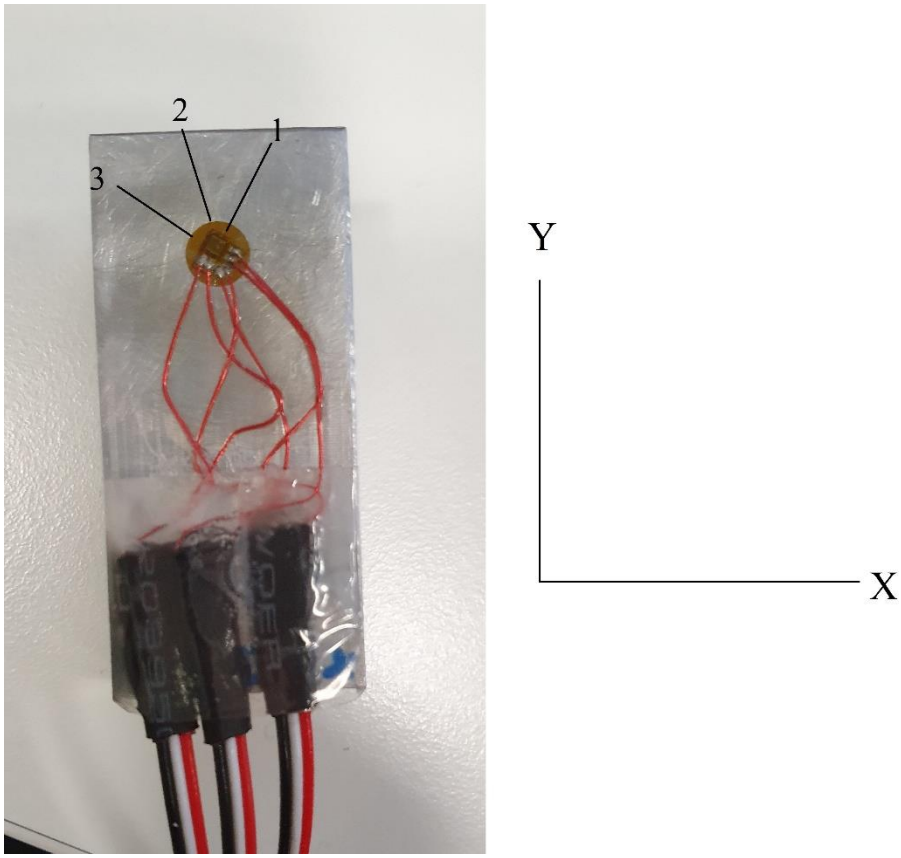

Figure 3.3.1 Coordinate System and Channel Directions of Strain Gauge

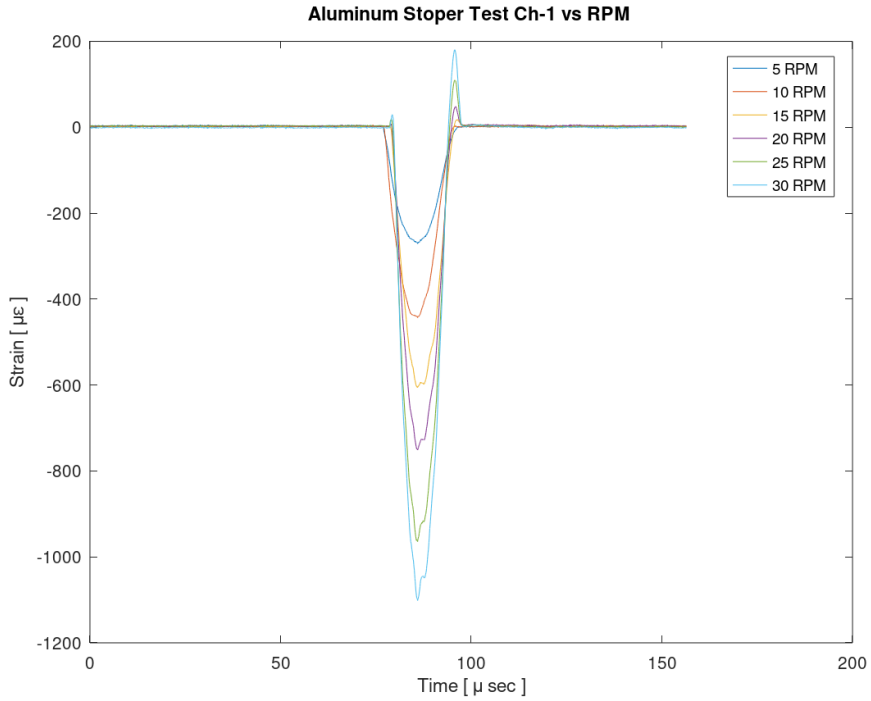

Figure 3.3.2 Aluminum Stopper Channel 1 Test Results

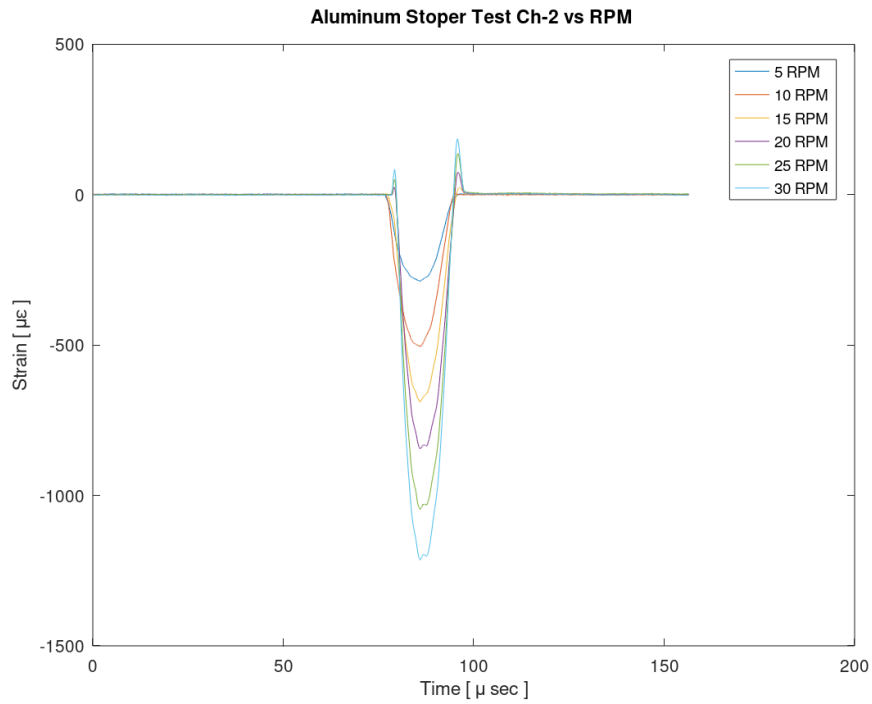

Figure 3.3.3 Aluminum Stopper Channel 2 Test Results

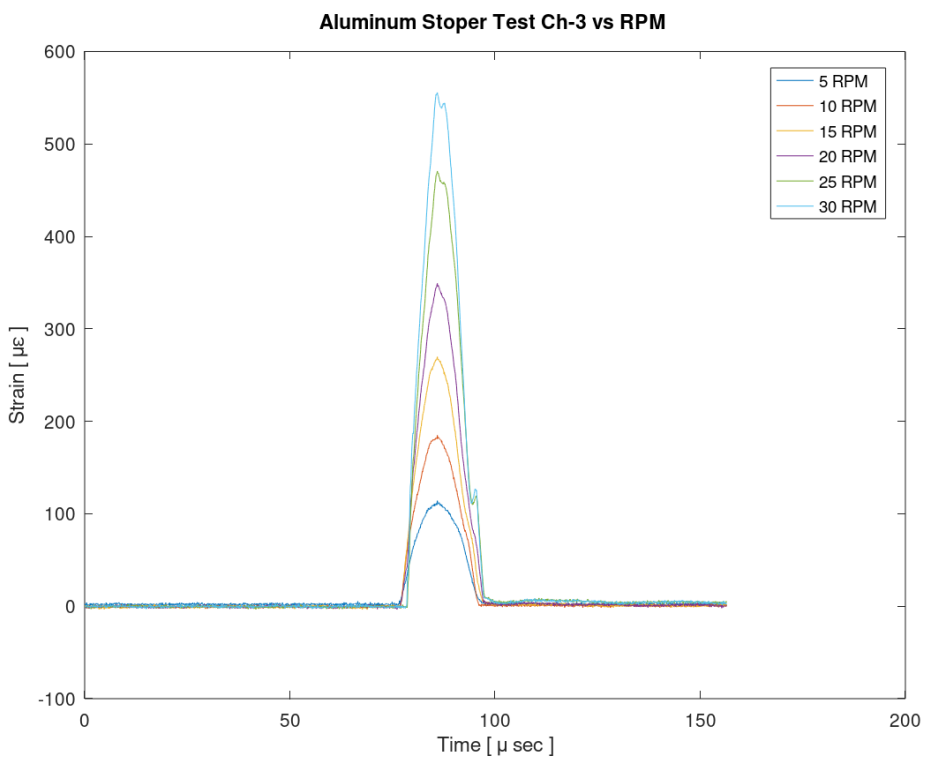

Figure 3.3.4 Aluminum Stopper Channel 3 Test Results

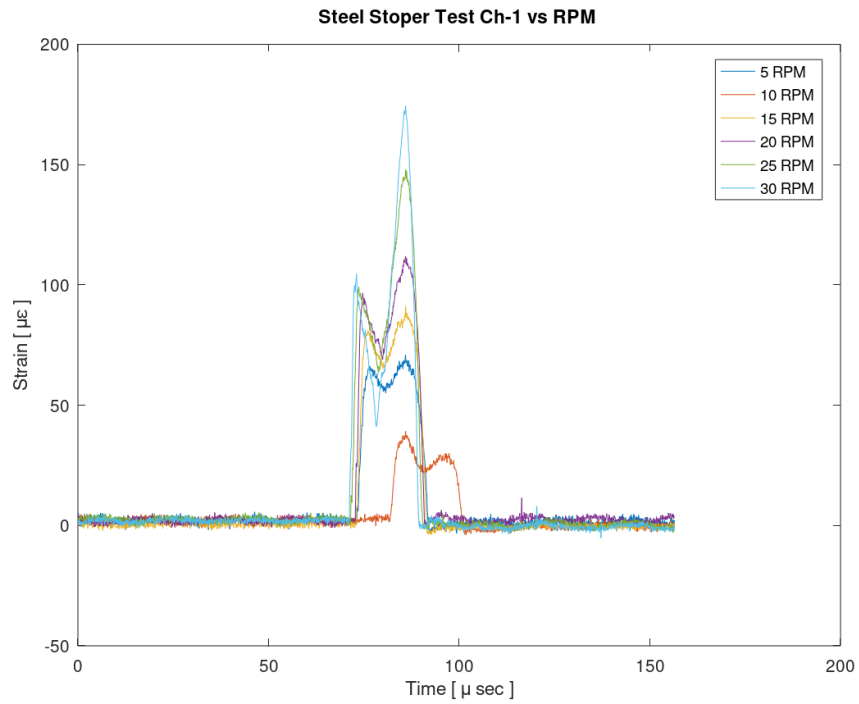

Figure 3.3.5 Steel Stopper Channel 1 Test Results

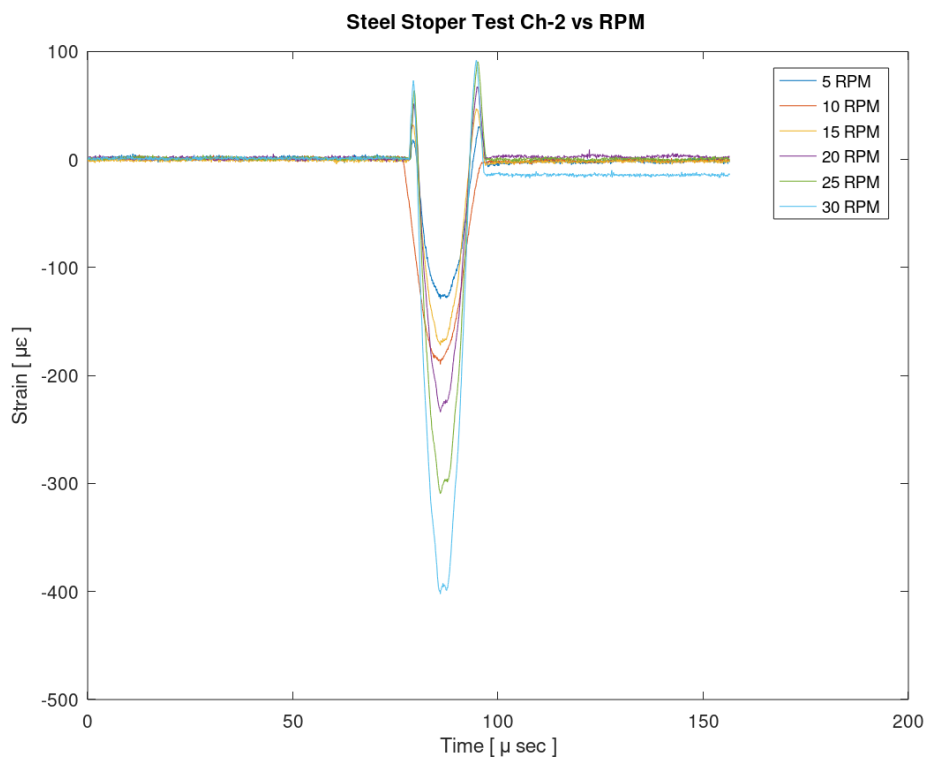

Figure 3.3.6 Steel Stopper Channel 2 Test Results

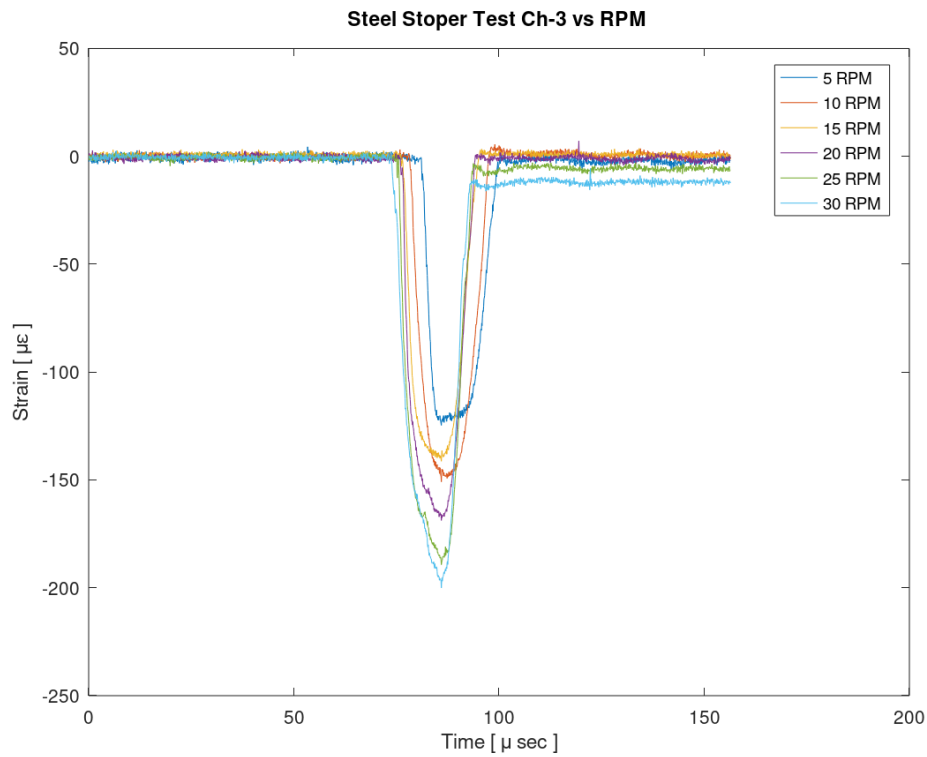

Figure 3.3.7 Steel Stopper Channel 3 Test Results

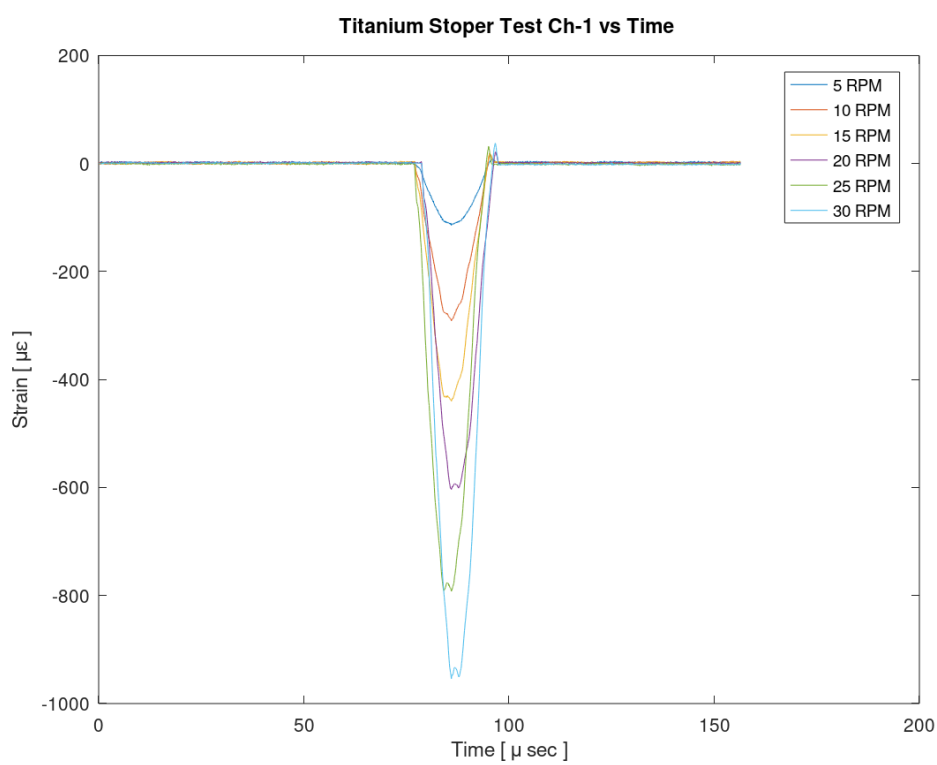

Figure 3.3.8 Titanium Stopper Channel 1 Test Results

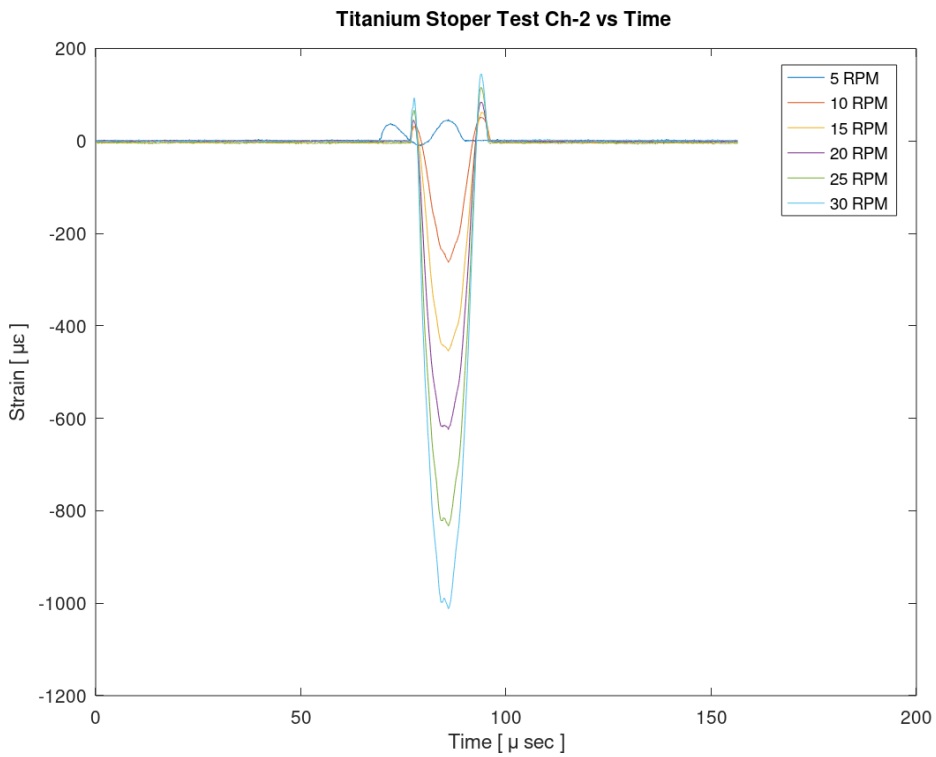

Figure 3.3.9 Titanium Stopper Channel 2 Test Results

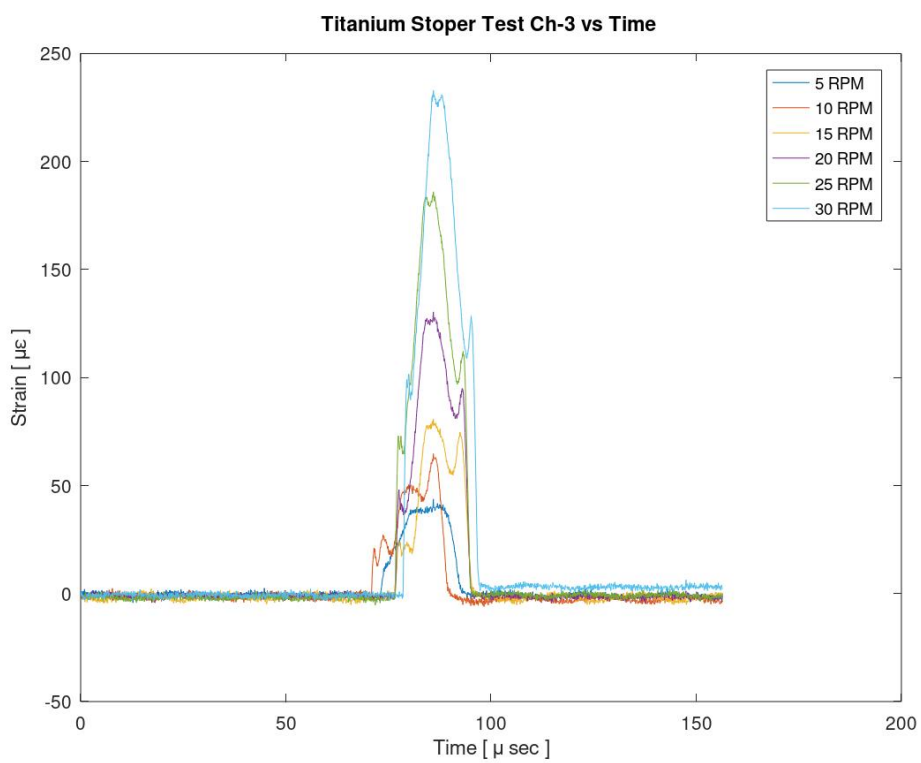

Figure 3.3.10 Titanium Stopper Channel 3 Test Results

In addition, the results obtained are expressed in one graph to see the difference between the results of different materials. In these graphs, the peak results for each channel and each material are expressed with respect to angular velocities of collision, seen in Figure *3.3.11*, Figure *3.3.12* and Figure *3.3.13*.

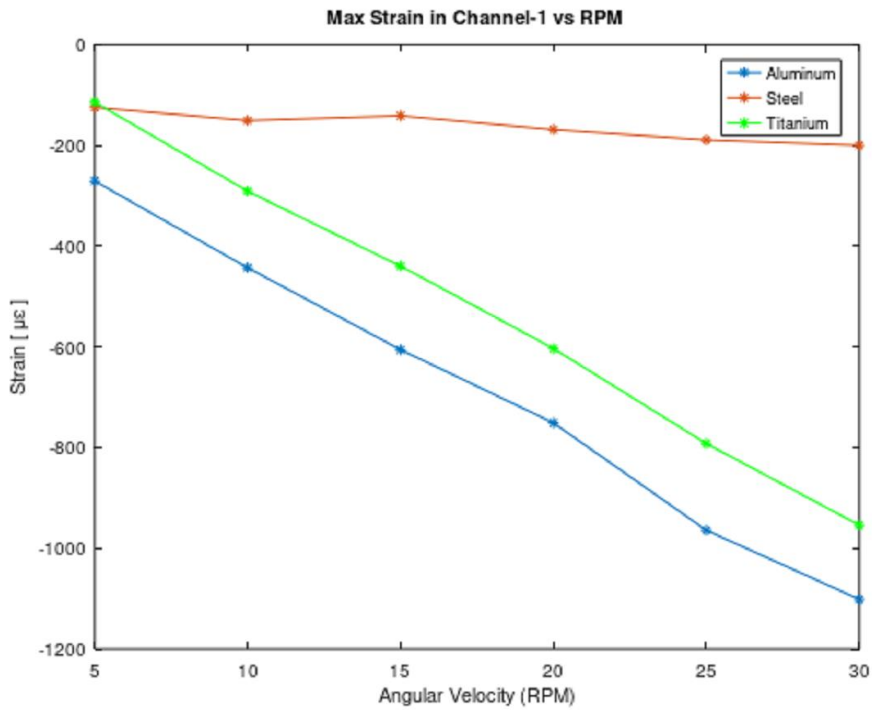

Figure 3.3.11 Maximum Strain of Stoppers With Respect to Velocities for Channel 1

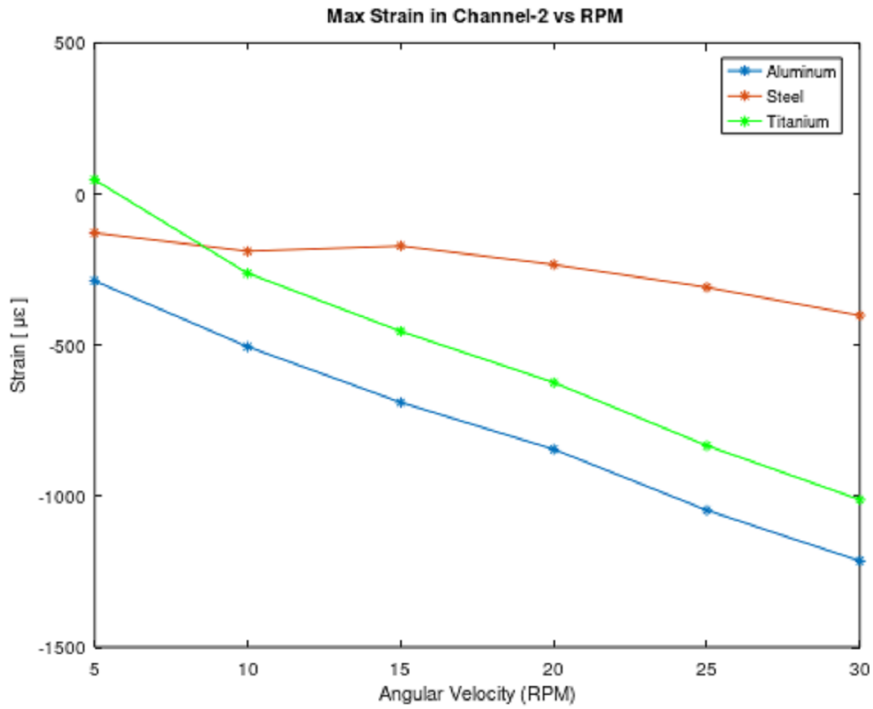

Figure 3.3.12 Maximum Strain of Stoppers With Respect to Velocities for Channel 2

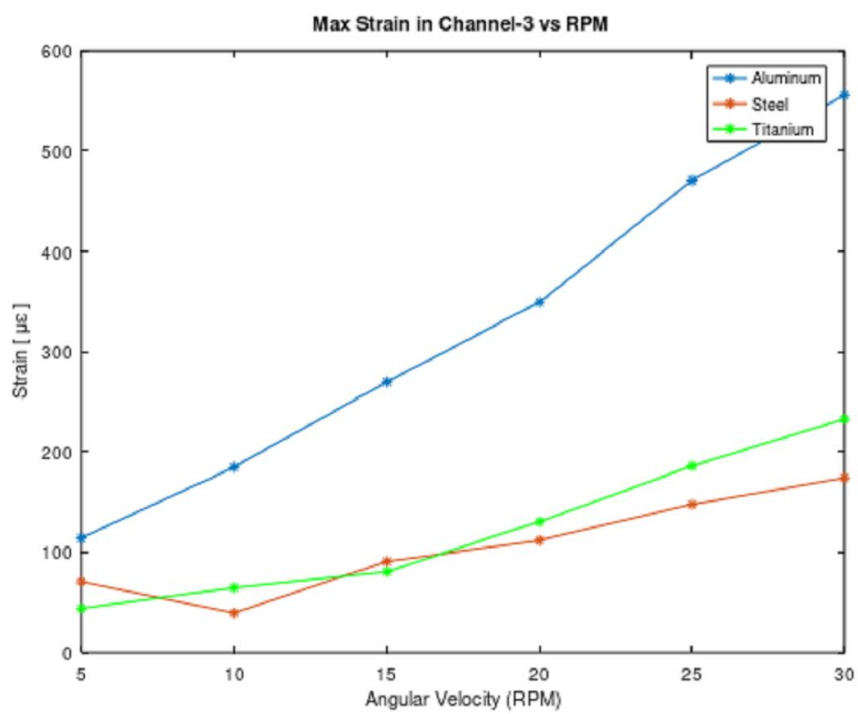

Figure 3.3.13 Maximum Strain of Stoppers With Respect to Velocities for Channel 3

4 COMPUTER AIDED ANALYSIS

In this chapter, it is aimed to understand the physics of the collision occurrence, express, and solve the phenomena with numerical analysis methods. To understand the impact phenomena, many analytical models are generated as we discussed in previous sections. However, it may be important and beneficial to investigate the occurrence with numerical analysis and compare the results. Thus, in this chapter, numerical solution study is carried on. Due to the high complexity of the whole system, numerical solution is carried on via computer aided numerical modelling program, ANSYS Mechanical 20R1. Since, the whole system is time dependent, "Explicit Dynamics" module of the program is used effectively. Many other studies, which focus on impact problems, uses and recommends "LS-DYNA" module, but, for this study and under these initial and boundary conditions, "Explicit Dynamics" is found to be useful and effective. During the modelling of the whole system, because of the complexity of the system and the impact physics, convergence is a dominant concern for such systems. Thus, to overcome convergence problem, such systems should be investigated carefully. Geometry preparation and initial and boundary condition selection plays key role. In this section, geometry preparation and analysis settings are explained in detail, and for this system and for similar systems, with different stopper materials, a generic ANSYS Mechanical model is created.

4.1 Geometry Analysis and Preparation

Antenna guidance body is a complex system. It is composed of structural mechanical bodies, bearings, shafts, electric motors, reducers, electronic components such as motor drives and encoders, cables connecting data and power, pipes carrying coolant liquids or gasses and slip rings if there is a requirement. It is impossible for one to represent the whole system in the FEM program with detail. Thus, there is an essential work needed to simplify the geometry and reduce the mesher and solver effort. First, all the cables and the pipers are ignored, due to their negligible contribution to the impact occurrence. Then, the electronic assemblies are removed from the system, because, most of them are very small and light components and, they are located in the arms that is not close to the impact area, which cannot have a major effect on the impact results. Thus, motor drivers, converters, filters etc. are removed from the

analysis body. Also, small details and features like pin holes, screw clearance holes, threaded holes, chamfers, radiuses etc. are removed because, these kind of details increases the node and element number significantly therefore increases the solver time severely.

Electromechanical components, such as electric motors and encoders are also discarded from the geometry, because, the initial motion to the system will be given as a joint initial condition. In addition, reducer is discarded from the analysis geometry due to its complicated geometry. The main parameters, which may affect the results of the analyses, are inertia and friction of the motor and reducer. Inertia parameter is negligible compared to payload, thus, neglecting these components may not affect the result significantly. Friction parameter is balanced via speed control of test procedure, thus, friction torque of the whole system may not affect the system significantly. Friction parameter will be discussed in the results section of this study in detail.

In addition, friction parameter is affected by rotary joint component of the system, however, as explained above, friction of the whole system is balanced and reduced with the speed control of the real time test, thus, rotary joint is discarded from the analysis model.

After the simplification process is carried on, a primitive analysis model is created and checked whether the geometry is sufficient or not. After this point, the geometry detail is increased via performing trial error method on “Explicit Dynamics” module with consistent and correct boundary and initial conditions. First primitive model can be seen in Figure *4.1.1*.

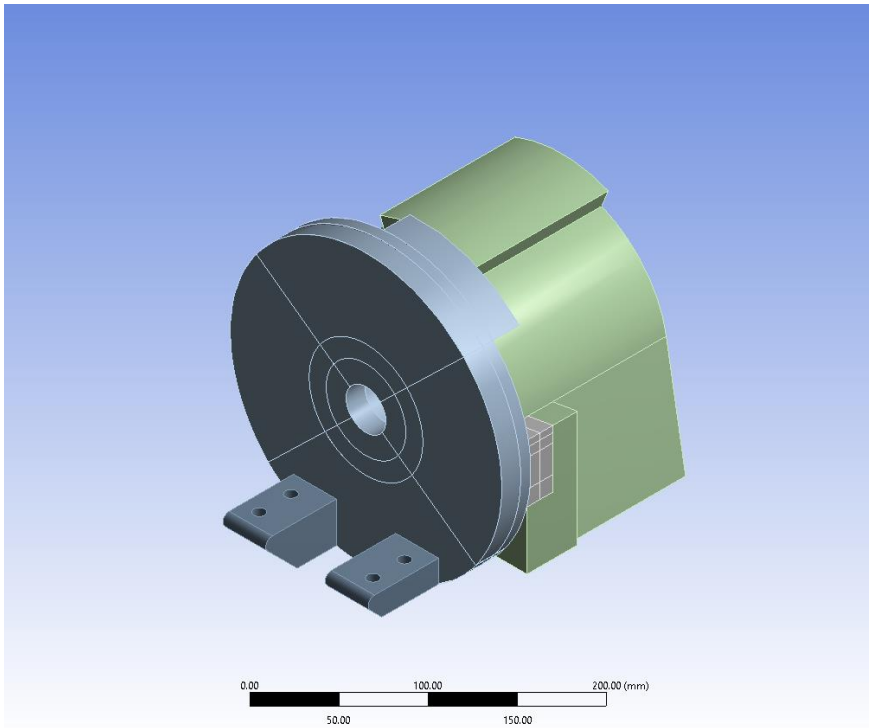

Figure 4.1.1 Primitive Simplified Geometry Assembly

After checking the results, it has been seen that, impact results are not representing the expected behavior the geometry is updated. After these iterative operations, adequate geometry of the system is created as seen is the Figure *4.1.2*. This model is used for the FEM analysis of the impact occurrence for each material case.

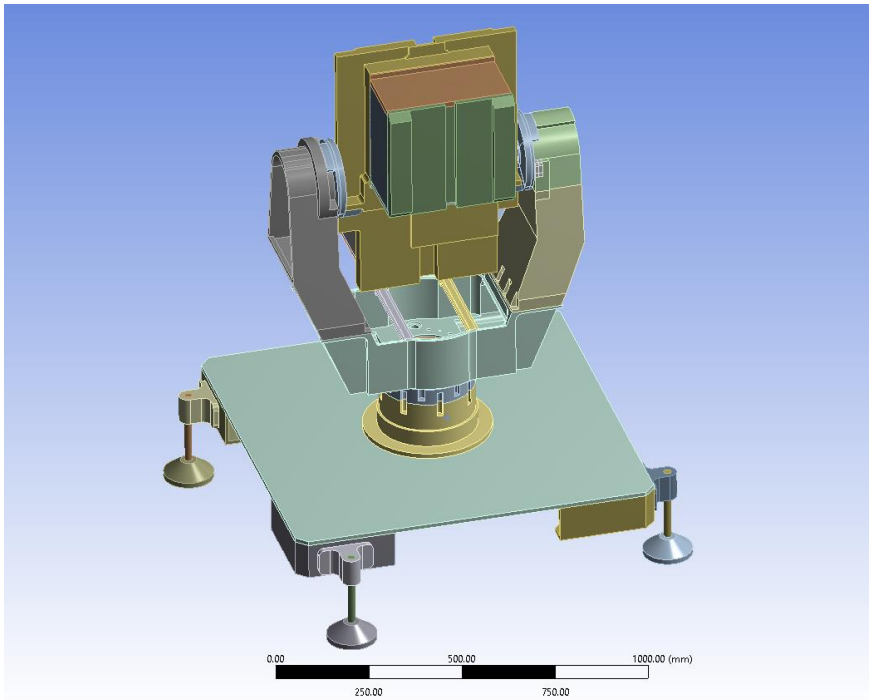

Figure 4.1.2 Final Analysis Geometry Assembly

The comparison between the analysis models generated on the real time test model can be seen in the Figure *4.1.3*.

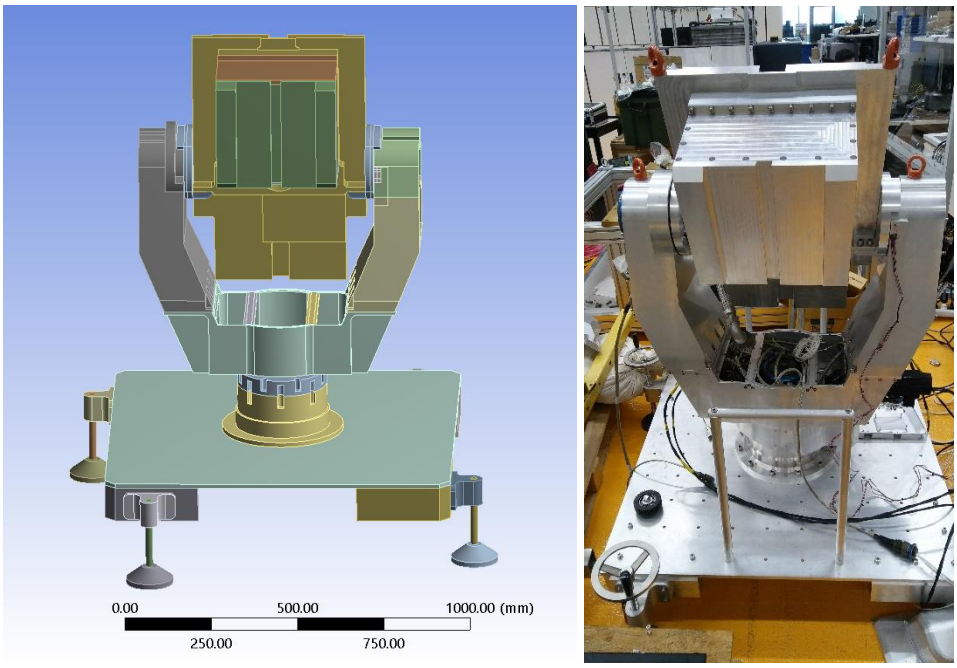

Figure 4.1.3 Analysis Geometry and Test Part Comparison

4.2 ANSYS Mechanical Model

After simplification and reduction of the geometry, the analysis body is transferred into the ANSYS Mechanical environment. At this stage of the study, material assignments, boundary and initial conditions are set. To obtain an accurate and precise result with respect to test results, one must investigate and understands the test boundary and initial conditions carefully.

During the test, as describe in the previous sections, the payload is accelerated with a known torque up to the desired rotational velocities to collide payload to the stopper. After reaching the desired velocity for each test sequence and condition, the controller has given some amount of torque to the payload to prevent the deceleration due to the frictional torque. Friction torque of the system with reducer, motor and rotary joint is concluded as 21 Nm from the Torque-Time diagram of the controller. During the impact, data is collected via data acquisition system and results are given as Strain-Time graphs in the previous sections.

As mentioned above, the test conditions should be reflected to the analysis set-up. After the solid bodies are imported to the mechanical interface, material of the sub parts of the assembly are assigned. Analysis materials mechanical properties are adapted from literature and given in the Table *4.2.1*.

Table 4.2.1 Materials and Mechanical Properties

Property	**Unit**	**AL 6061-T651**	**AISI 304**	**TI-6AL-4V**
Density	kg/m^3	2698.8	8000	4430
Thermal Expansion Coefficient	C^{-1}	2.30E-05	1.20E-05	8.60E-06
Young's Modulus	GPa	68.95	200	113.8
Poisson's Ratio	-	0.33	0.28	0.34
Bulk Modulus	GPa	67.6	151.5	120
Shear Modulus	GPa	25.9	78.1	42.4

Assembly sub parts material assignments can be seen in the Table *4.2.2*. For stopper geometries, for each case of impact analysis, AISI 304, 6061-T651 and TI-6AL-4V materials are assigned individually.

Table 4.2.2 Material Assignment Table

No	Assembly Part	Assembly Sub Part	Material
1	Dummy Payload		AL 6061-T651
2	Payload Carrier		AL 6061-T651
3	Chassis		-
4		Chassis	AL 6061-T651
5		Chassis Lat. Sup.	AL 6061-T651
6		Arm	AL 6061-T651
7		Arm Col	AL 6061-T651
8		Azimuth Shaft	AL 6061-T651
9		Fixed Body	AL 6061-T651
10	Carrier Table		-
11		Carrier Table	AL 6061-T651
12		Carrier Leg	AISI 304
13		Carrier Leg Sup.	AL 6061-T651
14		Carrier Table Found.	AL 6061-T651
15		Carrier Leg Ground	AL 6061-T651
16	Stopper		**
17	Upper M5 Screw		AISI 304
18	Bottom M5 Screw		AISI 304
19	Top Bearing Rep		AISI 304
20	Bottom Bearing Rep		AISI 304

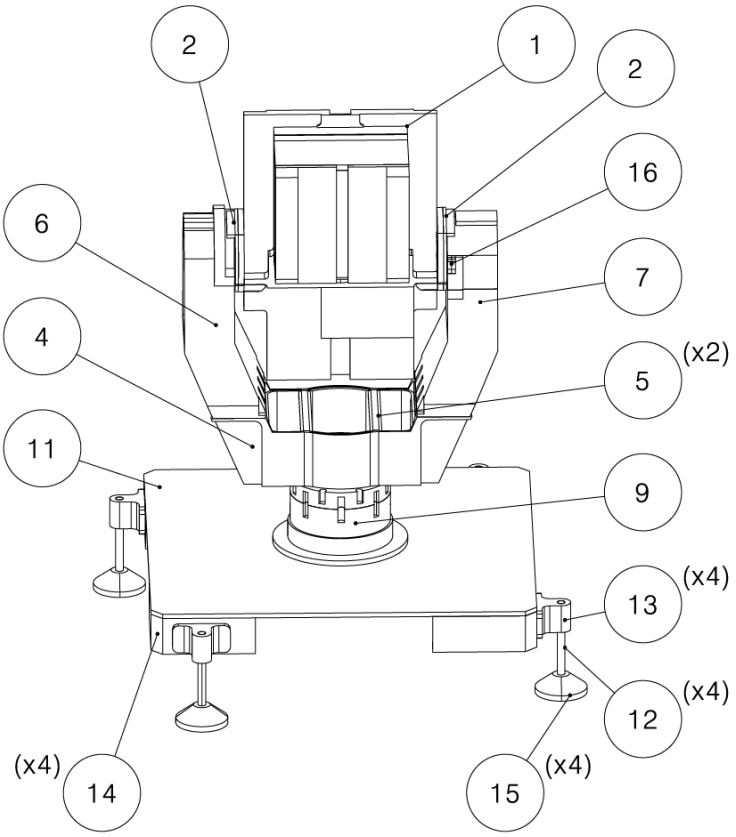

Figure 4.2.1 Schematic Representation of Test Assembly

Parts are modelled in modelling software, SpaceClaim and Siemens NX, and grouped with respect to their task in the structure tree of the assembly. Chassis parts are the structural members, which carries the payload, electronics and drive elements. These parts are manufactured from aluminum alloy due to its high strength with low-density advantage. Carrier table is an assembly to transfer and ground the whole assembly during tests and re-work, assemble, re-assemble processes. Parts described in above table can be seen in Figure *4.2.1*.

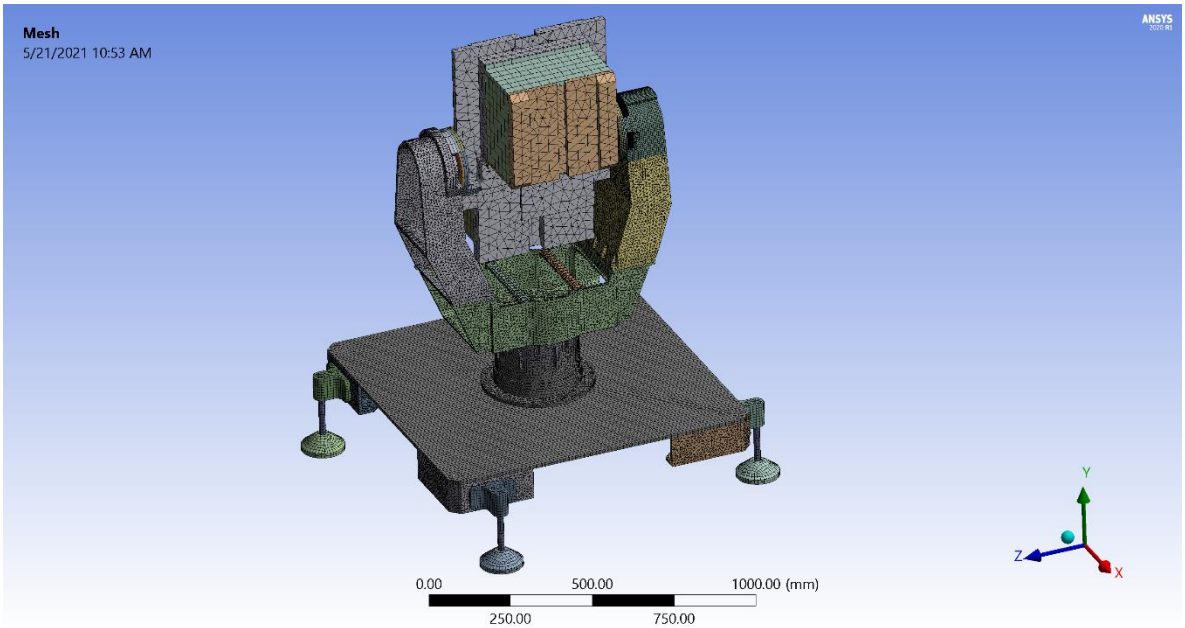

Figure 4.2.2 Generated Mesh on Bodies

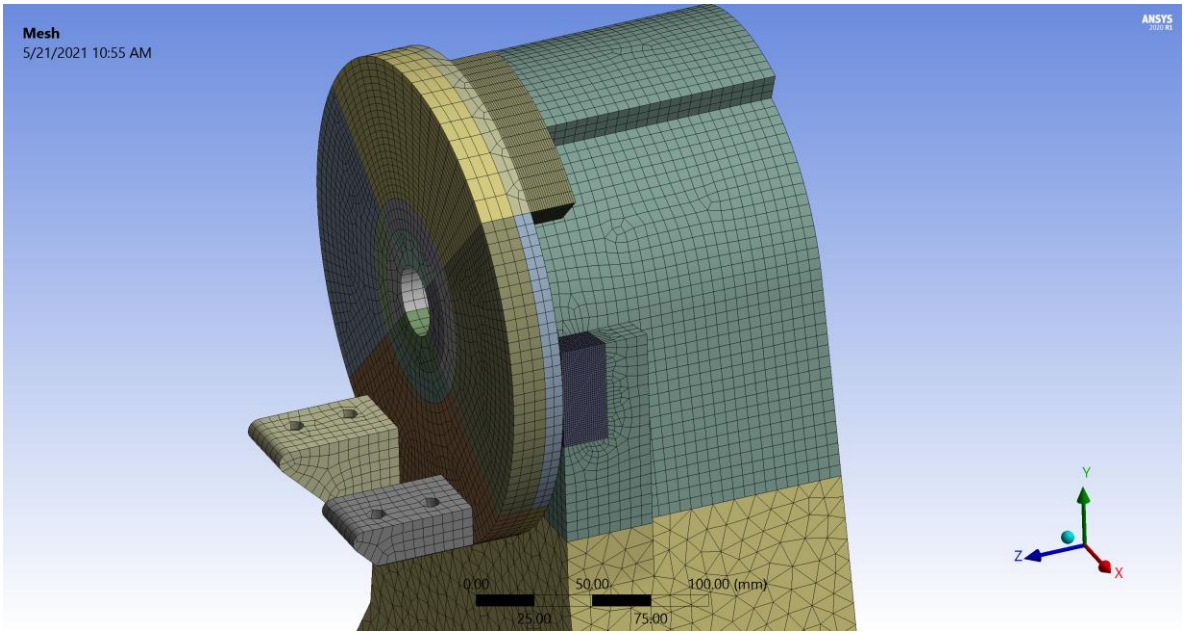

Figure 4.2.3 Generated Mesh on Stopper and Collision Arm

Some bulk parts are divided into small parts and bonded in the mechanical interface to increase the mesher ability and performance. To increase the mesher performance, reduce node and element number and optimize the mesh density, parts are divided into basic shapes like tetragonal prisms and disc slices. This process gives mechanical to use “Sweep” method

and “Hex. Dominant Method” for such parts to reduce mesh density and increase mesher performance. All elements are set to be quadratic elements to allow non-linear behavior of stress strain results. To increase local mesh density and decrease mesh sizing, size functions are used. For example, to investigate the stress-strain behavior on “Stopper” part, 1 mm mesh sizing function is applied. Mesh options and mesh statistics are given in Table *4.2.3*. In addition, mesh of the whole assembly and location where impact occurs are given in Figure *4.2.2* and Figure *4.2.3*.

Table 4.2.3 Mesh Options and Statistics

Physics Preference	Mechanical
Solver Preference	Mechanical APDL
Element Order	Quadratic
Error Limits	Aggressive Mechanical
Nodes	767,920
Elements	302,777

For the mating parts in the assembly, bonded type connection is used. This reduces number of parts modelled in mechanical environment, reduces mesh number, increases solver performance and convergence. Colliding interface is modelled as “Frictional Contact” with friction coefficient of 0.5, trim tolerance of 4.4 mm and pinball radius of 3.2 mm. For stopper and collision arm interface, “Frictional Contact” type is used with friction coefficient of 0.5. Moving parts are modelled as “Revolute Joint” for each payload carrier part.

Assembly is fixed from the “Carrier Leg Ground” parts. Firstly, rotary motion is given to the revolute joints mentioned above. But, giving the motion to both joints causes for the ANSYS mechanical a convergence problem, thus the motion is supplied to the assembly via one revolute joint where non-colliding arm carrier part is located. For initial position, in polar coordinates with respect to the revolute joint on the colliding arm, two stopper parts are approximately 0.6 radians distant from each other. This makes carrier arm to have 0.6 radians to travel before colliding with the stationary stopper parts. After calculating the travel distance, rotational velocity profile is obtained. Due to the convergence concerns, rotational

acceleration is kept smaller. Rotational velocity profile is given in Figure 4.2.4 and Table *4.2.4*.

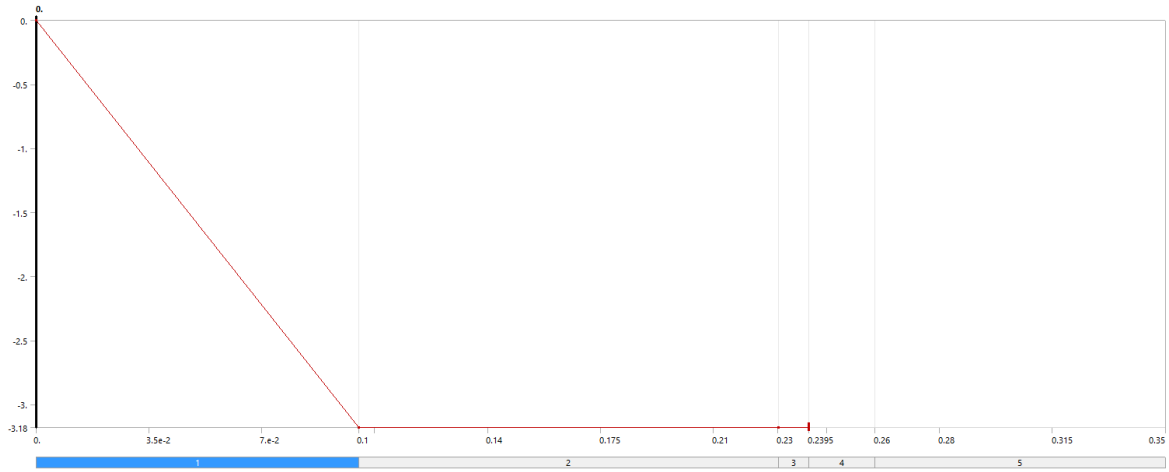

Figure 4.2.4 Rotational Velocity Profile

Table 4.2.4 Rotational Velocity Profile

Time (sec)	**Rotational Velocity (Rad/s)**
0	0
0.1	-3.18
0.23	-3.18
0.2395	-3.18
0.26	-3.18
0.35	-3.18

After checking the first solver attempts, it has been seen that, after reaching the desired rotational velocity of 3.14 rad/s, due to the stiffness and inertial effects of payload, payload generates waves that shakes the whole assembly. This shaking motion of the whole assembly causes reduction in payloads rotational velocity. To compensate this reduction in velocity, initial velocity of the payload is increased to 3.18 rad/s in scalar manner. The (-) sign is to ensure the direction of the rotational motion, due to the revolute joints sign convention.

Since the impact phenomena is a non-linear occurrence, the analysis should comprise non-linear effects of materials and change in the stiffness coefficient of the bodies. Thus, “Large Deflection” option is enabled for explicit solution. In addition, large deflection option helps

solver to rotate the motion body. Disabling large deflection may prevent the motion of the payload and result in “Maximum allowable deformation is exceeded” error. The solution time is divided into 5 sub steps and each sub step is solved by time integration. For the first sub step, payload is accelerated slowly. This one is divided into 0.02-second time intervals and ended at 0.1 second. In the second sub step, payload reached the desired rotational velocity of 3.18 rad /s, integrated with minimum time step of 0.01 seconds, and lasted for 0.13 second. At the third sub step, two stoppers get close to each other, thus, to ensure that frictional support between the stopper faces to be activated and improve the convergence ability of the solver, time integration is lowered to 0.0025 seconds and lasted until 0.2395 seconds of the motion. At the end of the third sub step, rotational velocity input is deactivated to prevent any extra load on the impacting stoppers. At the fourth sub step, free impact occurrence is observed with the same time integration interval with third sub step until 0.28 seconds of the motion. Until the end of this sub step, impact, indentation, peak point and restitution is observed. For the last sub step, bounce of the payload from stopper is observed until 0.35 second of the motion. Sub step control can be seen in Table *4.2.5*.

Table 4.2.5 Sub Step Control of Explicit Dynamics

Sub Step Number	Step End Time	Initial Time Step	Minimum Time Step	Maximum Time Step
1	0.1	0.02	0.02	0.02
2	0.23	0.02	0.01	0.02
3	0.2395	0.0025	0.0025	0.0025
4	0.28	0.0025	0.0025	0.0025
5	0.35	0.02	0.02	0.02

4.3 FEM Results

Initial and boundary conditions obtained from real time test are applied to the mechanical model in 3 different cases, for aluminum AL-6061-T651 alloy, stainless steel AISI 304 alloy and titanium Ti-6Al-4V alloy stationary stopper materials. For each material, many numerical simulation iterations are conducted. Numerical solutions are carried on such for 30 RPM, 3.14 rad/s rotational velocity for each case to compare the results with each other and to compare with test and analytical solutions. At the end of numerical solution process, adequate solutions have been obtained. Before analyzing the results of the numerical

solutions, an important remark should be pointed out about test and numerical solution of the impact problem. As seen in Figure *4.3.1*, test results shows a main peak for strain values for each material and each velocity test. However, at the beginning and at the end of the main peak, small peaks compared to main peak show up. On the contrary, initial FEM analysis of the system had given any such peaks on the geometry taken from design software NX. Initial FEM analysis results have given simple peaks with no distortion at the beginning or at the end of the impact. After analyzing the situation and carrying on many numerical solutions on the geometry, it has been seen that, any flatness failure, or any angularity failure of the contacting faces of two colliding parts creates these extra small peaks at the beginning and at the end of impact. Since these parts are machined in CNC milling tables, which have comprehensible tolerance margin to cause this kind of production faults. Also during assembling process of the stoppers to the colliding arm, workmanship may cause these angularity and flatness error. Thus, for each stopper material case, the angularity of the colliding surface is falsified under control. Many studies and numerical analyses have been conducted to find the admissible amount of angularity error. Therefore, as seen in the Figure *4.3.2* and Figure *4.3.3*, the surfaces of the stationary stoppers have been deflected within the margin of manufacturing tolerance of 0.2.

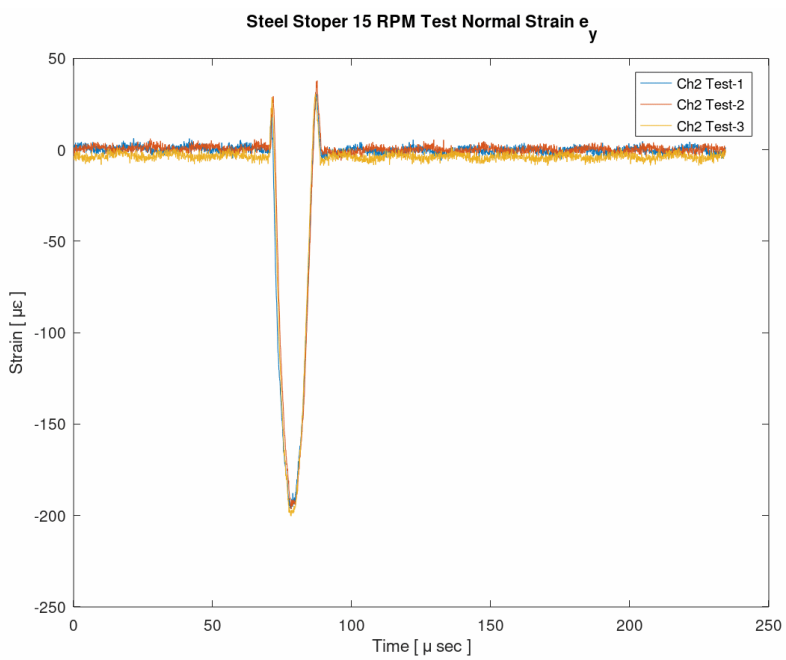

Figure 4.3.1 Small Peaks Before and After the Main Peak of Impact Strain

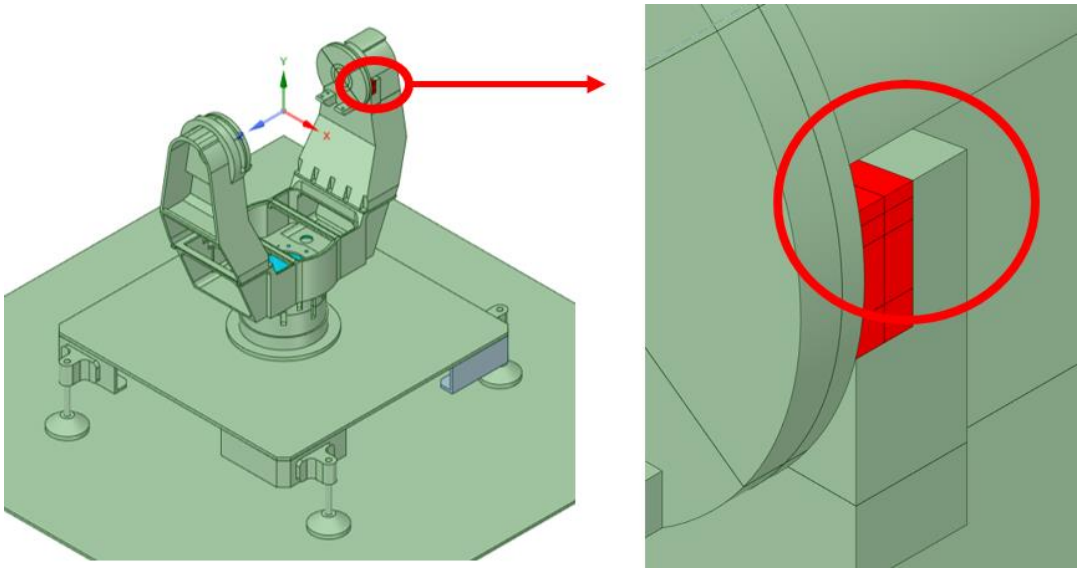

Figure 4.3.2 Stationary Stopper Impact Surface

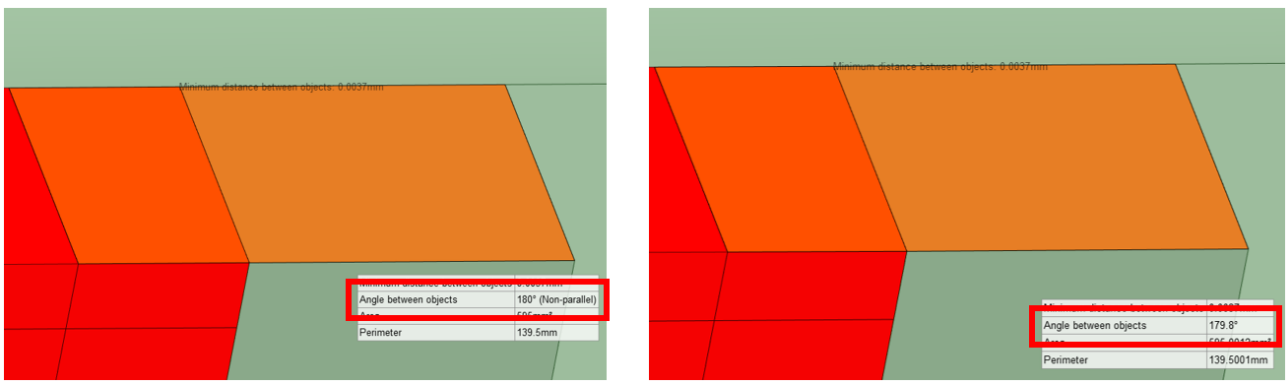

Figure 4.3.3 Deflected Stationary Stopper Surface

This geometrical deflection is implemented to geometries of numerical solution for all different material cases.

Numerical analysis results have given adequate results when compared to test results. The comparison between test result and numerical solution results will be given in the next chapter of this study in detail. An important point of the results of 30-RPM numerical solutions for all three different materials, for the local area where the strain gauges implemented are not in plastic deformation zone, as seen in Figure *4.3.4*, Figure *4.3.5* and Figure *4.3.6*. For such impact cases, especially for the regions close to the impact interface

or the colliding piece is structurally weak, plastic deformations may be inevitable. For strain gauge readings, plastic deformations are very dangerous errors, which throw away all the study and effort.

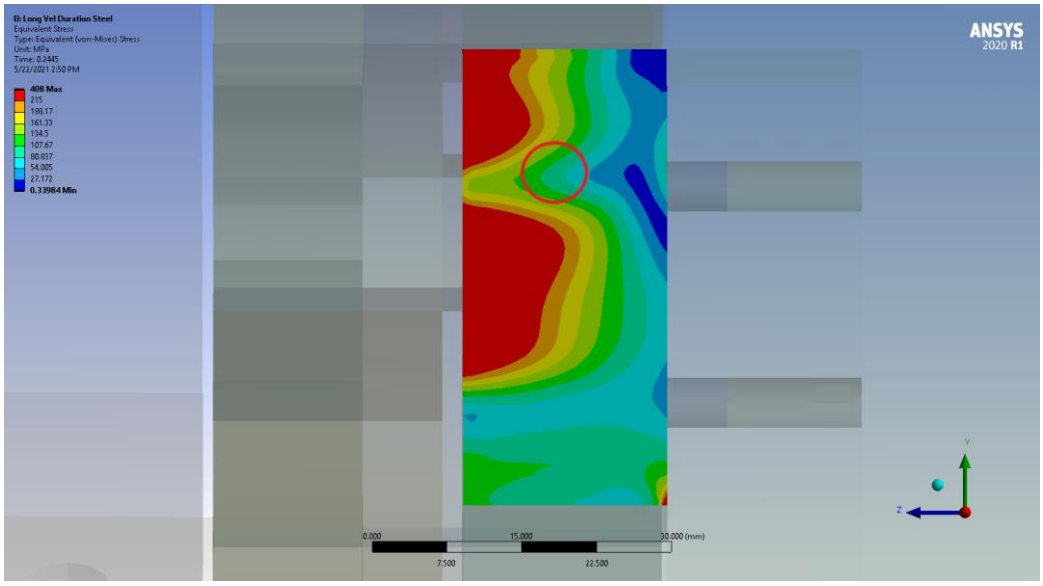

Figure 4.3.4 Von-Misses Stress Generated on Steel Stopper Specimen Strain Gauge Surface

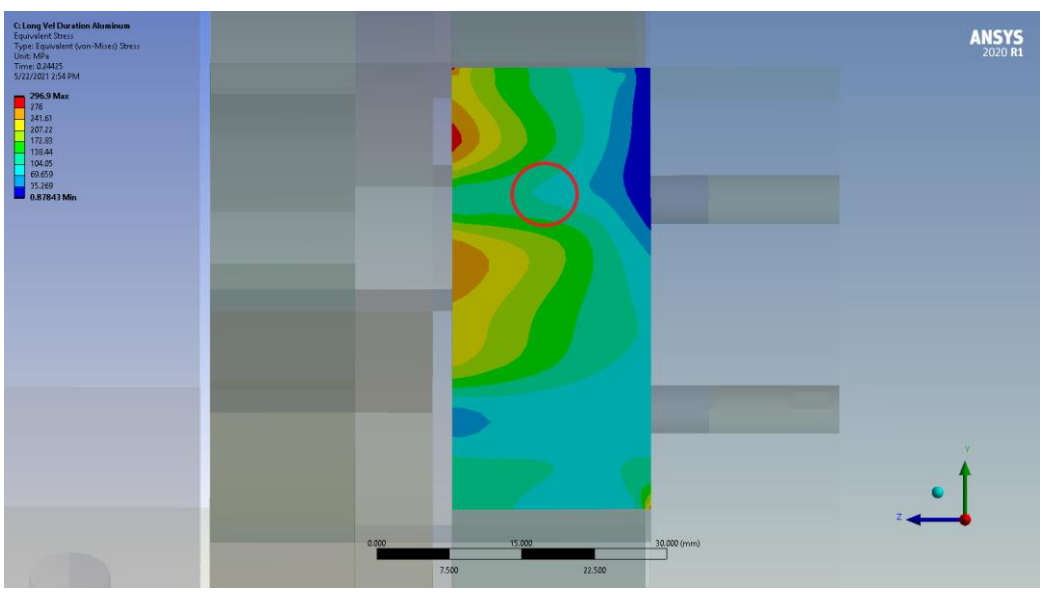

Figure 4.3.5 Von-Misses Stress Generated on Aluminum Stopper Specimen Strain Gauge Surface

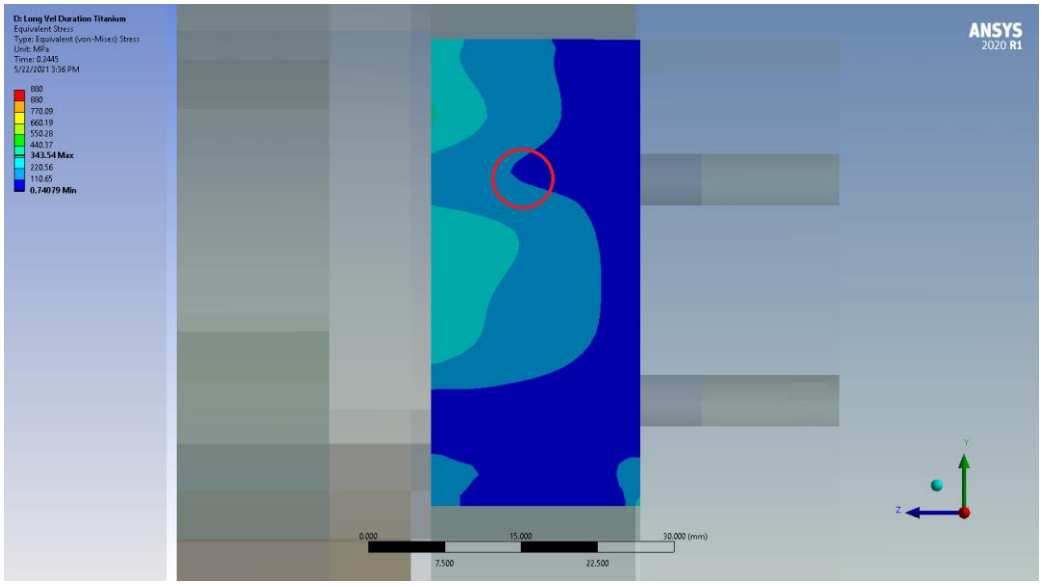

Figure 4.3.6 Von-Misses Stress Generated on Titanium Stopper Specimen Strain Gauge Surface

The results of numerical solution are shown below, from Figure *4.3.7* to Figure *4.3.12*, in addition, strain contours can be seen in figures below, from Figure *4.3.13* to Figure *4.3.18*.

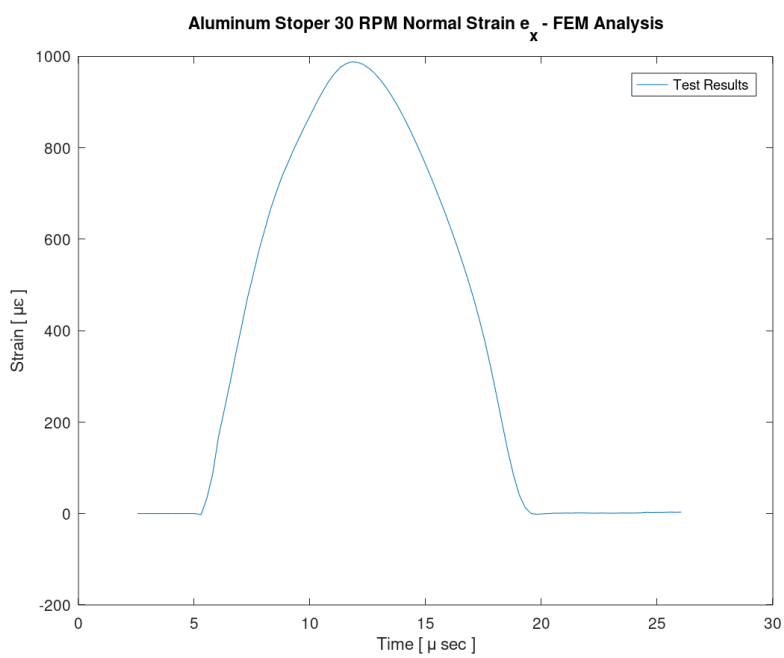

Figure 4.3.7 Normal Strain in (X) Direction for Aluminum Stopper

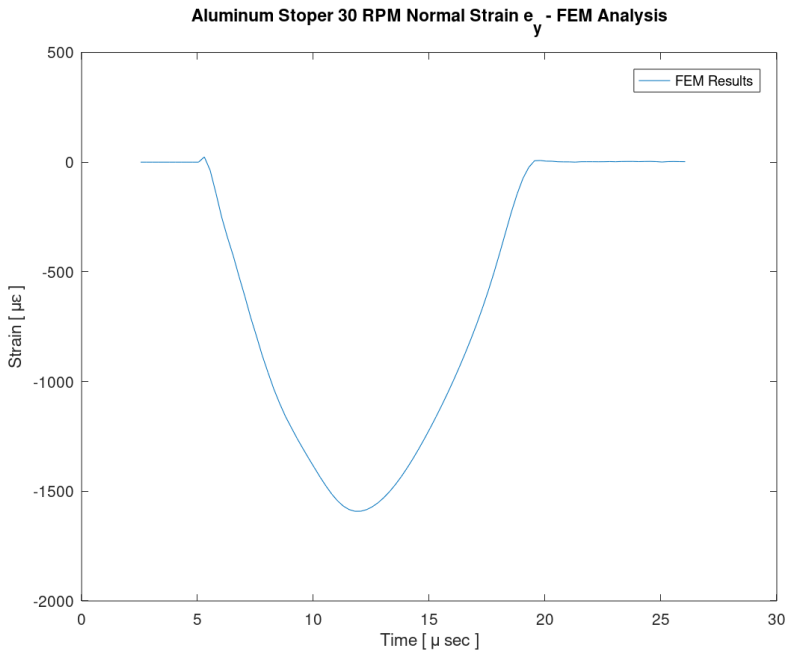

Figure 4.3.8 Normal Strain in (Y) Direction for Aluminum Stopper

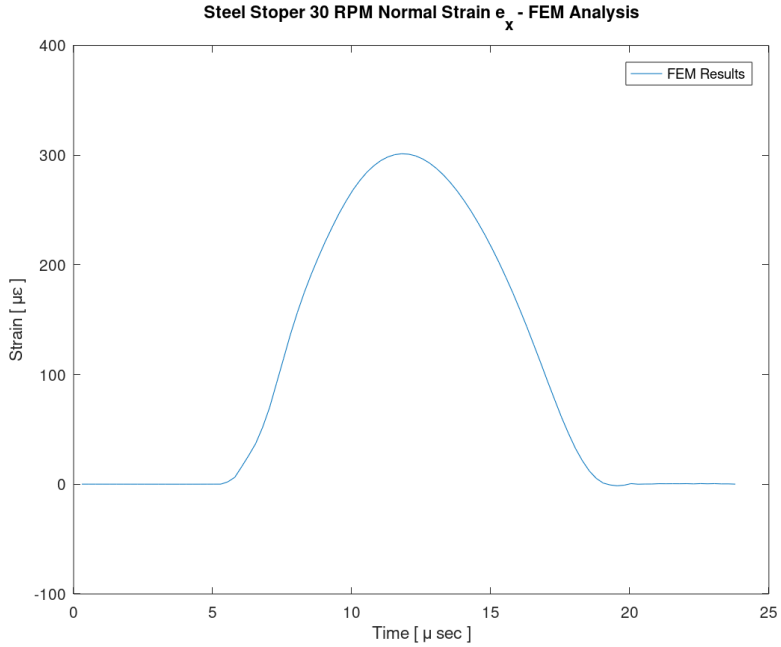

Figure 4.3.9 Normal Strain in (X) Direction for Steel Stopper

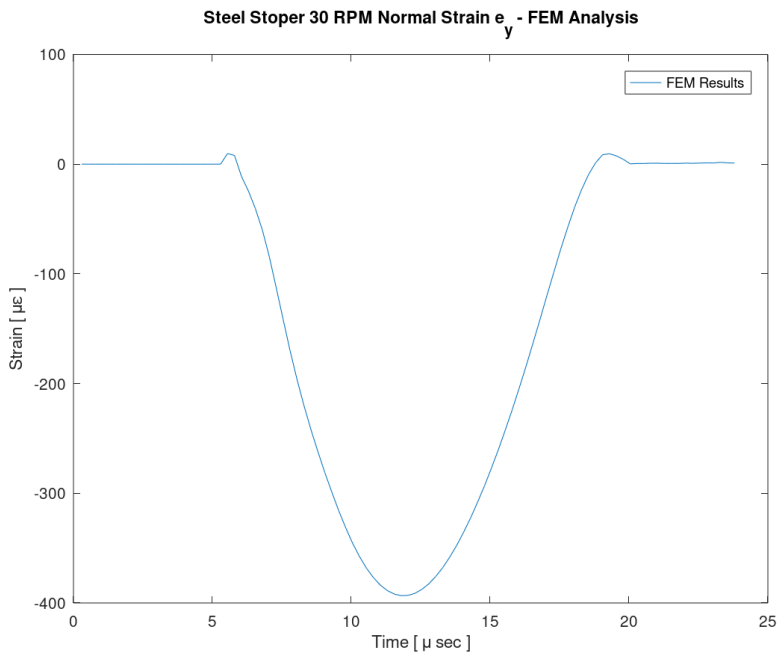

Figure 4.3.10 Normal Strain in (Y) Direction for Steel Stopper

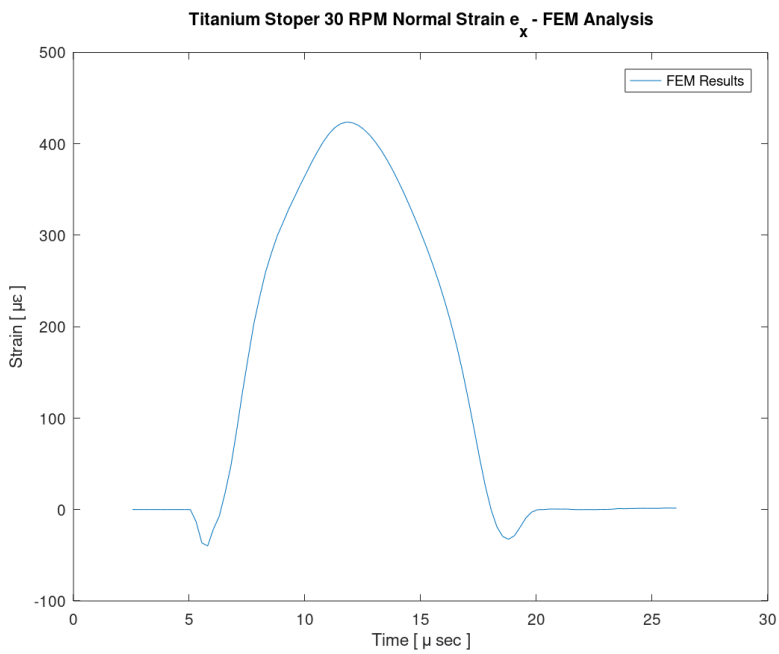

Figure 4.3.11 Normal Strain in (X) Direction for Titanium Stopper

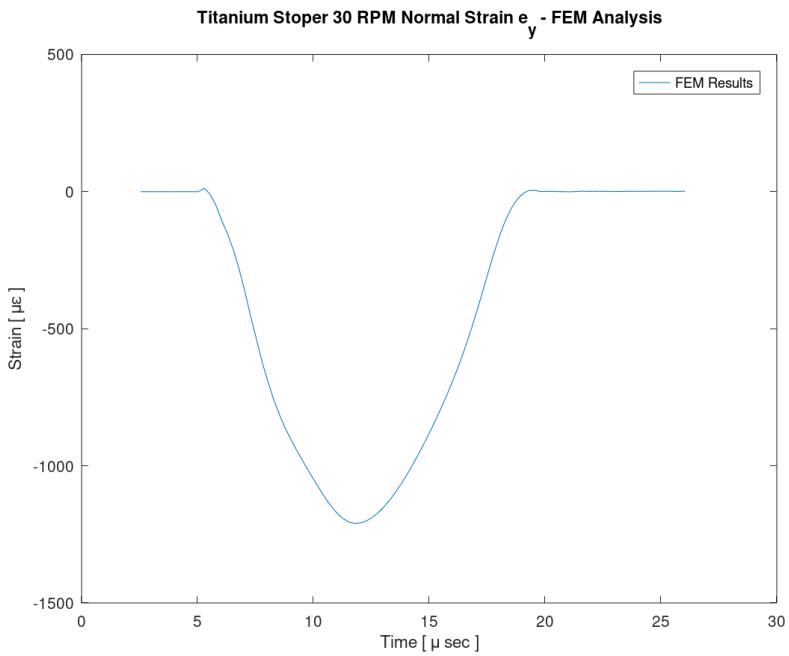

Figure 4.3.12 Normal Strain in (Y) Direction for Titanium Stopper

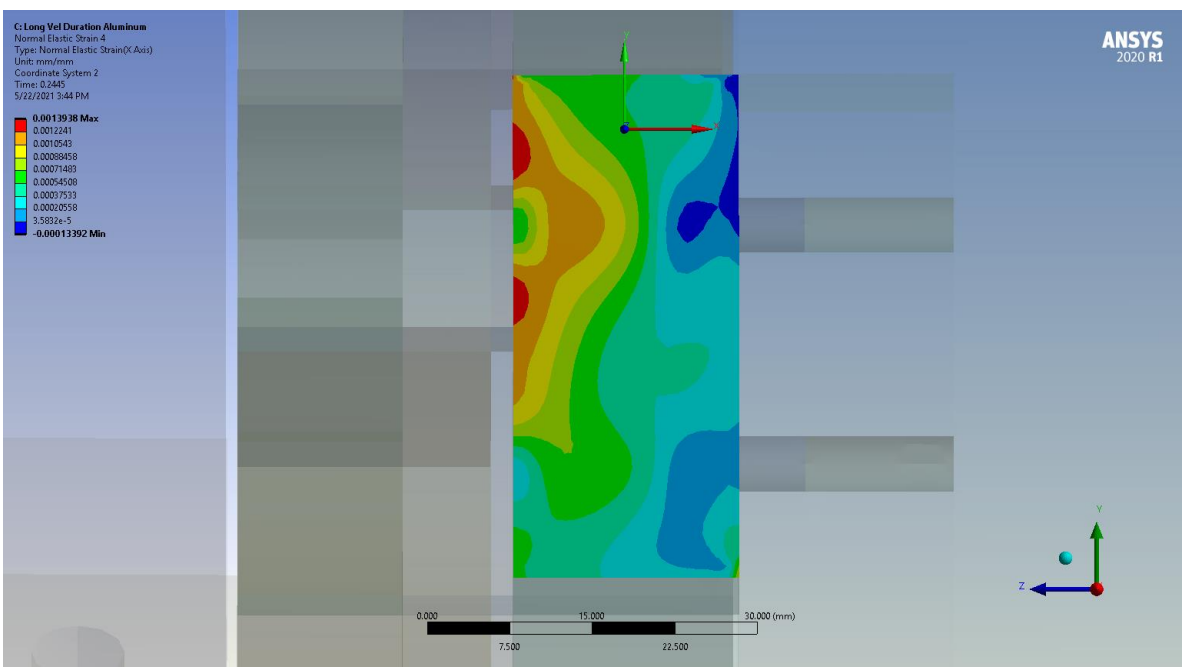

Figure 4.3.13 Normal Strain Contour in (X) Direction for Aluminum Stopper

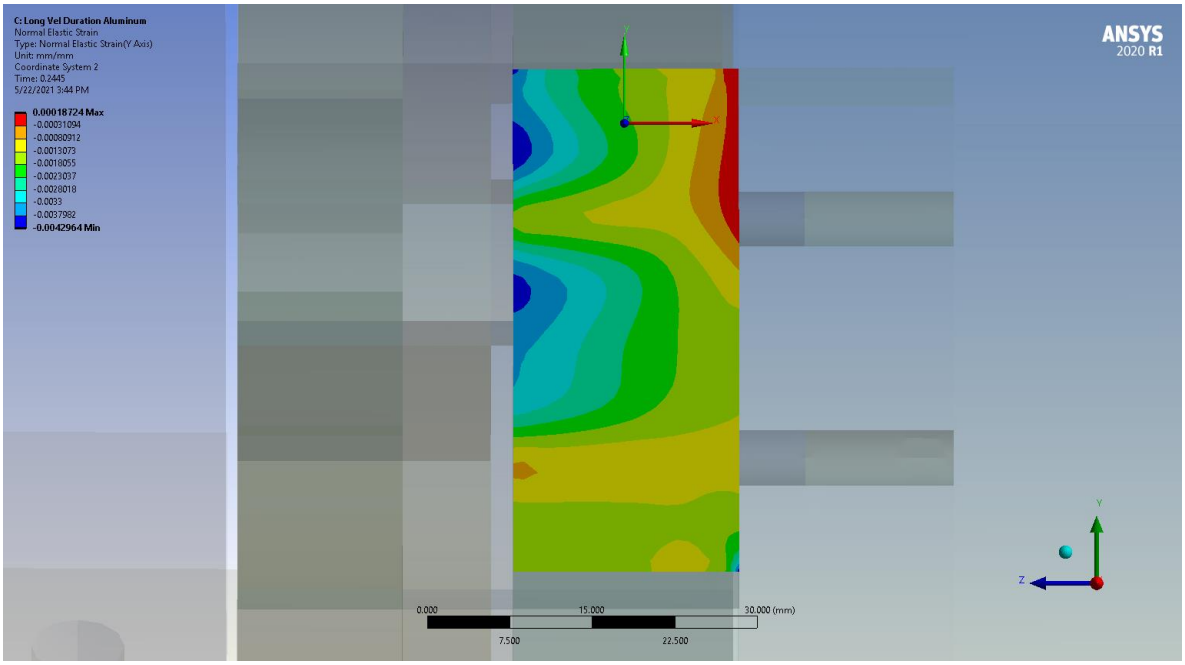

Figure 4.3.14 Normal Strain Contour in (Y) Direction for Aluminum Stopper

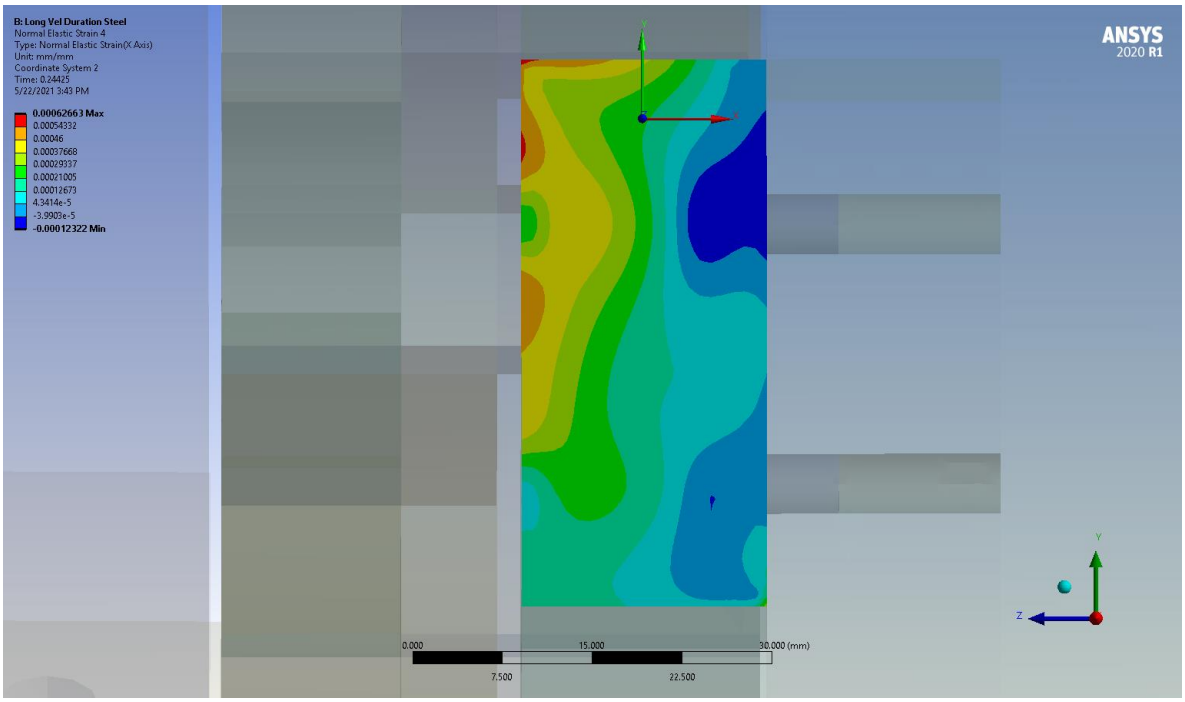

Figure 4.3.15 Normal Strain Contour in (X) Direction for Steel Stopper

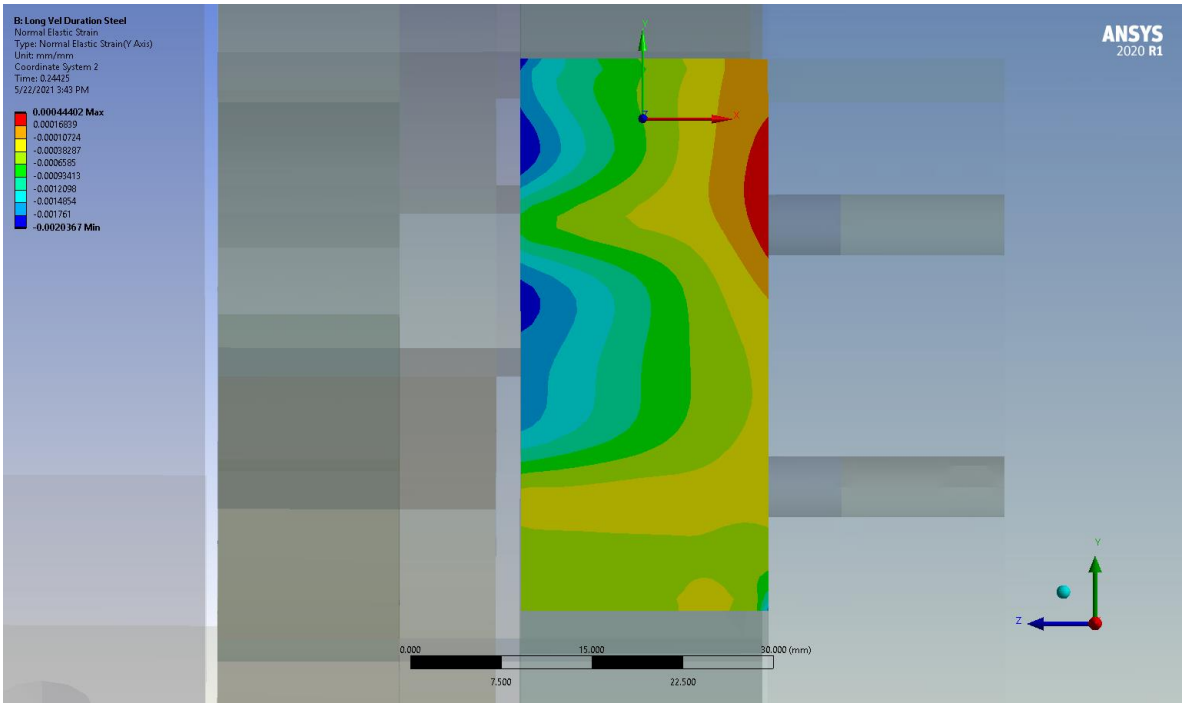

Figure 4.3.16 Normal Strain Contour in (Y) Direction for Steel Stopper

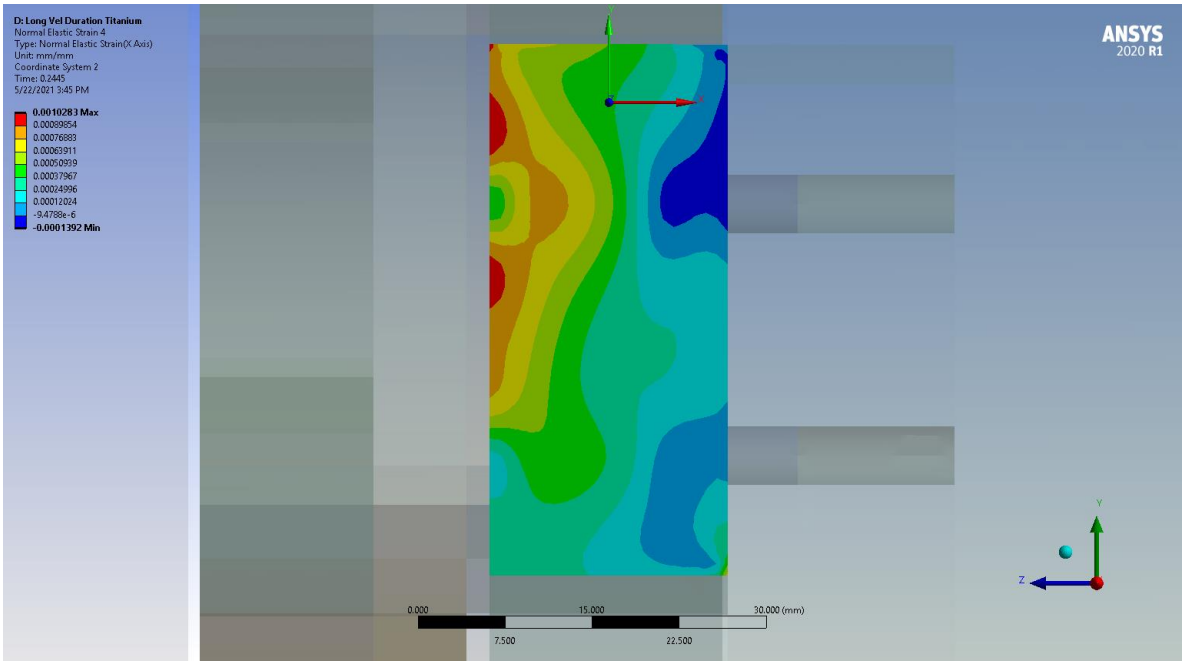

Figure 4.3.17 Normal Strain Contour in (X) Direction for Titanium Stopper

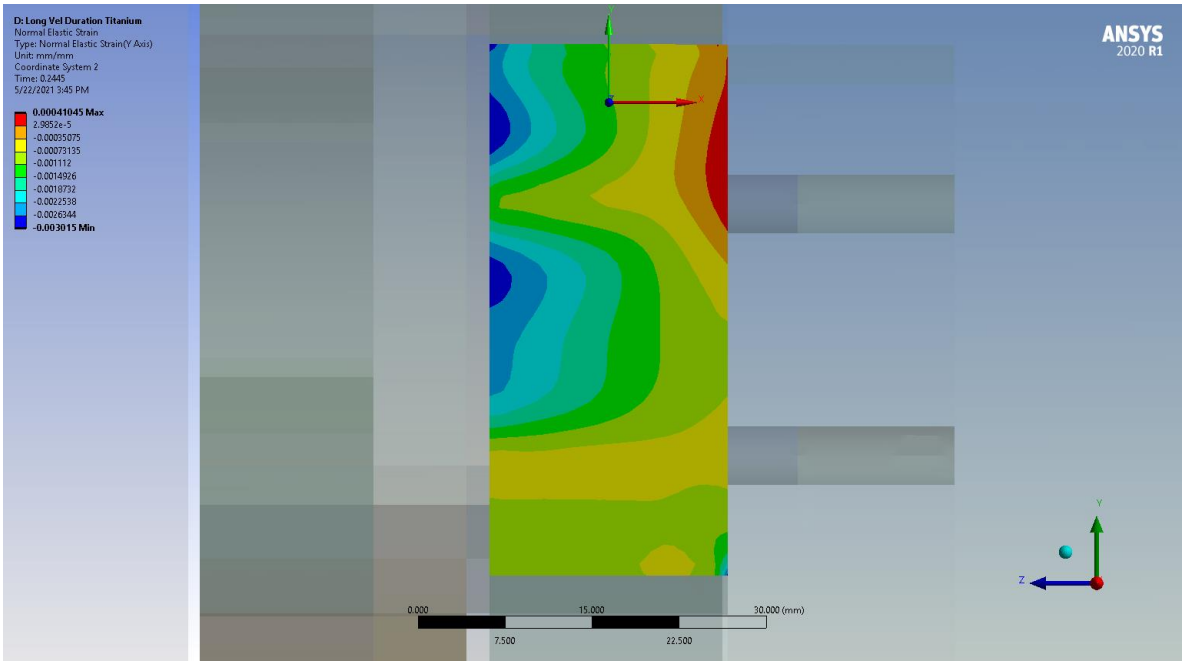

Figure 4.3.18 Normal Strain Contour in (Y) Direction for Titanium Stopper

For each numerical solution for different materials, the peak strain values occurred within the strain gauge zone, peak time of impact and impact duration are given in Table *4.3.1*.

Table 4.3.1 Strain Value, Peak Time and Impact Duration

Stopper Material	**AL 6061-T651**	**AISI 304**	**TI-6AL-4V**
Normal Strain At Peak in X Direction	423.85	296.25	987.22
Normal Strain At Peak in Y Direction	-1209.8	-404.25	-1590.9
Peak Time (sec)	0.24425	0.24425	0.2445
Impact Duration (msec)	15.5	15.25	14.75

5 COMPARISON OF TESTS, ANALYSES AND MATHEMATICAL MODELS

5.1 Test and FEM Analysis Comparison

Real time impact test is conducted for 5 to 30 RPM of rotational velocities of payload with 5-RPM increments and recorded as mentioned in above Section 3.3. FEM analysis method and results are also mentioned in Section 4.3. These results can be said to be close enough to compare the results. FEM effort of this study is carried on and represented in detail to show and use the method for numerous cases especially for such systems has rotational motion and mechanical stoppers. The comparison of test and FEM results in normal X, Y and Z directions with respect to stopper body are given in below figures, from Figure *5.1.1* to Figure *5.1.6*.

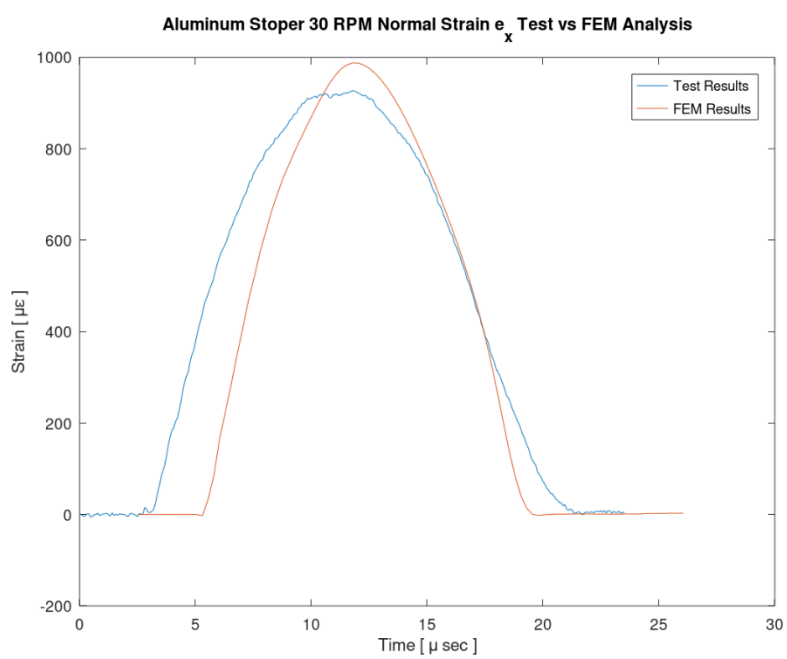

Figure 5.1.1 Aluminum Stopper Comparison of Test and FEM Normal Strain Results in (X) Direction

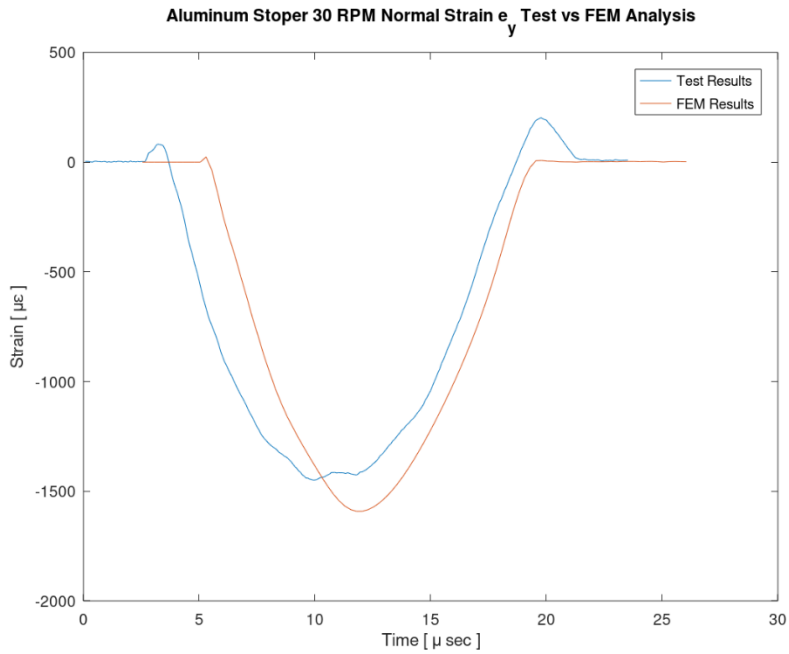

Figure 5.1.2 Aluminum Stopper Comparison of Test and FEM Normal Strain Results in (Y) Direction

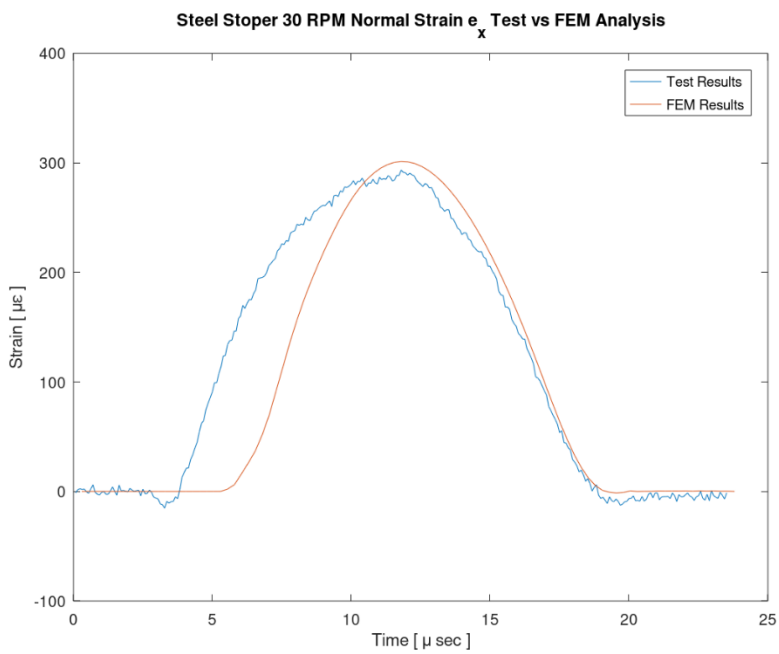

Figure 5.1.3 Steel Stopper Comparison of Test and FEM Normal Strain Results in (X) Direction

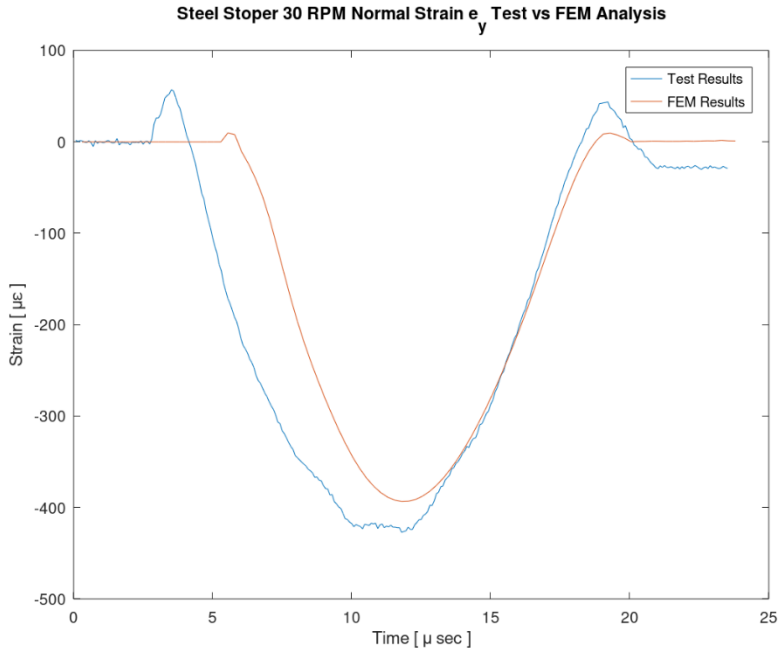

Figure 5.1.4 Steel Stopper Comparison of Test and FEM Normal Strain Results in (Y) Direction

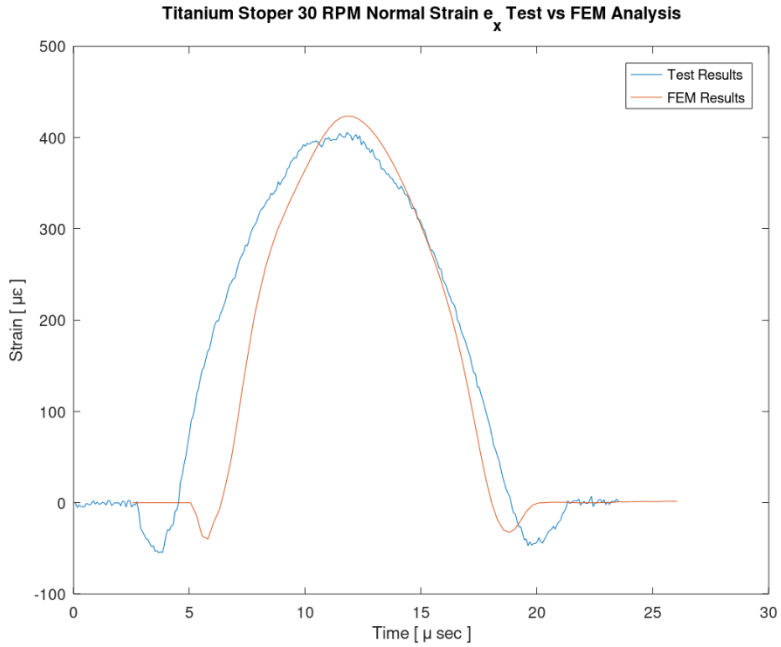

Figure 5.1.5 Titanium Stopper Comparison of Test and FEM Normal Strain Results in (X) Direction

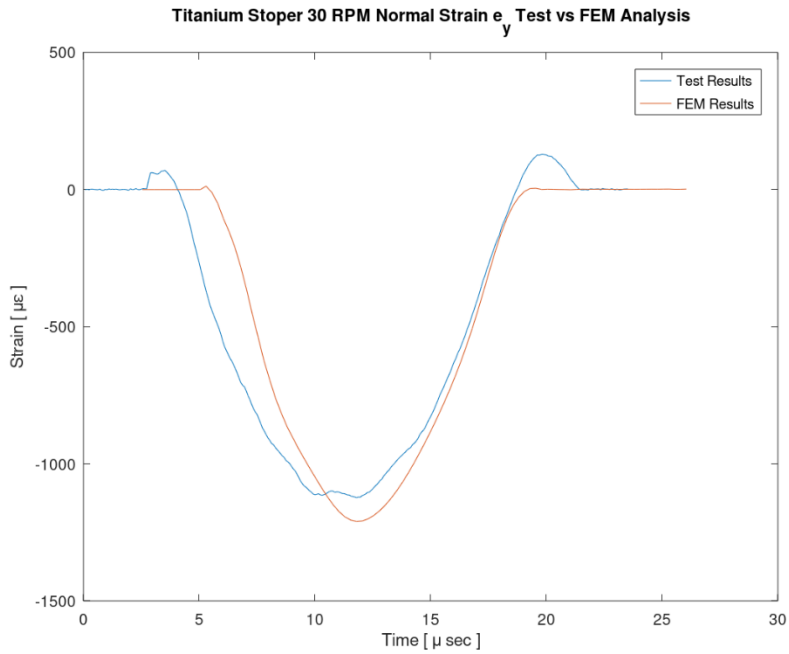

Figure 5.1.6 Titanium Stopper Comparison of Test and FEM Normal Strain Results in (Y) Direction

As seen in the figure above, the results of real time test and the FEM solutions are adequate and comparable. Thus, it can be said for FEM settings to be applicable and consistent for analyzing such systems. For each case, normal strain peaks for each material taken from FEM analysis are consistent with test results. Moreover, the small peaks emerged in the test result just before and after impact can be seen in the FEM results as mentioned in previous sections. Thus, the results explain these small peaks clearly.

Since tests are conducted in physical environment and FEM results are output of a software, the peak values differ from each other within an acceptable limit of error. The results comparison and error limits are given in Table *5.1.1*, Table *5.1.2* and Table *5.1.3* for each stopper material of AL6061-T651, AISI 304 and TI-6AL-4V respectively.

Table 5.1.1 Test and FEM Results Comparison for Aluminum Stopper

	ε_x	ε_y
Test Results	933	-1457.8
FEM Results	987.22	-1590.9
Error	5.492%	8.366%

Table 5.1.2 Test and FEM Results Comparison for Steel Stopper

	ε_x	ε_y
Test Results	301.5	-419
FEM Results	296.25	-404.25
Error	1.772%	3.649%

Table 5.1.3 Test and FEM Results Comparison for Titanium Stopper

	ε_x	ε_y
Test Results	408	-1128
FEM Results	423.85	-1209.8
Error	3.740%	6.761%

Since the peak values of the two results obtained from impact tests and FEM analysis within the error range between 1.7% and 8.4%, numerical solution model can be accepted as adequate and can be used for systems have such stopper designs and mechanisms. Moreover, strain-time graph characteristics are also similar between the results of test and the numerical solution. This similarity between strain-time curves increases the reliability of the numerical results.

However, it is clearly seen that, the main difference between the results of tests and numerical solution is the impact duration time. It can be seen that, impact duration of numerical solution for aluminum, steel and titanium stoppers are 15.5, 15.25 and 14.75 milliseconds, respectively. On the other hand, for test result, for each stopper, impact duration is about 19.06, 18.04 and 18.09 milliseconds. These results and impact duration differences are given in the Table *5.1.4* below.

Table 5.1.4 Impact duration of Test Result for Different Materials

Stopper Material	**AL6061-T651**	**AISI 304**	**TI-6AL-4V**
Impact Duration for Tests (msec)	19.30	18.60	18.91
Impact Duration for FEM (msec)	15.50	15.25	14.75
Difference (msec)	3.80	3.35	4.16
Error %	19.69	18.01	22

As seen above, impact duration differences are higher than expected and error values are significant. Thus, this outcome should be investigated carefully. After performing some other literature survey, LU et al. introduced a theory about contact duration and indentation depth of collision with a new approach [26]. According to their theory, contact duration and contact indentation is related to coefficient of restitution (COR) and coefficient of indentation (COI). These parameters are influenced by elastic, elastic-plastic or plastic behavior of contact between a flat plate and circular plate colliding to each other. As plasticity increases in collision occurrence, the impact duration increases. In addition, they have concluded that, as the impact velocity increases, impact duration decreases for a limit of certain approach velocity as seen in Figure *5.1.7*. In the study, this velocity limit is set to the value of velocity at which the colliding bodies or materials yield. After yield point, impact duration starts to increase as velocity increases, as seen in Figure *5.1.8*.

With this study, it can be said that similar results are obtained for impact duration-approach velocity relationship. Tests are conducted for impact with rotational velocities of 5, 10, 15, 20, 25 and 30 RPM. Readings from strain gauges' second channels, which is nearest channel to (Y) axis with respect to stopper geometry, on aluminum, steel and titanium specimens are given in below Figure *5.1.9* and tables from Table *5.1.5* to Table *5.1.7*. Small differences may be result of the complexity of the system teste, frictional losses between contacting faces, damping characteristics of the whole system and friction losses at reducer, motor, bearing and slip ring at the elevation axis. This time duration difference cannot be seen in FEM model due to the difficulty of modelling these parameters of the whole system in ANSYS Mechanical.

Table 5.1.5 Impact Duration - Impact Velocity Relation for Aluminum Stopper

Velocity	Contact Time	Separation Time	Impact Duration
5	76.49	96.56	20.08
10	76.88	96.27	19.39
15	78.44	98.26	19.81
20	78.60	97.98	19.38
25	78.67	97.98	19.32
30	78.67	97.97	19.30

Table 5.1.6 Impact Duration - Impact Velocity Relation for Steel Stopper

Velocity	Contact Time	Separation Time	Impact Duration
5	78.52	97.59	19.07
10	76.58	96.98	20.41
15	78.20	97.04	18.84
20	78.36	97.04	18.68
25	78.58	97.22	18.64
30	78.27	96.88	18.60

Table 5.1.7 Impact Duration - Impact Velocity Relation for Titanium Stopper

Velocity	Contact Time	Separation Time	Impact Duration
5	69.91	90.09	20.17
10	76.72	96.25	19.53
15	76.80	96.26	19.46
20	76.63	96.02	19.39
25	76.72	96.18	19.46
30	76.80	95.71	18.91

In our study, impact durations obtained from FEM analysis are shorter than ones obtained from impact test results. This can be explained due to the plastic and elastic deformations seen on colliding bodies. Due to the convergence concerns of the FEM results, plastic deformations and tangent modulus' of the materials did not taken into consideration. Many attempts have been conducted, however, any converged solution obtained due to the complexity of the system model. In the results, it has been seen that, plastic deformation on stopper geometries does not dominate the whole solution, plastic deformations are neglected

and the effect of plastic deformations are accounted as error source for the output of this study.

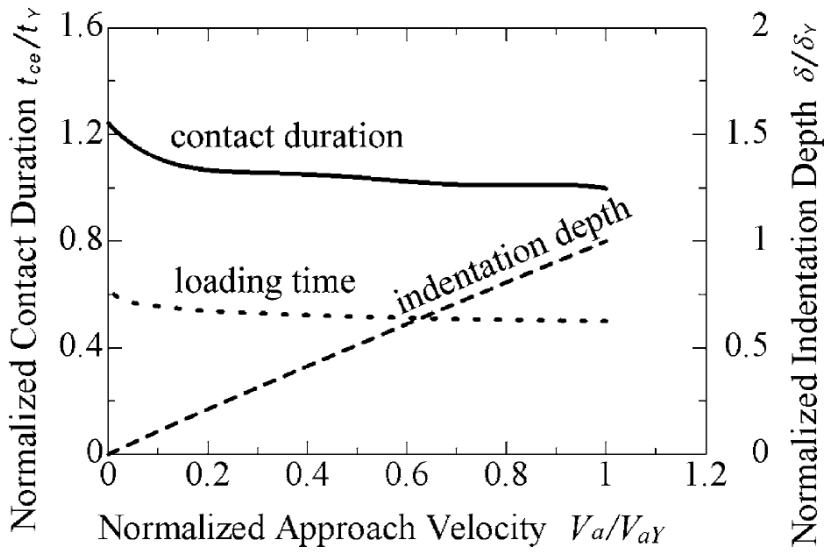

Figure 5.1.7 Impact Duration - Impact Velocity Relation in Elastic Region from LU's Study

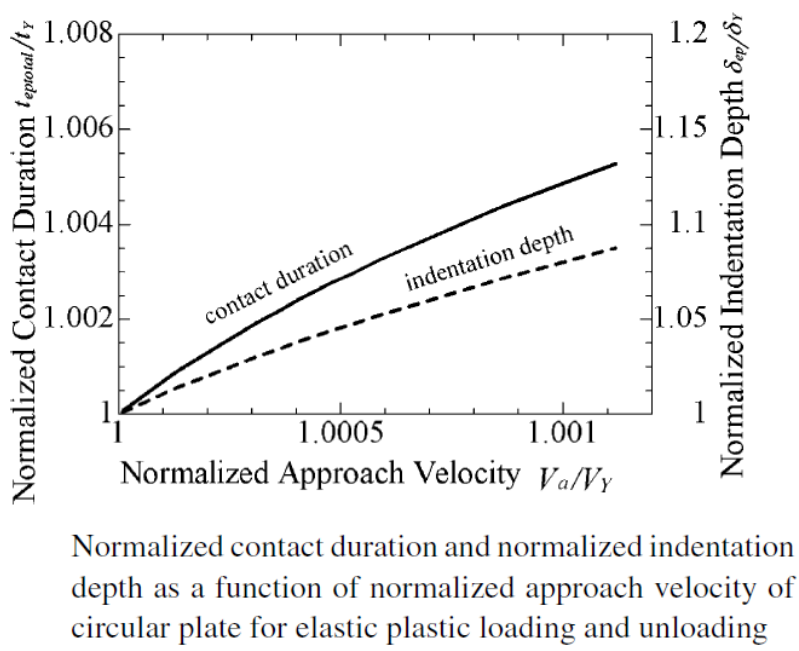

Figure 5.1.8 Impact Duration - Impact Velocity Relation in Plastic Region from LU's Study

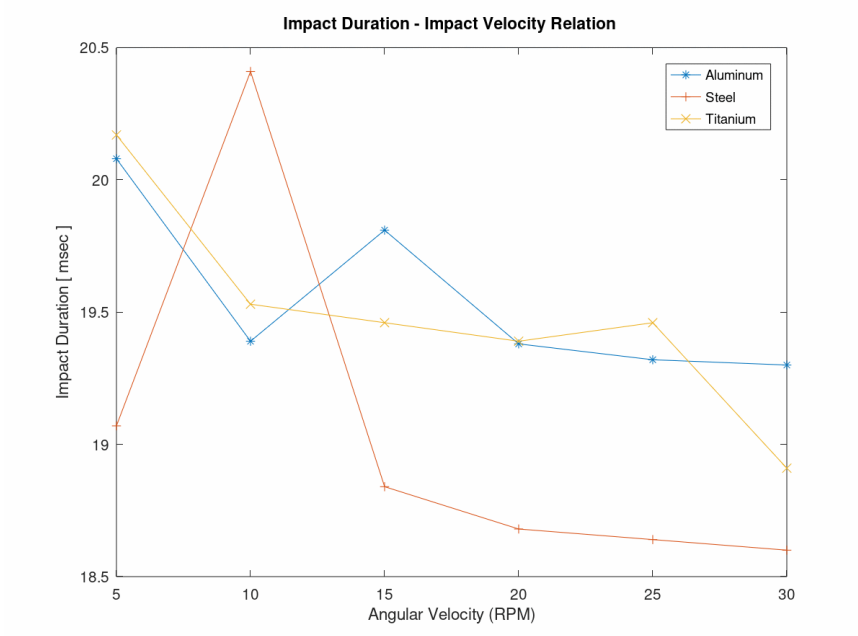

Figure 5.1.9 Impact Duration - Impact Velocity Relation from Impact Tests for Different Materials

5.2 Implementation to Mathematical Models

Since results of impact test and numerical solution are comparable and consistent within an acceptable error margin, numerical solution outputs can be used to demonstrate the mathematical models mentioned in above sections. As we discussed above, the mathematical models have been arisen from the study conducted by Hertz, and within the years, many approaches have been suggested by scientists. Thus, for our case, it can be beneficial to check which of the mathematical model fit for the solution of such stopper mechanisms as we discussed. Before calculating the mathematical models, impact parameters like indentation, restitution velocity and COR should be taken from FEM results. Velocity profiles for three different materials are given in below figures, and the parameters adapted from FEM results can be seen in tables from Table 5.2.1 to Table 5.2.3. These values are used to calculate the results for mathematical models described and listed in Table 2.2.1. Performing the analytical solutions gives contact forces, which are listed in tables

Table 5.2.4, Table 5.2.5 and Table 5.2.6. Restitution velocities and velocity profiles of the FEM result can be seen in Figure 5.2.1.

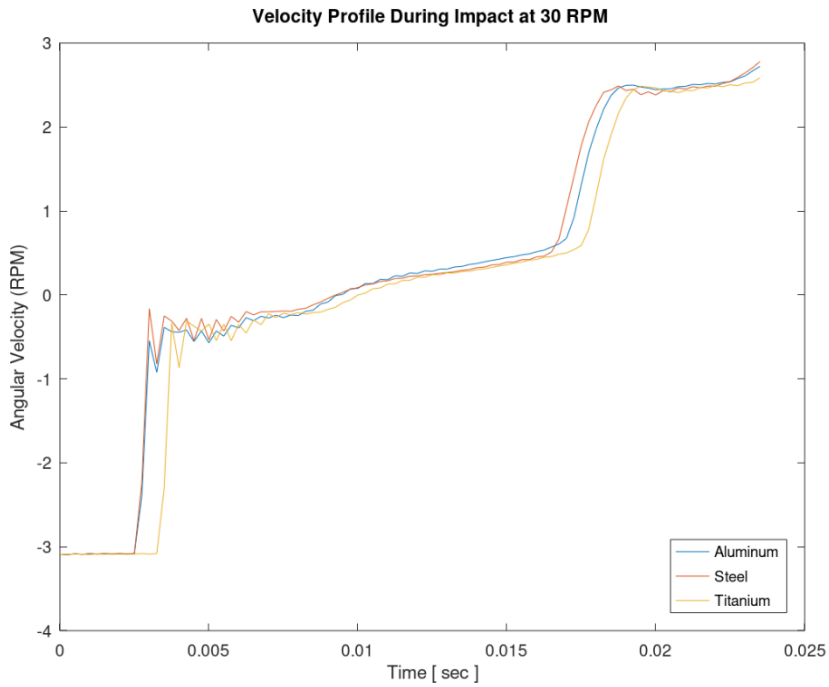

Figure 5.2.1 Velocity Profiles of FEM Results

Table 5.2.1 Impact Parameters for Aluminum Stopper

Parameters	**Value**	**Unit**	**Info**
vs	0.33	-	Poisson Ratio of Stopper
vk	0.33	-	Poisson Ratio of Body
Es	68900	N/mm^2	Elastic Modulus of Stopper
Ek	68900	N/mm^2	Elastic Modulus of Body
hs	1.293E-05	mm^2/N	Modifying Parameter of Stopper
hk	1.293E-05	mm^2/N	Modifying Parameter of Body
a	9.3	mm	Impact Area
K	7.57E+05	N/mm	Contact Stiffness
ms	200	kg	Mass of Stopper
mk	100	kg	Mass of Body
meff	66.66666667	-	Effective Mass
d	0.096738	mm	Indentation
ddot	266.65	mm/s	Indentation Velocity
Vi	334.74	mm/s	Approach Velocity
Vr	266.65	mm/s	Restitution Velocity
cr	0.796588397	-	Coefficient of Restitution

Table 5.2.2 Impact Parameters for Steel Stopper

Parameters	Value	Unit	Info
vs	0.28	-	Poisson Ratio of Stopper
vk	0.33	-	Poisson Ratio of Body
Es	200000	N/mm^2	Elastic Modulus of Stopper
Ek	68900	N/mm^2	Elastic Modulus of Body
hs	4.608E-06	mm^2/N	Modifying Parameter of Stopper
hk	1.293E-05	mm^2/N	Modifying Parameter of Body
a	9.3	mm	Impact Area
K	1.12E+06	N/mm	Contact Stiffness
ms	200	kg	Mass of Stopper
mk	100	kg	Mass of Body
meff	66.66666667	-	Effective Mass
d	0.0742	mm	Indentation
ddot	242.53	mm/s	Indentation Velocity
Vi	334.74	mm/s	Approach Velocity
Vr	242.53	mm/s	Restitution Velocity
cr	0.724532473	-	Coefficient of Restitution

Table 5.2.3 Impact Parameters for Titanium Stopper

Parameters	Value	Unit	Info
vs	0.342	-	Poisson Ratio of Stopper
vk	0.33	-	Poisson Ratio of Body
Es	113800	N/mm^2	Elastic Modulus of Stopper
Ek	68948	N/mm^2	Elastic Modulus of Body
hs	7.760E-06	mm^2/N	Modifying Parameter of Stopper
hk	1.292E-05	mm^2/N	Modifying Parameter of Body
a	9.3	mm	Impact Area
K	9.47E+05	N/mm	Contact Stiffness
ms	200	kg	Mass of Stopper
mk	100	kg	Mass of Body
meff	66.66666667	-	Effective Mass
d	0.089475	mm	Indentation
ddot	258.91	mm/s	Indentation Velocity
Vi	334.74	mm/s	Approach Velocity
Vr	258.91	mm/s	Restitution Velocity
cr	0.773465974	-	Coefficient of Restitution

Table 5.2.4 Calculated Hysteresis Damping Factors and Contact Forces for Aluminum Stopper

Mathematical Model	**X (Hysteresis Damping Factor, N/mm)**	**Fn (Contact Force, N)**
Hunt-Crossley	689.94	28309.84
Herbert-McWhannell	498.31	26772.41
Lee-Wang	344.97	25542.14
Anagnostopoulos	325.99	81632.22
Lankarani-Nikravesh	619.77	27746.86
Zhiyinh-Qishao	930.92	30243.20
Gonthier	1037.37	31097.29
Flores	923.86	30186.58
Gharib-Hurmuzlu	2838.64	45548.89
Hu-Guo	866.12	29723.32
Hertz	-	22774.44

Table 5.2.5 Calculated Hysteresis Damping Factors and Contact Forces for Steel Stopper

Mathematical Model	**X (Hysteresis Damping Factor, N/mm)**	**Fn (Contact Force, N)**
Hunt-Crossley	1377.79	29313.69
Herbert-McWhannell	1080.66	27857.18
Lee-Wang	688.90	25936.74
Anagnostopoulos	557.96	92860.50
Lankarani-Nikravesh	1188.02	28383.45
Zhiyinh-Qishao	2061.07	32663.10
Gonthier	2186.28	33276.87
Flores	2028.40	32502.97
Gharib-Hurmuzlu	4602.18	45119.57
Hu-Guo	1901.63	31881.52
Hertz	-	22559.79

Table 5.2.6 Calculated Hysteresis Damping Factors and Contact Forces for Titanium Stopper

Mathematical Model	X (Hysteresis Damping Factor, N/mm)	Fn (Contact Force, N)
Hunt-Crossley	960.90	31993.01
Herbert-McWhannell	712.70	30273.13
Lee-Wang	480.45	28663.75
Anagnostopoulos	411.18	94220.96
Lankarani-Nikravesh	852.06	31238.82
Zhiyinh-Qishao	1340.40	34622.78
Gonthier	1468.81	35512.62
Flores	1325.15	34517.08
Gharib-Hurmuzlu	3656.04	50668.97
Hu-Guo	1242.33	33943.17
Hertz	-	25334.48

Contact force readings from FEM analysis are given in table below, in Table *5.2.7*, and the error margin of the mathematical models can be seen in tables, Table *5.2.8*, Table *5.2.9* and Table *5.2.10* for aluminum, steel and titanium stoppers respectively.

Table 5.2.7 FEM Contact Reaction Forces

Stopper Material	Contact Reaction Force, N
AL6061-T651	29346
AISI 304	29919
TI-6AL-4V	29547

Table 5.2.8 Error Percentage of Reaction Force for Aluminum Stopper

Hunt-Crossley	-3.53 %
Herbert-McWhannell	-8.77 %
Lee-Wang	-12.96 %
Anagnostopoulos	178.17 %
Lankarani-Nikravesh	-5.45 %
Zhiyinh-Qishao	3.06 %
Gonthier	5.97 %
Flores	2.86 %
Gharib-Hurmuzlu	55.21 %
Hu-Guo	1.29 %
Hertz	-22.39 %

Table 5.2.9 Error Percentage of Reaction Force for Steel Stopper

Hunt-Crossley	-2.02 %
Herbert-McWhannell	-6.89 %
Lee-Wang	-13.31 %
Anagnostopoulos	210.37 %
Lankarani-Nikravesh	-5.13 %
Zhiyinh-Qishao	9.17 %
Gonthier	11.22 %
Flores	8.64 %
Gharib-Hurmuzlu	50.81 %
Hu-Guo	6.56 %
Hertz	-24.60 %

Table 5.2.10 Error Percentage of Reaction Force for Titanium Stopper

Hunt-Crossley	8.28 %
Herbert-McWhannell	2.46 %
Lee-Wang	-2.99 %
Anagnostopoulos	218.89 %
Lankarani-Nikravesh	5.73 %
Zhiyinh-Qishao	17.18 %
Gonthier	20.19 %
Flores	16.82 %
Gharib-Hurmuzlu	71.49 %
Hu-Guo	14.88 %
Hertz	-14.26 %

5.3 Characterization of Stoppers and Recommendations

In this section of the study, the results of the FEM analysis is compared with results of mathematical models mentioned above. Before going deep into the mathematical models, one should consider that, the results of FEM analysis has error sources due to friction and lack of detail of electric motor, reducer and slip ring used in elevation axis. However, after checking FEM strain results and test strain gauge results, the strain time graphs show similar characteristics and results are said to be close to each other. In addition, in case of including plastic deformations and effects to the stopper and load carrier geometries, impact duration difference may get smaller and/or vanish. Thus, FEM analysis can be said to be a good approximation to analyze such complex systems.

Analytical models seem to fit well to the FEM results as seen in the section above. Especially, the accordance of the error margin between FEM results and analytical method results are adequate. For aluminum specimen, Herbert – McWhannel model gives -8.77% error and this value is -6.89% for steel. The error values are parallel for different materials, especially for aluminum and steel stoppers.

An important issue must be pointed is that, Lankarani – Nikravesh model is not suitable for impact case analyzed in that study. This model is valid only for impact velocities lower than velocity of wave propagated in materials due to impact. This condition is given as,

$$\dot{\delta}_0 \leq 10^{-5}\sqrt{\frac{E}{\rho}}$$

Checking this condition gives us that, wave velocities propagated in materials due to impact are about 50.92, 88.19 and 65.26 mm/s for aluminum, steel and titanium specimens respectively. Since relative contact velocity is about 259 mm/s, this model is not applicable for our system, thus, Lankarani – Nikravesh model should be discarded from mathematical models.

After analyzing results and error margins, it can have said for aluminum and steel specimens that, Gonthier and Flores models can be applicable. Since these models include hysteresis effects and these models can be used for large contact areas, these models can be used to demonstrate the contact normal force and can be used for design of such mechanical stoppers. However, interestingly, these models cannot fit to the results obtained from titanium alloy.

Impact of materials gives us that, COR value is close to 0.75 – 0.8, which gives that, Hunt and Crossley model may fit to the solution. For aluminum and steel specimens, this model gives approximately 2-3% error. This value is 9% for titanium, thus, this model is suitable to correct the solution of impact for the stopper design.

As mentioned in the previous sections, Hertz study is the initial contact force modelling model studied in the literature. However, as mentioned, this model does not count for damping parameter of the materials and does not include hysteresis effects. As seen from the results, for each material, Hertz model has given lower contact force of colliding stoppers which excess amount of error.

As mentioned above, the stopper mechanism design can be checked and corrected by different approaches of contact force mathematical models found in the literature. The main concern should be analyzing the system correctly, and filling the model requirements and setting boundary conditions carefully.

In addition, as a material for impact stopper, designer should check material properties carefully. As seen above results, FEM analysis can be used to see the effects of impact on stopper materials. In addition, to choose stopper material, titanium stopper yielded with the lower stress value for the same analysis. This is the result of the fact that, titanium alloy has higher value of toughness and resilience. These parameters can be related to the ability of materials energy absorbance. The stress levels can be seen in Figure *5.3.1*, Figure *5.3.2* and Figure *5.3.3* for aluminum, steel and titanium specimens, respectively.

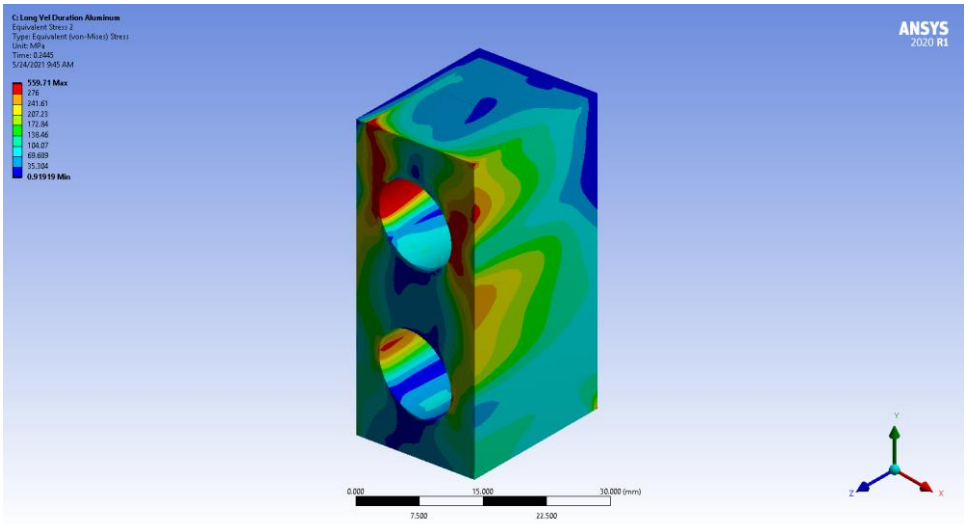

Figure 5.3.1 Stress Level for Aluminum Stopper

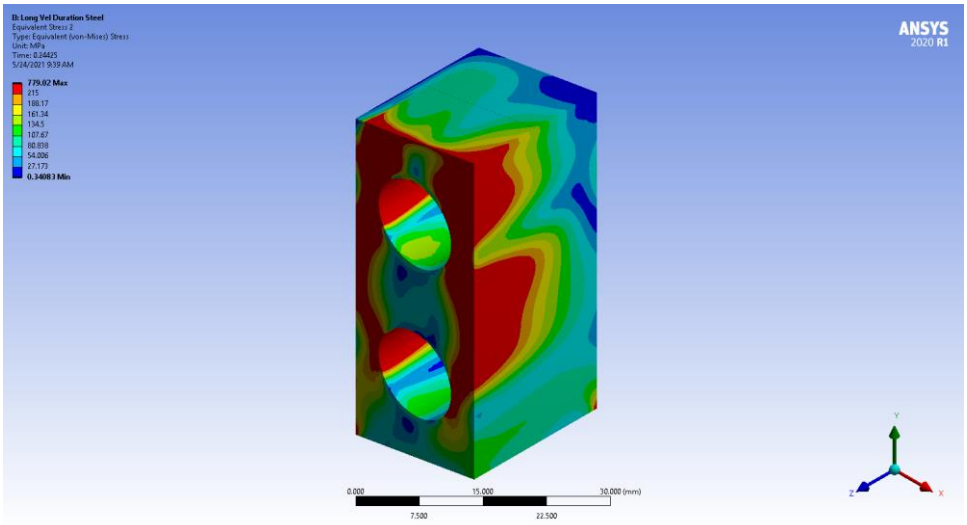

Figure 5.3.2 Stress Level for Steel Stopper

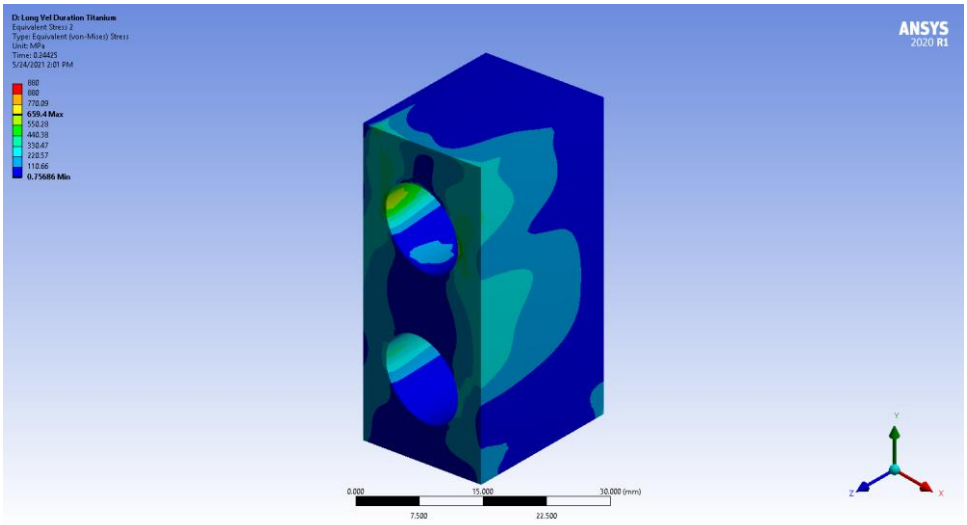

Figure 5.3.3 Stress Level for Titanium Stopper

As seen above figures, highest stress can be seen on steel material with a value of 779 MPa. This can be explained with high stiffness of the material and low energy absorbance characteristics. For such designs, aluminum alloy can be selected as stopper material due to its low material price and high specific properties with high energy absorbance characteristics due to its high resilience property. Titanium can also be selected; however, high base material price and machinability difficulty can be disadvantages.

6 CONCLUSION AND FUTURE WORK

In this study, it is aimed to analyze the dynamics of impact phenomena of mechanical stopper. In engineering area for such systems, it is essential to design mechanical stoppers to stop and/or limit the motion of payload in a safe manner. Stopping the motion of payload with a mechanical stopper provides a controlled environment for impact occurrence. In this case, it is important to understand the behavior of stoppers under impact load. Thus, a known stopper geometry is analyzed with different materials as mentioned above, stainless steel AISI 304, aluminum AL6061-T651 with chromate coating and titanium TI-6AL-4V samples. Firstly, motion stopper mechanism is performed and the reaction of the stoppers under impact loading are recorded via strain gauges for each stopper material. Tests are conducted for each material with different approach velocities. After conducting impact test in physical environment, the stopper mechanism is modelled in computer aided FEM software. The mechanism and system detail is introduced and after proper system simplifications, adequate system geometry is modelled and simulated in virtual environment. The results of real time impact tests are compared with FEM analysis results of same geometry with same materials. The results of impact test and FEM simulation are investigated and compared with each other with respect to stopper materials. As seen in above sections, FEM results with modelled geometry are close to impact test results. Thus, such parameters like those that restitution velocity, indentation etc. are implemented to mathematical models and these results are calculated with contact force model approaches found in the literature. At the end, FEM analysis, test results and analytical solutions gave us adequate and comparable results with in the accountable range of error. Thus, it can be said that, FEM model procedure and FEM model settings can be used to demonstrate and investigate the impact phenomenon. Moreover, effect of impact loading on different materials analyzed. For mechanical stoppers under impact loading with higher velocity, stopper material should be chosen with higher resilience value, which corresponds to energy absorption ability of material. Higher elastic modulus reduces the stress level on stopper geometry via reducing strain values however; stainless steel has lower yield point than titanium thus yields rapidly. Titanium has superior impact endurance nevertheless, due to base material price and lack in machinability properties, titanium would be the second choice. For such systems with high velocity and

high payload mass and inertia, one should select titanium stopper in their design. With its superior specific properties, ease of machinability and low cost compared to other specimens, aluminum stopper should be the best choice for mechanical stoppers. For better strength properties, one should use AL-7075 alloy with convenient surface coating against corrosion instead of AL-6061 alloy.

For the future, implementing plastic properties of materials to the FEM model will be primary objective. As mentioned in the study, plastic deformations have an important effect on the behavior of stopper under impact loading and source of energy dissipation in the system. Thus, reducing the FEM model to increase convergence ability with plastic properties of materials will be beneficial for the study.

System analyzed in the study is a significantly complex structure. This situation creates many other phenomenon during impact test. The geometry has many sub structures and connections between them. Bearing structures, slip rings, gear chains, reducers increases the non-linearity of the system tested. Thus, system will be simplified before analyzing. For example, a direct drive system will be tested and analyzed with the same procedure.

Finally, stoppers will be modelled with thin elastomer parts between colliding surfaces. The effect of elastomer parts and effect of shore parameter of elastomers will be compared to each other. In addition, composite materials and effect of fiber directions on stopper parts under impact loading will be studied in the future to investigate the effect of fiber structure of composite materials. Different stopper geometries with different contact angles may be studied and optimization about stopper geometry with stopper material will be a fair challenge for the future of this study.

7 REFERENCES

[1] H. Hertz, "Ueber die Beruehrung fester elastischer Koerper," *Journal fuer die reine und angewandte Mathematik,* vol. 91, pp. 156-171, 1881.

[2] W. Goldsmith, Impact: The Theory and Physical Behaviour of Colliding Solids, Edward Arnold, 1960.

[3] X. Zhu, "Tutorial on Hertz Contact Stress," 2012.

[4] Y. A. Khulief and A. A. Shabana, "A continuous force model for the impact analysis flexible multibody systems," *Mechanism and Machine Theory,* vol. 22, no. 3, pp. 213-224, 1987.

[5] Margarida Machado, Pedro Moreira, Paulo Flores, and Hamid M. Lankarani, "Compliant contact force models in multibody dynamics: Evolution of the Hertz contact theory," *Mechanism and Machine Theory,* vol. 53, no. 0, pp. 99-121, 2012.

[6] Paulo Flores and Jorge Ambrósio, "On the contact detection for contact-impact analysis in multibody systems," *Multibody System Dynamics,* vol. 24, no. 1, pp. 103-122, 2010.

[7] K. H. Hunt and F. R. E. Crossley, "Coeffient of restitution interpreted as damping in vibroimpact," *Journal of Applied Mechanics,* vol. 7, pp. 440-445, 1975.

[8] T. M. Guess, G. Thiagarajan, M. Kia, and M. Mishra., "A subject specific multibody model of the knee with menisci," *Medical Engineering and Physics,* vol. 32, no. 5, pp. 505-515, 2010.

[9] R. G. Herbert and D. C. McWhannell, "Shape and frequency composition of pulses from an impact pair," *Journal of Engineering for Industry,* vol. 99, pp. 513-518, 1977.

[10] T. W. Lee and A. C. Wang, "On the dynamics of intermittent-motion mechanisms, Part 1: dynamic model and response," *Journal of Mechanisms, Transmissions, and Automation in Design,* vol. 105, pp. 534-540, 1983.

[11] H. M. Lankarani and P. E. Nikravesh, "A Contact Force Model With Hysteresis Damping for Impact Analysis of Multibody Systems," *Journal of Mechanical Design,* vol. 112, no. 3, pp. 369-376, 1990.

[12] S. Shivaswamy, Artist, *Modeling contact forces and energy dissipation during impact in multibody mechanical systems.* [Art]. Wichita State University, Witchita, Kansas, 1997.

[13] A. L. Schwab, J. P. Meijaard, and P. Meijers, "A comparison of revolute joint clearance models in the dynamic analysis of rigid and elastic mechanical systems," *Mechanism and Machine Theory,* vol. 37, pp. 895-913, 2002.

[14] P. Flores, J. Ambrosio, J. C .P. Claro, and H. M. Lankarani, "Dynamic behaviour of planar rigid multi-body systems including revolute joints with clearance," *Proceedings of the Institution of Mechanical Engineers Part K: Journal of Multi-body Dynamics,* vol. 221, no. 2, pp. 161-174, 2007.

[15] O. Muvengei, J. Kihiu, and B. Ikua, "Dynamic analysis of planar multi-body systems with LuGre friction at differently located revolute clearance joints," *Multibody System Dynamics,* vol. 28, no. 4, pp. 369-393, 2012.

[16] Z. F. Bai and Y. Zhao, "A hybrid contact force model of revolute joint with clearance for planar mechanical systems," *International Journal of Non-Linear Mechanics,* vol. 48, pp. 15-36, 2013.

[17] Y. Gonthier, J. McPhee, C. Lange, and J. C. Piedboeuf, "A regularized contact model with asymmetric damping and dwell-time dependent friction," *Multibody System Dynamics,* vol. 11, no. 3, pp. 209-233, 2004.

[18] Q. Zhiying and L. Qishao, "Analysis of impact process based on restitution coeffcient," *Journal of Dynamics and Control,* vol. 4, pp. 294-298, 2006.

[19] P. Flores, M. Machado, M. T. Silva, and J. M. Martins, "On the continuous contact force models for soft materials in multibody dynamics," *Multibody System Dynamics,* vol. 25, no. 3, pp. 357-375, 2011.

[20] S. Hu and X. Guo, "A dissipative contact force model for impact analysis in multibody dynamics," *Multibody System Dynamics,* vol. 35, no. 2, pp. 131-151, 2015.

[21] Luka Skrinjar, Janko Slavic, Miha Boltezar, "A review of continuous contact-force models in multibody dynamics," *International Journal of Mechanical Sciences,* vol. 145, pp. 171-187, 2018.

[22] Avinash S. Joshi and Laxmikant M. Gupta, "A simulation study on quantifying damage in bridge piers subjected to vehicle collisions," *International Journal of Advanced Structural Engineering*, vol. 4:8, 2012.

[23] C. Cho, Artist, *A Study of Dynamic Impact Models for Pile-Driver Breech Fatigue System.* [Art]. Armanent Research, Development and Engineering Center, 2008.

[24] H. Yazdani Sarvestani, A.H. Akbarzadeh, H. Niknam and K. Hermenean, "3D printed Architected Polymeric Sandwich Panels: Energy Absorption and Structural Performance," *Composite Structures*, 2018.

[25] H.W. Leheta, A.M. Elhewy, W. El Sayed Mohamed, "Finite element simulation of barge impact into a rigid wall," *Alexandria Engineering Journal*, vol. 53, pp. 11-21, 2014.

[26] Zhongjie LU, Koichi TANAKA, Masahiro NISHIDA and Fenglei HUANG, "Theoretical Investigation on the Contact Duration in Elastic and Inelastic Collision of a Circular Plate to Planar Surface," *JSME International Journal*, vol. 49, no. 2, pp. 258-264, 2006.

8 APPENDIX

A. Strain Gauge Datasheet

G1350

MICRO MEASUREMENTS
A VPG Brand

General Purpose Strain Gages—Stacked Rosette

GAGE PATTERN DATA

actual size

GAGE DESIGNATION See Note 1	RESISTANCE (OHMS)	OPTIONS AVAILABLE
L2A-XX-G1350-120/SP70*	120 ± 0.6%	
C2A-XX-G1350-120/SP70*	120 ± 0.6%	SP20
C2K-XX-G1350-350/SP70*	350 ± 0.8%	SP20

DESCRIPTION

Stacked, 0°-45°-90° rosette for use in applications involving limited gaging areas or steep strain gradients. The matrix has a circular trim (SP70).

Pb Pb-free
RoHS COMPLIANT

GAGE DIMENSIONS

Legend
ES = Each Section
S = Section (S1 = Section 1)
CP = Complete Pattern
M = Matrix

inch
millimeter

Gage Length	Overall Length	Grid Width	Overall Width	Matrix Length	Matrix Width
0.040 ES	0.144 CP	0.045 ES	0.147 CP	0.20	0.20
1.0 ES	3.66 CP	1.14 ES	3.73 CP	5.1	5.1

GAGE SERIES DATA — See Gage Series datasheet for complete specifications

Series	Description	Strain Range	Temperature Range
L2A	Encapsulated constantan gages with preattached ribbon leads.	±3%	−100° to +250°F (−75° to +120°C)
C2A	Encapsulated constantan gages with preattached ready-to-use cables.	±3%	−60° to +150°F (−50° to +66°C)
C2K	Encapsulated Karma gages with preattached ready-to-use cables.	±1.5%	−60° to +150°F (−50° to +66°C)

Example of an
L2A Construction

Example of an
C2A Construction

Note 1: Insert desired S-T-C number in spaces marked XX.

*SP70: circular trim of matrix.

Disclaimer

ALL PRODUCTS, PRODUCT SPECIFICATIONS AND DATA ARE SUBJECT TO CHANGE WITHOUT NOTICE.

Vishay Precision Group, Inc., its affiliates, agents, and employees, and all persons acting on its or their behalf (collectively, "VPG"), disclaim any and all liability for any errors, inaccuracies or incompleteness contained herein or in any other disclosure relating to any product.

The product specifications do not expand or otherwise modify VPG's terms and conditions of purchase, including but not limited to, the warranty expressed therein.

VPG makes no warranty, representation or guarantee other than as set forth in the terms and conditions of purchase. **To the maximum extent permitted by applicable law, VPG disclaims (i) any and all liability arising out of the application or use of any product, (ii) any and all liability, including without limitation special, consequential or incidental damages, and (iii) any and all implied warranties, including warranties of fitness for particular purpose, non-infringement and merchantability.**

Information provided in datasheets and/or specifications may vary from actual results in different applications and performance may vary over time. Statements regarding the suitability of products for certain types of applications are based on VPG's knowledge of typical requirements that are often placed on VPG products. It is the customer's responsibility to validate that a particular product with the properties described in the product specification is suitable for use in a particular application. You should ensure you have the current version of the relevant information by contacting VPG prior to performing installation or use of the product, such as on our website at vpgsensors.com.

No license, express, implied, or otherwise, to any intellectual property rights is granted by this document, or by any conduct of VPG.

The products shown herein are not designed for use in life-saving or life-sustaining applications unless otherwise expressly indicated. Customers using or selling VPG products not expressly indicated for use in such applications do so entirely at their own risk and agree to fully indemnify VPG for any damages arising or resulting from such use or sale. Please contact authorized VPG personnel to obtain written terms and conditions regarding products designed for such applications.

Product names and markings noted herein may be trademarks of their respective owners.

Copyright Vishay Precision Group, Inc., 2014. All rights reserved.

B. M-Bond 200 Strain Gauge Adhesive Datasheet

M-Bond 200

MICRO MEASUREMENTS
A VPG Brand

Strain Gage Adhesive

OTHER ACCESSORIES USED IN AN M-BOND 200 INSTALLATION:

- CSM Degreaser or GC-6 Isopropyl Alcohol
- Silicon Carbide Paper
- M-Prep Conditioner A
- M-Prep Neutralizer 5A
- GSP-1 Gauze Sponges
- CSP-1 Cotton Applicators
- PCT-2M Gage Installation Tape

Pb-free
RoHS
COMPLIANT

DESCRIPTION

For routine experimental stress analysis applications under temperate environmental conditions, M-Bond 200 adhesive is ordinarily the best choice. This adhesive is very easy to handle, and cures almost instantly to produce an essentially creep-free, fatigue-resistant bond, with elongation capability of five percent or more.

M-Bond 200 is a cyanoacrylate that has been pretested and certified for use in bonding strain gages. It is an excellent general-purpose adhesive for laboratory and short-term field applications. The procedure for making a strain gage installation with M-Bond 200 is illustrated and described in detail in Instruction Bulletin B-127 included in each kit of adhesive.

The user should note that the performance of the adhesive can be degraded by the effects of time, humidity conditions, elevated temperature, and moisture absorption. Because of the latter effect, strain gage installations should always be covered with a suitable protective coating. When necessitated by more rigorous test requirements and/or environmental conditions, consideration should be given to one of the M-Bond epoxy adhesives, using the "Recommended Adhesives/ Strain Gage Series" chart.

CHARACTERISTICS

PARAMETER	DETAILS	
CURE REQUIREMENTS*	One-minute thumb pressure, followed by a minimum two-minute delay before tape removal. Bond strength increases rapidly during first five minutes. Cure time must be extended under conditions of low temperature [<70°F (<21°C)] or low humidity (<40% RH).	
OPERATING TEMPERATURE RANGE	**Short Term:** –300° to +200°F (–185° to +95°C).	**Long Term:** –25° to +150°F (–32° to +65°C).
ELONGATION CAPABILITIES	>5% at +75°F (+24°C), 3% at +75°F (+24°C) when used with CEA or EA/Option E strain gages.	
SHELF LIFE	Minimum 12 months when stored unopened at +40°F (+5°C) or minimum 9 months when stored unopened at +75°F (+24°C). *Note:* To ensure a proper seal, wipe bottle spout clean and dry before replacing cap. *Note:* Condensation rapidly degrades adhesive performance and shelf life; if refrigerated, allow adhesive to reach room-temperature before opening. Refrigeration after opening is not recommended.	
POT LIFE	Maximum 3 months at +75°F (+24°C) (not to exceed date of expiration) after opening. Replace the cap immediately after each use.	

PACKAGING OPTIONS

KIT	BULK
1 bottle (1 oz/28 g) Adhesive 1 brush-cap bottle (30 ml) Catalyst	1 bottle (1 oz/28 g) Adhesive 5 tubes (2 g each) Adhesive 16 bottles (1 oz/28 g each) Adhesive 12 brush-cap bottles (30 ml each) Catalyst

***Reference:** Instruction Bulletin B-127 for complete details.

Disclaimer

ALL PRODUCTS, PRODUCT SPECIFICATIONS AND DATA ARE SUBJECT TO CHANGE WITHOUT NOTICE.

Vishay Precision Group, Inc., its affiliates, agents, and employees, and all persons acting on its or their behalf (collectively, "VPG"), disclaim any and all liability for any errors, inaccuracies or incompleteness contained herein or in any other disclosure relating to any product.

The product specifications do not expand or otherwise modify VPG's terms and conditions of purchase, including but not limited to, the warranty expressed therein.

VPG makes no warranty, representation or guarantee other than as set forth in the terms and conditions of purchase. **To the maximum extent permitted by applicable law, VPG disclaims (i) any and all liability arising out of the application or use of any product, (ii) any and all liability, including without limitation special, consequential or incidental damages, and (iii) any and all implied warranties, including warranties of fitness for particular purpose, non-infringement and merchantability.**

Information provided in datasheets and/or specifications may vary from actual results in different applications and performance may vary over time. Statements regarding the suitability of products for certain types of applications are based on VPG's knowledge of typical requirements that are often placed on VPG products. It is the customer's responsibility to validate that a particular product with the properties described in the product specification is suitable for use in a particular application. You should ensure you have the current version of the relevant information by contacting VPG prior to performing installation or use of the product, such as on our website at vpgsensors.com.

No license, express, implied, or otherwise, to any intellectual property rights is granted by this document, or by any conduct of VPG.

The products shown herein are not designed for use in life-saving or life-sustaining applications unless otherwise expressly indicated. Customers using or selling VPG products not expressly indicated for use in such applications do so entirely at their own risk and agree to fully indemnify VPG for any damages arising or resulting from such use or sale. Please contact authorized VPG personnel to obtain written terms and conditions regarding products designed for such applications.

Product names and markings noted herein may be trademarks of their respective owners.

Copyright Vishay Precision Group, Inc., 2014. All rights reserved.

C. Strain Data Read-Write and Transformation MATLAB Code for AL6061-T651 Specimen

```
clc
clear all
close all

SF=12800/1000;              %Sampling Frequency, Hz
E=70000/10^6;               %Elastic Modulus of AL6061-T651
pois=0.33;                  %Poisson's Ratio of AL6061-T651
offsett=-11.3214;           %Angle Offset of Strain Gauge

for RPM=[5 10 15 20 25 30]   %Test Velocity
  for TEST=[1 2 3]           %Test Sequence

    dataname= horzcat("AL_",num2str(RPM),"_RPM_",num2str(TEST),".asc");
    dataset=dlmread(dataname);
    dataname2= horzcat("AL_",num2str(RPM),"_RPM_",num2str(TEST),".csv");

    dlmwrite(dataname2,dataset(100:end,1:3));



    Ex_Actual=[];
    Ey_Actual=[];
    Shearx_Actual=[];

        t1=(45-offsett)/180*pi;
        t2=((90-offsett))/180*pi;
        t3=(135-offsett)/180*pi;
        transformationmatrix=[(cos(t1))^2 (sin(t1))^2 cos(t1)*sin(t1);...
                    (cos(t2))^2 (sin(t2))^2 cos(t2)*sin(t2);...
                    (cos(t3))^2 (sin(t3))^2 cos(t3)*sin(t3)]^-1;
```

```
    for JJ=0:1:length(dataset(100:end,1))-1

     ACTUALSTRAINS=transformationmatrix*[dataset(100+JJ,1);dataset(100+JJ,2)...
         ;dataset(100+JJ,3)];
     Ex_Actual(JJ+1,1) =ACTUALSTRAINS(1,1);
     Ey_Actual(JJ+1,1)=ACTUALSTRAINS(2,1);
     Shearx_Actual(JJ+1,1)=ACTUALSTRAINS(3,1);

     STRESS=E/((1+pois)*(1-2*pois))*[1-pois pois 0; pois 1-pois 0;...
         0 0 (1-2*pois)]*  [ACTUALSTRAINS(1,1);ACTUALSTRAINS(2,1);...
         ACTUALSTRAINS(3,1)];
     Stress_x(JJ+1,1) =STRESS(1,1);
     Stress_y(JJ+1,1) =STRESS(2,1);
     Stress_xy(JJ+1,1) =STRESS(3,1);

     end

    [MaxValCH1,LocationCH1]=max(abs(Ex_Actual));
    [MaxValCH2,LocationCH2]=max(abs(Ey_Actual));
    [MaxValCH3,LocationCH3]=max(abs(Shearx_Actual));

TIME_DATA=(1:1:length(Ex_Actual((LocationCH1-1000):LocationCH1+2000,1)))*1/SF;


figure(RPM)
plot(TIME_DATA,Ex_Actual((LocationCH1-1000):LocationCH1+2000,1));
hold on
legend("Ch1 Test-1","Ch1 Test-2","Ch1 Test-3")
plottitle=horzcat("Aluminum Stoper ",num2str(RPM),...
"RPM","Test Normal Strain e_x");
```

```
title(plottitle)
xlabel('Time [ \mu sec ]')
ylabel('Strain [ \mu\epsilon ]')

figure(RPM+1)
plot(TIME_DATA,Ey_Actual((LocationCH2-1000):LocationCH2+2000,1));
hold on
legend("Ch2 Test-1","Ch2 Test-2","Ch2 Test-3")
plottitle=horzcat("Aluminum Stoper ",num2str(RPM),...
"RPM","Test Normal Strain e_y");
title(plottitle)
xlabel('Time [ \mu sec ]')
ylabel('Strain [ \mu\epsilon ]')

figure(RPM+2)
plot(TIME_DATA,Shearx_Actual((LocationCH3-1000):LocationCH3+2000,1));
hold on
legend("Ch3 Test-1","Ch3 Test-2","Ch3 Test-3")
plottitle=horzcat("Aluminum Stoper ",num2str(RPM),...
"RPM","Test Shear Strain gamma_{xy}");
title(plottitle)
xlabel('Time [ \mu sec ]')
ylabel('Strain [ \mu\epsilon ]')

figure(RPM+100)
plot(TIME_DATA,Stress_x((LocationCH1-1000):LocationCH1+2000,1));
hold on
legend("Ch1 Test-1","Ch1 Test-2","Ch1 Test-3")
plottitle=horzcat("Aluminum Stoper ",num2str(RPM),...
"RPM","Test Normal Stress_X");
title(plottitle)
```

```
xlabel('Time [ \mu sec ]')
ylabel('Stress [ MPa ]')


figure(RPM+101)
plot(TIME_DATA,Stress_y((LocationCH2-1000):LocationCH2+2000,1));
hold on
legend("Ch2 Test-1","Ch2 Test-2","Ch2 Test-3")
plottitle=horzcat("Aluminum Stoper ",num2str(RPM),...
"RPM","Test Normal Stress_Y");
title(plottitle)
xlabel('Time [ \mu sec ]')
ylabel('Stress [ MPa ]')

figure(RPM+102)
plot(TIME_DATA,Stress_xy((LocationCH3-1000):LocationCH3+2000,1));
hold on
legend("Ch3 Test-1","Ch3 Test-2","Ch3 Test-3")
plottitle=horzcat("Aluminum Stoper ",num2str(RPM),...
"RPM","Test Shear Stress_{XY}");
title(plottitle)
xlabel('Time [ \mu sec ]')
ylabel('Stress [ MPa ]')

  end
end
```

D. Control MATLAB Code for Strain Gauge Validation

```
clc
clear all
close all

SamplingFreq=12800/1000; %Hz
for TEST=[1 2]
  for RPM=[5]

    dataname= horzcat("Gauge_",num2str(RPM),"_RPM_",num2str(TEST),".asc");
    dataset=dlmread(dataname);
    dataname2= horzcat("Gauge_",num2str(RPM),"_RPM_",num2str(TEST),".csv");

    dlmwrite(dataname2,dataset(100:end,1:3));

    [MaxValCH1,LocationCH1]=max(abs(dataset(100:end,1)));
    [MaxValCH2,LocationCH2]=max(abs(dataset(100:end,2)));
    [MaxValCH3,LocationCH3]=max(abs(dataset(100:end,3)));

    TIME_DATA=(1:1:length(dataset((LocationCH1-
30000):LocationCH1+30000,1)))*0.001/SamplingFreq;

figure(RPM)
plot(TIME_DATA,dataset((LocationCH1-30000):LocationCH1+30000,1));
hold on
legend("472 gr at 200 mm","472 gr at 100 mm")
plottitle=horzcat("Static Strain Level at Channel 1");
title(plottitle)
xlabel('Time [ \mu sec ]')
ylabel('Strain [ \mu\epsilon ]')
```

```
figure(RPM+1)
plot(TIME_DATA,dataset((LocationCH2-30000):LocationCH2+30000,2));
hold on
legend("472 gr at 200 mm","472 gr at 100 mm")
plottitle=horzcat("Static Strain Level at Channel 2");
title(plottitle)
xlabel('Time [ sec ]')
ylabel('Strain [ \mu\epsilon ]')

figure(RPM+2)
plot(TIME_DATA,dataset((LocationCH3-30000):LocationCH3+30000,3));
hold on
legend("472 gr at 200 mm","472 gr at 100 mm")
plottitle=horzcat("Static Strain Level at Channel 3");
title(plottitle)
xlabel('Time [ sec ]')
ylabel('Strain [ \mu\epsilon ]')


  end
end
```